Université de Montréal

Odd-Even Effects in Electroactive Self-Assembled Monolayers

par Yanqi Feng

Département de chimie, Université de Montréal
Faculté des arts et des sciences

Mémoire présenté à la Faculté des études supérieures et postdoctorales
en vue de l'obtention du grade de maîtrise (M.Sc.)
en chimie

Octobre, 2017

Abstract

Odd-even effect in the redox-induced molecular reorientations that occur in electroactive molecular films were investigated using surface plasmon resonance (SPR) coupled with cyclic voltammetry. Experiments were conducted on self-assembled monolayers (SAMs) of ferrocenylalkanethiolates on gold (FcC_nSAu) with n = 6-16. SPR was used to follow in situ and real time the electrochemical oxidation and reduction of the FcC_nSAu SAMs. An increase in the resonance angle was observed upon the oxidation of the SAM-bound ferrocene to ferrocenium due to an untilting of the Fc^+C_nS molecules which resulted in a film thickening of ~0.2 nm. An odd-even variation of the resonance angle shift was observed, which originated from a difference in the dielectric constants of FcC_nSAu SAMs with an odd (SAM^{odd}) versus even (SAM^{even}) number of methylenes.

Cyclic voltammetry (CV) was used to characterize the oxidation of the ferrocene group in the presence of sodium perchlorate, and to investigate odd-even effects in the electron transfer and ion pairing reactions. The peak splitting observed in CV was attributed to different packing structures of the SAM related to the polycrystalline nature of the thermally evaporated, gold thin films and annealed gold beads used as the substrates. The apparent redox potential of SAM^{even} is higher than that of SAM^{odd}, which implies that it is harder to oxidize the surface-tethered ferrocenes for even chain lengths. This corroborates theoretical predictions that the van der Waals interactions between the even FcC_nS chains, and therefore the SAM^{even} packing energy, are more favorable.

This work supports a general understanding of the structure-property relationships in ferrocene-terminated SAMs to guide their use as charge transport and storage elements in electronic and electrochemical devices.

Keywords: Self-assembled monolayers, ferrocenylalkanethiolates, electrochemistry, surface plasmon resonance, dielectric properties, molecular reorientation.

Résumé

L'effet de longueur de chaîne paire-impaire sur la réorientation des molécules induites par les réactions rédox dans un film moléculaire électroactif est investigué en utilisant la spectroscopie de résonnance des plasmons de surface (SPR) couplée à la voltampérométrie cyclique. Les expériences ont été réalisées sur des monocouches auto-assemblées (SAMs) de ferrocénylalcanethiolates sur l'or (FcC_nSAu) avec n = 6-16. La SPR est utilisée pour suivre in situ et en temps réel les réactions rédox des SAMs de FcC_nSAu. Une augmentation de l'angle de résonance est observée lors de l'oxidation du ferrocène de la SAM en ferrocénium. Ceci est dû au redressement des molécules de Fc^+C_nS qui cause une augmentation de 0.2 nm de l'épaisseur de la SAM. Une variation pair-impair du déplacement de l'angle de résonnance est observée, et est due à la différence entre les constantes diélectriques des SAMs de FcC_nSAu ayant un nombre impair de méthylènes (SAM^{odd}) et les SAMs de FcC_nSAu ayant un nombre pair de méthylènes (SAM^{even}).

La voltampérométrie cyclique (VC) a été utilisée pour caractériser l'oxydation du groupement terminal ferrocène en présence de perchlorates de sodium, ainsi que pour investiguer les effets pair-impair sur les réactions de transfert électronique et de pairage ionique. Le dédoublement de pic observé dans les VCs est attribué aux différentes structures de paquetage dans la SAM dues à la nature polycristalline du substrat d'or: films minces thermo-évaporés et billes recuites. Le potentiel rédox apparent des SAM^{pair} est plus élevé que celui des SAM^{impair}, ce qui implique qu'il est plus difficile d'oxyder les ferrocènes attachés à la surface pour les chaînes paires. Ce résultat corrobore les prédictions théoriques qui stipulent que les interactions de van der Waals entre les chaînes FcC_nS paires sont plus favorables, et donc que l'énergie de paquetage des SAM^{pair} est plus grande.

Ce travail vise une meilleure compréhension de la relation entre la structure et les propriétés des SAMs ayant un groupement terminal ferrocène, afin de guider leur utilisation en tant qu'éléments de transport de charges et de stockage dans les dispositifs électroniques et électrochimiques.

Mots-clés : Monocouches auto-assemblées, ferrocénylalcanethiolates, électrochimie, résonnance des plasmons de surface, propriétés diélectriques, réorientation moléculaire.

Table of Contents

Abstract i
Résumé ii
Table of Contents iv
List of Tables vi
List of Figures vii
List of Frequently Used Symbols xii
List of Frequently Used Abbreviations xiii
Acknowledgements xiv
Chapter 1. INTRODUCTION 1
1.1 Motivation and Objectives 1
1.2 Self-Assembled Monolayers (SAMs) 3
1.3 Electroactive Ferrocenylalkanethiolate SAMs 12
1.4 Odd-Even Effects in SAMs 17
1.5 SAM Characterization 29
1.5.1 Surface Plasmon Resonance (SPR) 29
1.5.2 Cyclic Voltammetry (CV) 36
1.5.3 Electrochemical Impedance Spectroscopy (EIS) 40
Reference 44
Chapter 2. Experimental Section 54
2.1 Materials 54
2.2 Choice of FcC_nSH Chain Lengths and Gold Substrates 54
..... 55
2.3 Preparation of FcC_nSAu SAMs 56
2.4 Electrochemical Surface Plasmon Resonance (EC-SPR) 58
2.5 Electrochemical Impedance Spectroscopy (EIS) 60
Reference 61
Chapter 3. Results 61

3.1 Electrode Surface Characterization 61
3.2 FcC_nSAu SAM Electrochemistry 63
3.2.1 Cyclic Voltammetry 63
3.2.2 Peak Deconvolutions 66
3.3 Redox-Induced Resonance Angle Change 72
3.4 EIS of the FcC_nSAu SAMs 74
3.5 SAM Thickness Change 79
Reference 80
Chapter 4. Discussion 83
4.1 Surface Microstructure 83
4.2 Film Structure Insights via Cyclic Voltammetry 85
4.3 Odd-Even Effects in the Electrochemical Parameters 88
4.4 Chain Length Dependence of the Oxidation-Induced Thickness Change 91
4.5 Dielectric Properties of the FcC_nSAu SAMs 94
Reference 96
Chapter 5. Summary and Conclusions 102
Reference 104
Supporting Information 105

List of Tables

Table 2.1. Fresnel Layer Model Used to Determine the Oxidation-Induced Change in the Effective SAM Thickness 59

List of Figures

Figure 1.1. Schematic illustration of an ω-functionalized alkylthiolate SAM on gold. 1

Figure 1.2. Illustration of the preparation of RSAu SAM modified Au surfaces. 4

Figure 1.3. Scheme of the film formation process. 6

Figure 1.4. Optical photograph demonstrating a gradient in hydrophilicity, as measured by the spreading of water drops on a $CH_3(CH_2)_{11}SAu$ SAM. 6

Figure 1.5. Schematic depiction of some intrinsic and extrinsic defects found in SAMs formed on a polycrystalline metal substrate. 7

Figure 1.6. An STM image of $CH_3(CH_2)_{11}S$ SAM chemisorbed on Au (111) from ref 32..... 8

Figure 1.7. (A) A schematic representation of an alkanethiols SAM (large shaded circles) on an Au (111) surface (small open circles) where the SAM forms $(\sqrt{3}\times\sqrt{3})R30°$ lattice. (B) Alkanethiolates SAM forms a c(4×2) superlattice structure with a rectangular unit cell composed of four distinct molecules on the Au (111) surface. (C) Commensurate c(2×2) overlayer structure of sulfurs bonded to the rectangular hollow sites of the Au (110) surfaces. 10

Figure 1.8. CVs of $Fc(CH_2)_4COO(CH_2)_9SAu$ SAMs recorded in the presence of different electrolyte anions in aqueous solution. Electrolyte concentration is 0.1 M. Potential scan rate is 100 mV/s. T = 25 °C. 14

Figure 1.9. Schematic illustration of the structure of ferrocenylalkanethiol. 15

Figure 1.10. Illustration of the $FcC_{12}S/Fc^+C_{12}SAu$ reorientation induced by the redox reaction. The anion is not shown. 16

Figure 1.11. Melting points of ferrocenylalkanethiols (bulk or 3D material)..... 18

Figure 1.12. Schematic illustration of ω-functionalized alkanethiolates $(S(CH_2)_nCH_2X)$ chemisorbed onto a metallic surface. 19

Figure 1.13. Friction images of $CH_3(CH_2)_nS$ monolayers patterned on smooth gold at a contact load of ~25 nN by microcontact printing (μP), followed by solution deposition (SD): (A) *n*15(μP), *n*16(SD); (B) *n*16(μP), *n*15(SD); (C) *n*14(μP), *n*15(SD); (D) *n*15(μP), *n*14(SD);

(E) *n*13(μP), *n*14(SD) and (F) *n*14(μP), *n*13(SD). The brighter contrast corresponds to higher friction. 20
Figure 1.14. (A) Idealized structure of n-alkanethiolates on gold substrate. (B) Plots of friction force (f) vs. the contact load (FN) for n-alkanethiolates monolayers chemisorbed on gold. The inset plots represents the f and the absorbance of the s(CH3) obtained from infrared reflection spectroscopy in function of n. 21
Figure 1.15. Contact angle measurement: contact angle (θ). 22
Figure 1.16. Surface roughness and contact angles observed on Au surfaces. AFM images of the Au^{TS} substrate: (A) two-dimensional (2D) view. (B) tilted three-dimensional (3D) view of a 3 × 3 μm surface. (C) Surface roughness and polycrystallinity were confirmed by SEM. (D) Static contact angles measured by a drop of water on *n*-alkanethiolate SAMs formed on Au^{TS} substrate. (E-H) Similar images for the Au^{AD} ("as-deposited") surface. 23
Figure 1.17. (A) Schematic illustration of junctions of Ag^{TS}-SC_nFc//Ga_2O_3/EGaIn; (B) Values of the rectification ratio R as a function of the alkyl chain length *n*. 25
Figure 1.18. (A) Schematic illustration of the odd-even difference in the orientation of the terminal ferrocene unit suggested by NEXAFS and MD simulations in FcC_nSAu SAMs of n_{even} and n_{odd} for an ideal all-trans extended conformation of the alkyl chains. (B) Tilt angle (γ) of the linear backbone of the alkyl chain away from the surface normal as a function of the number of methylenes (*n*), is estimated by molecular dynamics. (C) The ferrocene tilt angles (α_{NEXAFS}) as a function of *n* are derived from the angular dependence of the NEXAFS spectra. (D) The ferrocene tilt angles (α_{MD}) calculated by MD simulations. (B), (C) and (D) are from ref 6. 26
Figure 1.19. Characteristics of junctions with SAMs of SC_nFc on Au and Ag as a function of *n*. (A) Tunneling current, |J| of the junctions at +1.0 V, (B) Rectification ratio, R and (C) Calculated SAM packing energy. 27
Figure 1.20. Schematic illustration of the electromagnetic field with surface plasmons traveling along a metal/dielectric interface. 29
Figure 1.21. Schematic illustration of the Kretschmann attenuated total reflectance (ATR) geometry for the excitation of surface plasmons from ref 92. 32
Figure 1.22. Illustration of a reflectivity-incident angle (R-Θ) or SPR curves. 33

Figure 1.23 Illustration of the electrochemical surface plasmon resonance (EC-SPR) setup used for the investigations of the FcC_nSAu SAMs. 35

Figure 1.24. (A) Surface plasmon resonance angle shifts to higher value when Fc is oxidized into Fc^+ due to an oxidation-induced structural rearrangement of the SAM. (B) Current density j and resonance angle change $\Delta\Theta_{min}$ for five consecutive voltammetric cycles of a $FcC_{16}SAu$ SAM in 0.1 M $NaClO_{4(aq)}$ are shown. 35

Figure 1.25. (A) Cyclic potential sweep. (B) Typical reversible cyclic voltammogram for a soluble redox species at a bare electrode surface. 36

Figure 1.26. Characteristics of a cyclic voltammogram of a redox-active component adsorbed to an electrode surface. 38

Figure 1.27. Characteristics of a cyclic voltammogram of a redox-active component adsorbed on an electrode surface. (A) A peak-broadening CV scan of FcC_6SAu SAM in perchlorate solution. (B) A CV of a single component $FcC_{12}SAu$ SAM with peak splitting. CVs in (A) and (B) were scanned at 10 mV s^{-1}. 39

Figure 1.28. (A) Phasor diagram for alternating current and voltage signals at frequency ω. (B) (C) An impedance response displayed on Bode plots for a series circuit with R = 100 Ω and C = 1 μF. 41

Figure 2.1. AFM height images of (A) thermally-evaporated gold on B270 glass used for ESPR, (B) annealed gold bead electrode used for EIS, (C) FcC_8SAu SAM, and (D) $FcC_{14}SAu$ SAM. Image sizes are (A), (B) 1 μm × 1 μm and (C), (D) 0.5 μm × 0.5 μm. 55

Figure 3.1. Cyclic voltammograms (current density j, right-hand axis) and corresponding resonance angle changes ($\Delta\Theta_{min}$, left-hand axis) recorded by ESPR for FcC_nSAu SAMs in 0.1 M $NaClO_{4(aq)}$ (pH = 5.0). Only data from the second of five consecutive oxidation-reduction cycles is shown for clarity. Scan rate of 10 mV s^{-1}. 63

Figure 3.2. Electrochemical data for FcC_nSAu SAMs formed on gold thin film substrates. (A) Anodic and cathodic peak potentials E_{pa} and E_{pc}, (B) apparent formal redox potential $E^{o'}$, (C) anodic-cathodic peak separation ΔE_p, and (D) ferrocene surface coverage Γ_{Fc} as a function of the number of methylenes n in the alkyl chain. Values for peak 2 are not given for n = 6 and 7 in (A)–(C) because their positions are not discernable by eye. Data points and error bars represent the mean and standard deviation of N different FcC_nSAu SAMs: (A)–(C) N = 7–23

and (D) N = 10–15. The dotted lines are guides to the eye. The black open circles in (D) are the Γ_{Fc} values reported in ref 8 for FcC_nSAu SAMs formed on ultraflat, template-stripped gold films. 65

Figure 3.3. Examples of the anodic peak deconvolution. Blue curves are the individual Gaussian and Lorentzian peaks and red curves are the cumulative fits. The green curves are the fitting residuals. The anodic peaks were baseline corrected with Boltzmann function before mathematical deconvolution. Functions used for the peak deconvolutions: FcC_6SAu Gaussian-Gaussian, FcC_9SAu Gaussian-Gaussian, FcC_{12}SAu Gaussian-Lorentzian, and FcC_{15}SAu Gaussian-Lorentzian. 67

Figure 3.4. Anodic peak deconvolution results. (A) Peak potential E_{pa}, (B) percent area peak area, (C) ferrocene surface coverage Γ_{Fc}, and (D) full width at half maximum E_{fwhm} of the individual peaks as a function of n. N = 10 different voltammetric sweeps were deconvoluted for each n. The data points and error bars represent the mean and standard deviation. The dotted lines are guides to the eye. 68

Figure 3.5. Interaction parameter $\nu G\theta$T as a function of the alkyl chain length n. 71

Figure 3.6. Resonance angle change recorded at the most anodic potential $\Delta\Theta$minox versus the number of methylenes n in the alkyl chain of the FcC_nSAu SAMs. Each data point is the mean of N = 10–19 different FcC_nSAu SAMs. Error bars represent the standard deviations (grey) and 95% confidence intervals (black) of the mean $\Delta\Theta$minox values. The dotted line is a guide to the eye. 73

Figure 3.7. Electrochemical impedance spectroscopy (EIS) data for selected chain lengths. (A) Bode plot – impedance magnitude $|Z|$ vs. frequency. (B) Complex plane plot – imaginary part of the impedance Z'' vs. the real part Z' . (C) Bode phase plot – phase angle φ vs. frequency. Impedance spectra were acquired at 0.0 V versus Ag/AgCl in 0.1 M $NaClO_{4(aq)}$ (pH = 5.0). Symbols are the experimental data and solid lines are the result of CNLS fits to the data using the equivalent circuit model shown in inset in (A) which consists of a solution resistance R_s in series with a constant phase element CPE. 76

Figure 3.8. (A) Plot of the reciprocal of the FcC_nSAu SAM capacitance C_{SAM}^{-1} as a function of n. The solid line represents the linear regression analysis to *all* of the data. Error bars represent the standard deviations of the mean values of N = 10–16 independent measurements

per n. Inset shows the difference ΔC_{SAM}^{-1} between C_{SAM}^{-1} obtained experimentally and C_{SAM}^{-1} calculated based on the regression line. (B) Dielectric constant ϵ_{SAM} calculated from the SAM capacitance using equation 31 and the computed SAM thicknesses reported in ref 6. The thickness of the n = 16 SAM was extrapolated from the reported values. Error bars represent the standard deviations (grey) and 95% confidence intervals (black) of the mean values. Dashed lines are guides to the eye. 78

Figure 3.9. Oxidation-induced FcC_nSAu SAM thickness change Δd^{ox} calculated using the mean values of ϵ_{SAM} determined by EIS and $\Delta\Theta minox$ determined by ESPR. Dashed lines indicate the upper and lower limits of the standard deviation of the average of *all* the data. .. 79

List of Frequently Used Symbols

Å	angstrom (10^{-10} m)
A	electrode area, in cm^2
C_i	capacitance
Γ	surface coverage
ΔE_p	anodic-cathodic peak separation
$\Delta\theta_{min}$	resonance angle shift in SPR
E_a	anodic peak potential
$E°'$	apparent redox potential
E_c	cathodic peak potential
ΔE_{FWHM}	full width at half maximum
F	Faraday constant, 96 485.3 C mol^{-1}
i	Faradic current
Q	charge
v	scan rate, in mV s^{-1}

List of Frequently Used Abbreviations

AFM	atomic force microscopy
Fc	ferrocene
Fc^+	ferrocenium ion
FcC_nSAu	ferrocenylalkanethiolate SAM on gold, *n* represents the alkyl chain length or number of methylene units
CV	cyclic voltammetry
DSC	differential scanning calorimetry
EC-SPR	electrochemical surface plasmon resonance
RSH	*n*-alkylthiol
RSSR	alkyldisulfide
SPR	surface plasmon resonance
SAM	self-assembled monolayer
UME	ultramicroelectrode

Acknowledgements

First and foremost, I would like to express my sincere gratitude to my supervisor, Professor Antonella Badia, for her continuous support throughout my degree. She was always there whenever I encountered problems in my research or experienced dilemmas in planning for the future. Her passion and knowledge encouraged me throughout my research. Her patience and advice calmed me and helped me rationally plan for the future. I feel grateful to have been a member of her group.

In addition to my supervisor, I have benefited greatly from the helpful comments, suggestions, and endless encouragement of my lab colleagues during the entire process. I would like to especially thank my coworkers Tania Sultana for her instructions on SPR experiments and Dr. Eric Dionne for his help with various instruments. I would like to thank Dr. Olga Borozenko and Fadwa Ben Amara for their homemade cakes, which provided me with some enjoyable breaks from work. Thank you Dr. Ngoc Duc Trinh for the many discussions that helped make my work exciting. Your knowledge and suggestions greatly assisted my PhD application process.

I would also like to thank Dr. Violeta Toader in Mcgill for her help with the synthesis of ferrocenylalkanethiolates applied in our experiments.

A special thanks is directed to Patricia Moraille (LCM) for her continuous assistance in collecting AFM images and for helpful discussions. I would also like to thank Jacqueline Sanchez (LCM and RQMP) for her humor and positive attitude which benefited me greatly.

Finally, I would like to thank my parents. Without their selfless moral and economic support, I would never have had the chance to pursue my dream in Canada and meet all of the wonderful people mentioned above. I would also like to thank Zhirou Mao. His presence and encouragement greatly supported my current academic accomplishments.

Chapter 1. INTRODUCTION

1.1 Motivation and Objectives

Molecular self-assembly, as one of the most popular approaches for the modification and functionalization of solid surfaces, has attracted intense interest over the past three decades.[1] Self-assembled monolayers (SAMs) are formed by the spontaneous adsorption of organic molecules on the surfaces of noble metals or semiconductors such as silicon. The intrinsic chemical stability of SAMs, particularly ω-functionalized alkanethiolates on metal surfaces, provide possibilities for fabricating well-defined, flexible, and simple organic interfaces with significant control over their physicochemical properties, such as wetting and lubrication,[2] chemical or biochemical reactivity[3] or electrochemistry.[4]

Tailored SAM surfaces are generally produced by attaching an appropriate functional group (X) at the chain end (e.g., X = $-CH_3$, -OH, -COOH, redox couple or a biological receptor) to achieve the desired surface property (Figure 1.1).

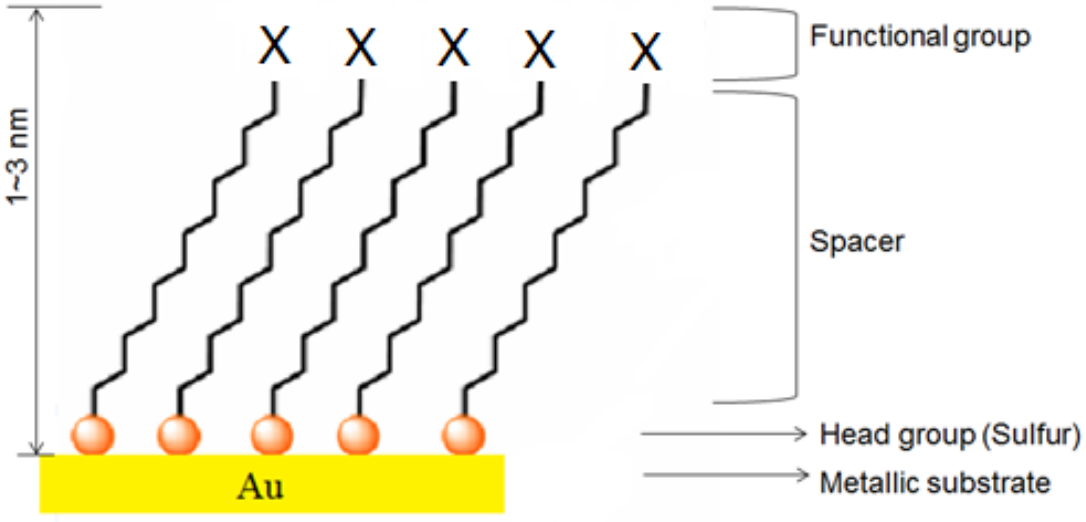

Figure 1.1. Schematic illustration of an ω-functionalized alkylthiolate SAM on gold.

Studies have shown that subtle conformational-based distinctions in the supramolecular structure of SAMs of ω-functionalized alkanethiolates on metal surfaces can have a significant impact on their interfacial and film properties.[1] The work presented in this thesis was specifically motivated by recent investigations of molecular tunneling junctions comprised of SAMs of ω-ferrocenylalkanethiolates on gold (FcC_nSAu) or silver (FcC_nSAg) which show that the relatively small difference of 5° in the tilt angles adopted by the ferrocenes in SAMs of odd versus even-numbered alkyl chains lead to dramatic variances in the electron transport properties and performance of the SAM-based devices.[5] Junctions of FcC_nSAg SAMs with n_{odd} rectify current 10 times more effectively, give a 10% higher yield of working devices, and can be fabricated 2-3 times more reproducibly than n_{even}.[6]

These previous studies focused on electrical measurements on metal (EGaIn)-FcC_nS-metal (Au or Ag) junctions (EGaIn: Eutectic Gallium Indium) in the solid-state (no solvent) and the characterization of the electronic properties of FcC_nSAu or FcC_nSAg SAMs under vacuum.[6] However, FcC_nS-based SAMs have traditionally been investigated and used in electrolyte solution where both electron transfer and ion pairing reactions are operative. Furthermore, most of the information with regards to the odd-even distinctions in the FcC_nS SAM packing structure was derived from molecular dynamics simulation (theory). The degree of conformational order in these SAMs and the effect of the redox reaction on the SAM structure remain to be established.

The objectives of the project are to investigate odd-even effects in the (i) Faradaic electrochemistry of FcC_nSAu SAMs, (ii) redox-induced molecular reorientations that occur in these electroactive SAMs using surface plasmon resonance coupled with cyclic voltammetry and (iii) dielectric properties of the SAMs in the reduced/neutral state.

This introduction chapter is divided into five sections: i) the motivation and objectives of the work, ii) a general introduction to SAMs, including the common preparation protocol and SAM structure, especially ferrocenylalkanethiolate SAMs, iii) the electrochemical characterization of electroactive SAMs and parameters used to define their redox properties, iv) a brief review of the odd-even effects in SAMs, and more specifically odd-even effects in the electric properties of FcC_nS-based junctions, and v) the principle of surface plasmon resonance and its application to the investigation of ultrathin films.

1.2 Self-Assembled Monolayers (SAMs)

The fabrication and characterization of thin film organic surfaces is the focus of intensive research since the interfacial properties may provide insight into fundamental aspects of surface chemistry.[1] The interesting topics include film adhesion, wetting/dewetting phenomena, corrosion, catalysis, bio-chemical reactivity and electron transfer. The spontaneous adsorption of molecular constituents on a solid surface or compression-induced organization of amphiphilic molecules at the air/water interface provides a rational methodology for the preparation of structurally well-defined, organic thin film (Langmuir monolayers). Adsorbates, on self-assembled monolayer (SAM), can be transferred from the solution or gas phase and self-organize into crystalline (or semi-crystalline) structures immediately after adsorption.[1] The self-assembly process is primarily driven by molecule-substrate interactions and intermolecular forces. This concept was first introduced by Zisman and coworkers in 1946 who demonstrated the preparation of SAMs through the adsorption of a surfactant on a platinum substrate.[7] Other SAM systems have since been developed, for example, alcohols on silicon and iron oxides, acid-functionalized alkanes on metal oxides (i.e., α-Al_2O_3, Fe_xO_y, Ti/TiO_2) and organosulfurs on noble metals and metallic compounds (i.e., Ag, Cu, Au, FePt, AgS).[8]

The molecular structure of the SAM can be briefly divided into three distinct parts (Figure 1.1): a functional headgroup that has a specific affinity for the solid substrate; a spacer group, usually an alkyl chain that defines the 2D organization and conformational order, and a terminal group that defines the monolayer function properties. The most common protocol for RSAu SAM preparation (Figure 1.2) involves the immersion of clean metal-coated substrates into a dilute solution of the thiol in a polar solvent such as EtOH (~1-10 mM RSH concentration) for several hours to overnight incubation at room temperature. The substrates are then rinsed copiously with solvent to remove physisorbed material. Finally, the substrates are dried with nitrogen. This method is largely adopted for the preparation of SAMs due to its reproducibility, cost effectiveness, and convenience.

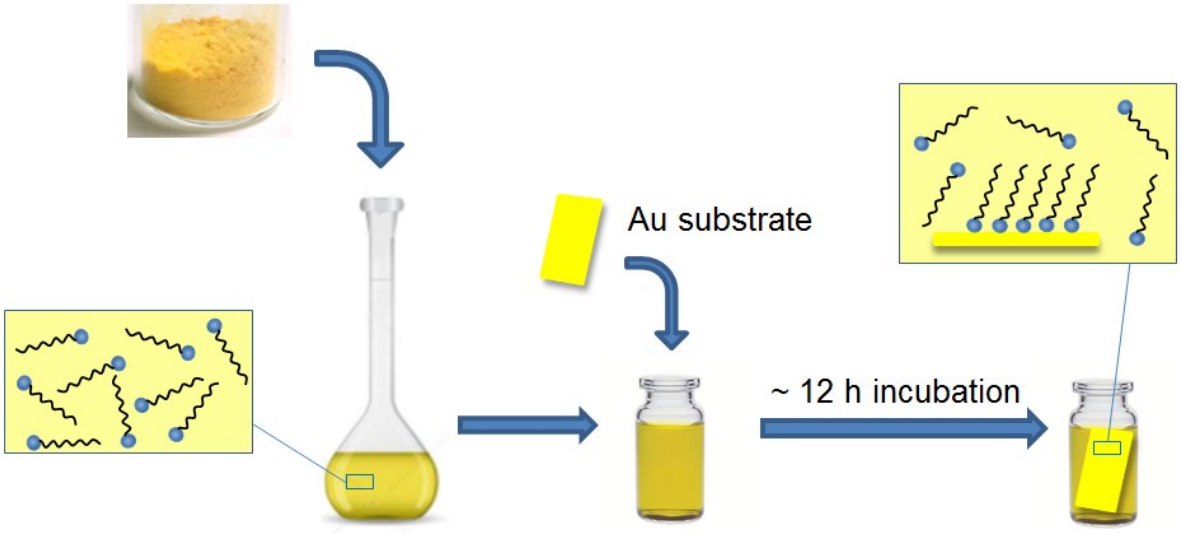

Figure 1.2. Illustration of the preparation of RSAu SAM modified Au surfaces.

The great majority of studies of SAMs are derived from the chemisorption of alkanethiols (RSHs) or alkyldisulfides (RSSRs) on metals such as gold, silver, copper, palladium, platinum and mercury.[1] Among the metals, gold has been regarded as a standard substrate in the study of SAMs for two reasons: (i) it forms good SAMs and (ii) it is reasonably inert in ambient air. The adsorption of *n*-alkanethiols exhibits hydrophobic surfaces with the lowest free energy (19 mJ/m^2) compared to any other hydrocarbon surface studied to date.[9]

Although there is currently no direct supporting evidence, the adsorption of organosulfur compounds is supposed to proceed via oxidative addition between the S-H or S-S and Au which results in a surface gold-thiolate species.[8]

$$\mathrm{R-SH} + \mathrm{Au}_n^o \xrightarrow{-\frac{1}{2}\mathrm{H_2?}} \mathrm{R-S}^{\delta^-}\mathrm{Au}_n^{\delta^+} \cdot \mathrm{Au}_{n-1}^o$$

$$\mathrm{RS-SR} + \mathrm{Au}_n^o \longrightarrow 2(\mathrm{R-S}^{\delta^-}\mathrm{Au}_n^{\delta^+}) \cdot \mathrm{Au}_{n-2}^o \qquad (1)$$

Infrared[10-13] and Raman spectra[14-15] indicate the rupture of the S-H and S-S chemical bonds with the absence of stretching vibrations after monomolecular film formation. The

thiols have a strong affinity for gold and form a largely covalent, but with partial ionic character, Au-S bond of bond energy of ca. 165-210 kJ/mol.[16-17] Additionally, X-ray photoelectron spectroscopy (XPS) measurements confirm the partial ionic character of the Au-S bond.[9, 13, 18-19] The sulfur has a partial negative charge of 0.2 *e*.[20]

The mutual effects from the gold-sulfur chemical electrostatic bond and non-covalent lateral interactions (e.g. van der Waals interactions) among the alkyl chains determine the kinetics and thermodynamics of SAM formation.[21-22] The kinetics of SAM formation is relatively complicated with the involvement of solvent molecules, but the process approximately follows the Langmuir adsorption model in which the rate of deposition is proportional to the available free space.[1, 23] Bain and coworkers initially verified this model by measuring the ellipsometric thickness and contact angles of the SAMs at different incubation times.[9, 24-26] The results indicated that the film formation process can be divided into two steps: (i) a quick and dense coverage of the adsorbates is observed during the first milliseconds to minutes (~ 80-90%);[9] followed by (ii) a slow reorganization process on the order of hours to maximize the structural order and minimize the defects in the system. This explains why overnight incubation is frequently employed to prepare SAMs (Figure 1.3).[1] The final result is a well-ordered, densely-packed surface monolayer with optimal configuration. In practice, there are also a number of experimental conditions that affect the rate of deposition and the resulting SAM structure such as temperature,[27] nature of the solvent,[28] thiol concentration,[9, 29] thiol purity, oxygen content of the solution (usually a problem for easily oxidized metals only),[18, 30] and cleanliness of the substrate surface. Proper experimental conditions reproducibly yield organic interfaces with desired functional behavior.

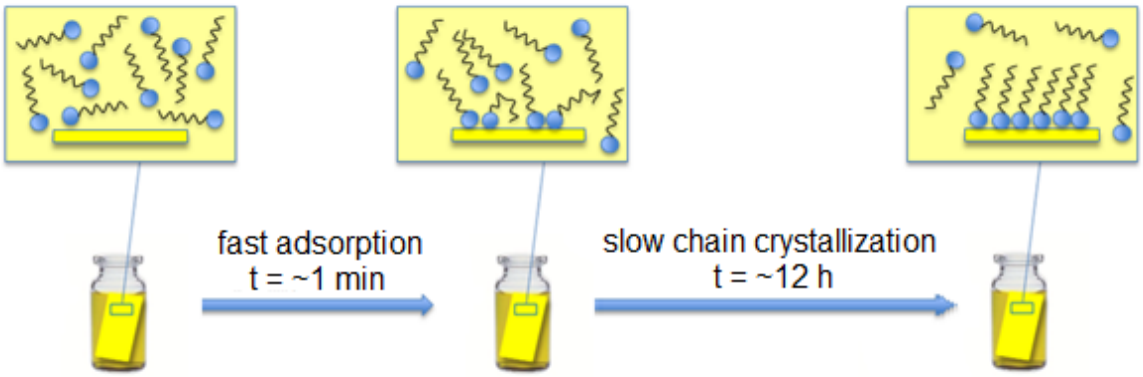

Figure 1.3. Scheme of the film formation process.

Studies by Nicholas *et al*. further support this model. They generated a hydrophobicity gradient film by forming regions/areas of different surface coverage of alkanethiolates along the immersion axis of the gold-coated silicon substrate by increasing the immersion time from bottom to top (Figure 1.4).[31]

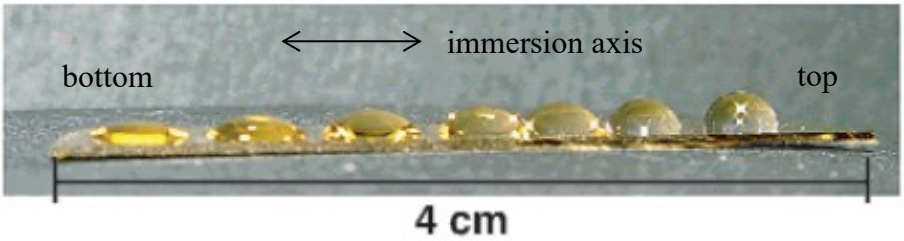

Figure 1.4. Optical photograph demonstrating a gradient in hydrophilicity, as measured by the spreading of water drops on a $CH_3(CH_2)_{11}SAu$ SAM. Reprinted from ref 31. Copyright 2003 American Chemical Society.

The thermodynamic nature of the self-assembly process is such that the SAMs formed are embedded with both intrinsic and extrinsic types of defects as illustrated in Figure 1.5.[1] These originate from external factors such as the substrate preparation method (i.e. surface

roughness and crystallographic microstructure), cleanliness of the substrate, and purity of the immersion solution, while some intrinsic defects result simply from the SAMs dynamic systems with complex phase behaviors (i.e. the defects at the SAM crystal edges in Figure 1.5). In order to obtain reproducible SAMs, several factors should be taken into consideration such as the choice of substrate and incubation time.

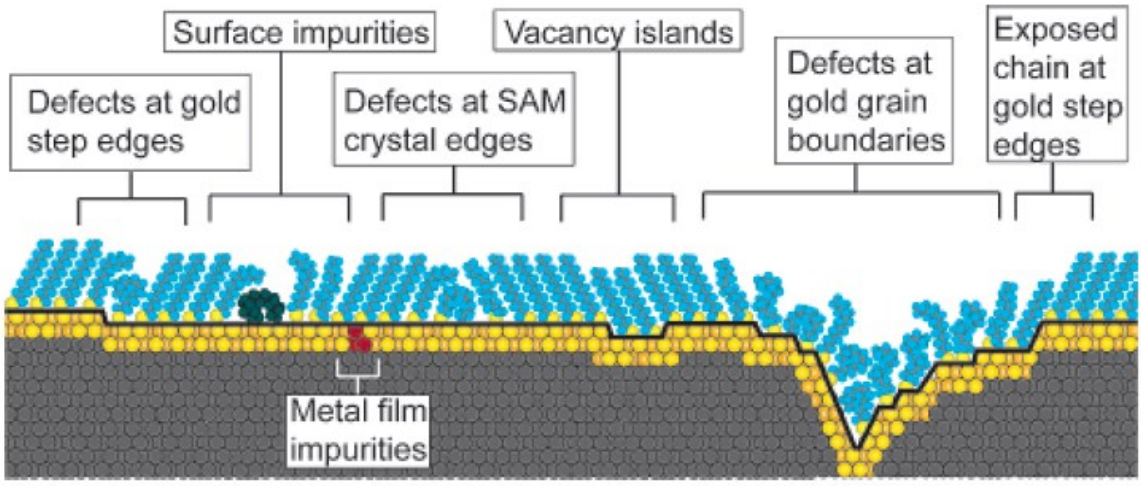

Figure 1.5. Schematic depiction of some intrinsic and extrinsic defects found in SAMs formed on a polycrystalline metal substrate. Reprinted from ref 1. Copyright 2005, American Chemical Society.

Scanning tunneling microscopy (STM) is one of the methods used to visualize SAM defects. Figure 1.6 is an STM image of a dodecanethiolate SAM ($CH_3(CH_2)_{11}S$) on Au (111) prepared by thermal annealing to increase the average domain area.[32] The surface exhibits terraces separated by two Au steps (double arrows), statistically distributed depressions (defects) surrounded by several domains and interconnected by domain boundaries as well as various superstructures within individual domains.

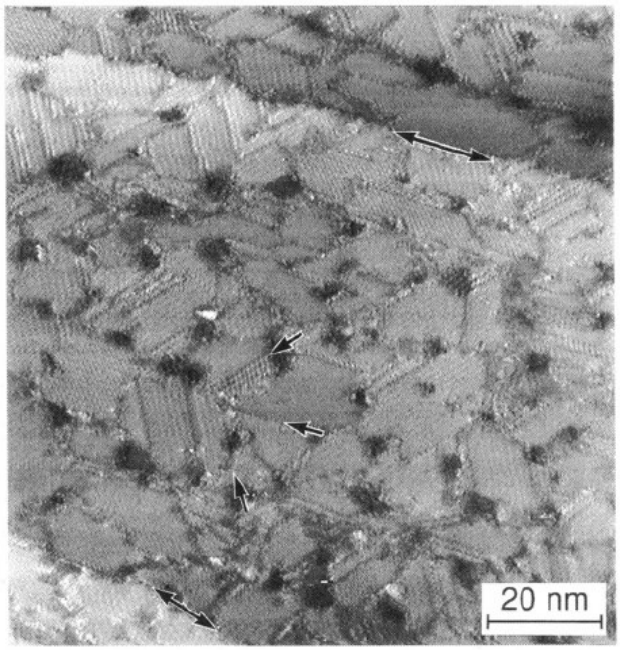

Figure 1.6. An STM image of $CH_3(CH_2)_{11}S$ SAM chemisorbed on Au (111) from ref 32. Copyright 1994 American Chemical Society.

The SAM packing density and intermolecular separation depends on the underlying metal lattice. The S··S spacing and alkyl chain packing density in RS-Au SAMs are largely decided by the structure of the underlying metal lattice. He diffraction,[33-34] electron diffraction[35] and grazing incidence X-ray diffraction[36] studies of alkanethiolates on Au (111) surfaces demonstrate that alkyl chains form commensurate hexagonal arrays with an average S··S spacing of 4.99 Å between alkanethiols chains. The area occupied by each alkyl chain within this structure is 21.7 $Å^2$/molecule. Since the spacing between adjacent sulfurs in alkanethiolates SAMs is greater than the distance with the closest packing arrangement of the alkyl chains (4.24 Å), the chains are typically tilted at an angle ~ 30° from the surface normal to maximize the overall van der Waals interactions. The ellipsometric measurements also confirm that the alkyl chains rotate around the axis chain by an angle (twist angle) of around 52° on surface of Au (111) crystals. The alkyl chains are in the all trans configuration with very few gauche defects. STM studies reveal that sulfurs are bonded to the Au triple hollow sites (Figure 1.7).[24, 26, 37-42] More specifically, STM studies reveal that the sulfur atoms are

bonded to the Au (111) surface crystallographic structure, in which the alkanethiolate forms a ($\sqrt{3} \times \sqrt{3}$)R30° hexagonal lattice.[21, 23, 43-44] and a secondary ordering of the chains corresponding to a c(4×2) superlattice is also observed by grazing-angle X-ray diffraction in ultrahigh vacuum (Figure 1.7B).[45-46] By comparison, the S··S spacing of alkanethiolates adsorbed on a Au (110) surface is 5.76 Å, with the sulfur atoms bonded to the rectangular hollow sites of the Au (110) surface in a commensurate c(2×2) adlayer lattice structure (Figure 1.7C).[47-48] The alkyl chains tilt ~40° from the surface normal which results in a surface packing of the chains ~ 8% less dense than the SAM formed on the Au (111) surfaces.

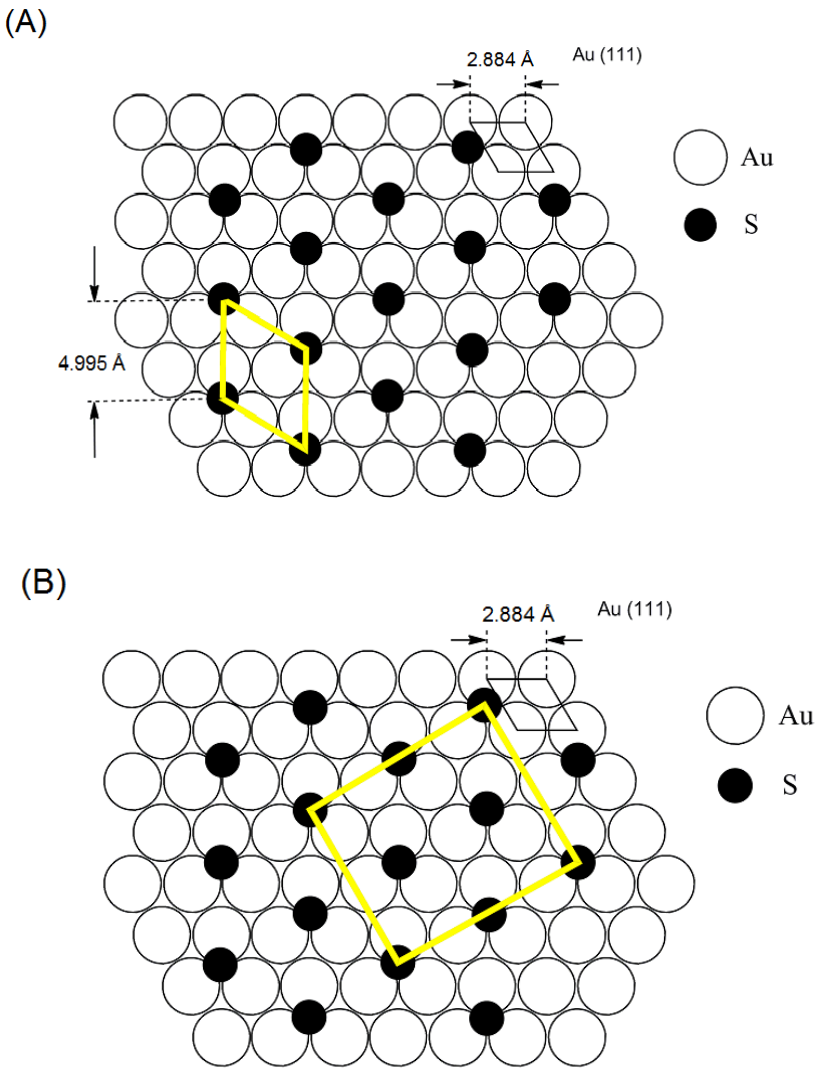

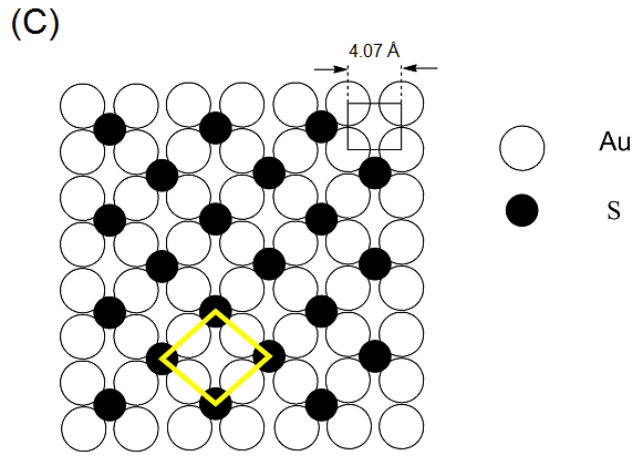

Figure 1.7. (A) A schematic representation of an alkanethiols SAM (large shaded circles) on an Au (111) surface (small open circles) where the SAM forms $(\sqrt{3}\times\sqrt{3})$R30° lattice. (B) Alkanethiolates SAM forms a c(4×2) superlattice structure with a rectangular unit cell composed of four distinct molecules on the Au (111) surface. (C) Commensurate c(2×2) overlayer structure of sulfurs bonded to the rectangular hollow sites of the Au (110) surfaces.

The structure of SAMs of alkanethiolates ($CH_3(CH_2)_nS$) on gold has been extensively characterized. Ellipsometric measurements of the monolayer thickness as a function of the chain length suggests two distinct regions: a non-linear region between n = 1 and n = 9, and a linear region between n = 9 and n = 21.[12] A comparison between the measured thickness and thicknesses calculated assuming a fully extended all-trans conformation for alkyl chains which are tilted 20-30° from the surface normal reveals a close agreement only for the chain lengths n = 10-21.[12] The peak frequencies and peak widths of the methylene stretching modes in infrared spectroscopy are sensitive markers for the extent of the lateral interactions between the polymethylene chains.[49-50] For example, crystalline polymethylene exhibits $\upsilon_a(CH_2)$ and $\upsilon_s(CH_2)$ at 2920 cm^{-1} and 2850 cm^{-1}. The peak positions shift to 2928 cm^{-1} and 2856 cm^{-1} in the liquid phase. A similar trend is observed for bulk *n*-alkanethiols, where $\upsilon_a(CH_2)$ shifts from 2918 cm^{-1} to 2924 cm^{-1} and $\upsilon_s(CH_2)$ shifts from 2851 cm^{-1} to 2855 cm^{-1} from the crystalline to liquid state.[12] A comparison of the $\upsilon_a(CH_2)$ peak frequencies measured for $CH_3(CH_2)_nSAu$ SAMs of n = 3-21 using infrared reflection absorption spectroscopy (IRRAS)

reveals a definite trend toward higher peak frequencies as the alkyl chain length decreases. More specifically, the peak positions (~2918 cm^{-1}) of chain lengths n = 15-21 indicate that the monolayer is in a high density, crystalline-like state, whereas the average local environment of the assemblies with $n \leq 7$ is akin to that of the liquid or disordered state. A similar, but less pronounced trend is also observed for the $\upsilon_s(CH_2)$ mode. Low energy helium diffraction experiments show an abrupt decrease in the diffraction peak intensities for $CH_3(CH_2)_9SAu$ and no diffraction is seen for $CH_3(CH_2)_5SAu$ monolayer, as the carbon chain length is shortened.[51] Altogether, these results indicate a sudden decrease in the SAM order at chain lengths of $n <$ 10, which correlates with the finding of the IRRAS investigation.

1.3 Electroactive Ferrocenylalkanethiolate SAMs

Charge transfer from one site to another over nanometer-scale distances is fundamental to important redox processes in biology,[52] and to the development of a wide range of devices, such as transistors and diodes.[53] Electron transfer in biology is often achieved by the immobilization of biologically-active molecules on organic matter. For instance, the electrochemical oxidation of self-assembled monolayers with hydroquinone terminal groups can be used for the selective immobilization of proteins via Diels-Alder reaction.[54] Electroactive SAMs therefore provide an attractive method for bio-immobilization and the preparation of a range of tailored substrates presenting peptides, carbohydrates, and other low-molecular weight ligands, for studies in cell biology and biotechnology.[55]

Electroactive SAMs (i.e. SAMs bearing a redox terminal group) can also be used in organic/molecular electronics. Two-terminal metal-molecule-metal junctions consist of molecules sandwiched between two metal contacts, in which at least one of the contacts is coated with an electroactive SAM.[1] Common configurations employed in electrochemistry to study the kinetics of electron transfer across SAM-modified electrodes include: (i) thick, hydrophobic SAMs to block a redox species from diffusing to the electrode[12] and (ii) mixed SAMs with at least one molecular component comprised of an electroactive terminal group to minimize diffusion effects.[56-58] Chemical modification of an electrode with redox-tagged alkanethiols makes it possible to immobilize electroactive species on the electrode itself while generating a dielectric barrier layer that prevents the free diffusion of electroactive species or ions to the electrode surface.[59]

The present work focuses on electroactive SAMs, where the oxidation state and charge of the electroactive end groups can be changed by applying a voltage or potential to the SAM-moditified electrode. The original motivation for immobilizing redox-active molecules on metal surfaces was to investigate interfacial electron transfer phenomena.[60-61] The strength of the metal-sulfur bond (i.e., 210 kJ/mol for Au-S)[21] and stabilizing chain-chain interactions in SAMs allows them to retain their structural integrity within a window of applied electrode potentials (-0.5 V—0.85 V vs. Ag/AgCl) and makes electrochemical measurements possible, especially in aqueous electrolytes. The SAM is an electrical, precisely switchable system in

which the redox state of the end groups can be controlled by the amplitude of the applied potential. These two distinct advantages motivate the study of electron transfer processes across metal-SAM interfaces. Due to the attractive electrochemical properties of ferrocene (facile electron transfer, low oxidation potential, and two stable redox states), ferrocene-terminated SAMs are among the most investigated electroactive SAM systems.[56-57, 62-63]

The ferrocene/ferrocenium couple exhibits a straightforward reversible single-electron redox reaction. The surface-confined oxidation proceeds via coupled single electron-transfer and ion-pairing reactions:[62, 64-66]

$$\mathrm{Fc} \rightleftharpoons \mathrm{Fc}^{+} + e^{-}$$

$$\mathrm{Fc}^{+} + \mathrm{X}^{-} \rightleftharpoons \mathrm{Fc}^{+}\mathrm{X}^{-} \quad (2)$$

The formation constant K of the $Fc^{+}X^{-}$ pair is expressed as:

$$K = \Gamma_{\mathrm{Fc}^{+}\mathrm{X}^{-}} / \Gamma_{\mathrm{Fc}^{+}} a_{\mathrm{X}^{-}} \quad (3)$$

where Γ_{Fc+} and Γ_{Fc+X-} are the surface concentrations of ferrocenium and anion-paired ferrocenium, and α_{X^-} is the activity of the anion X^-.[64-65]

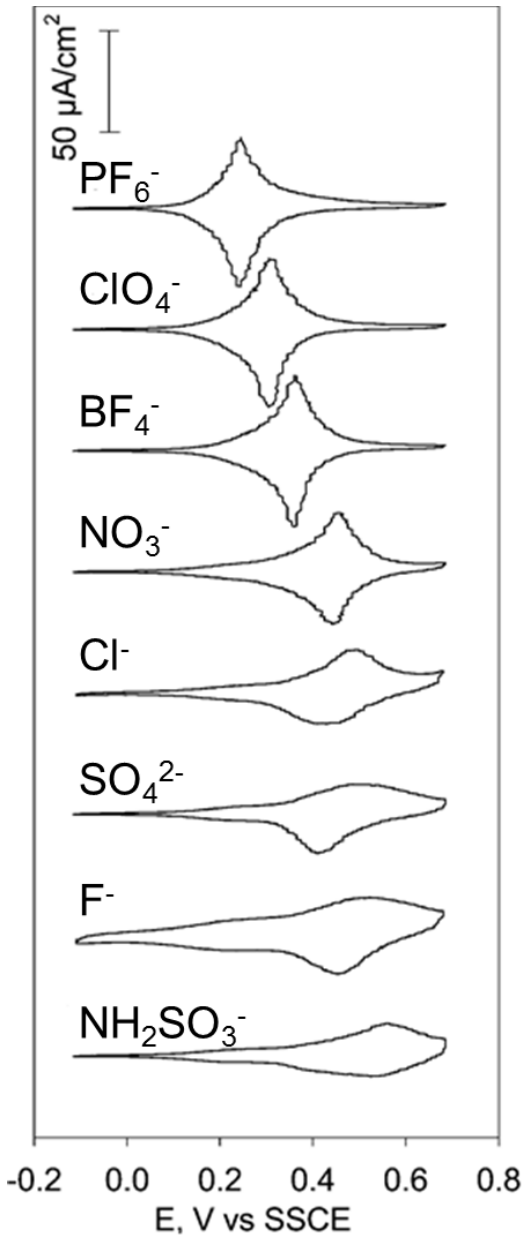

Figure 1.8. CVs of $Fc(CH_2)_4COO(CH_2)_9SAu$ SAMs recorded in the presence of different electrolyte anions in aqueous solution. Electrolyte concentration is 0.1 M. Potential scan rate is 100 mV/s. T = 25 °C. Reprinted from ref 62. Copyright 2004, American Chemical Society.

Ion-pairing between the anion and ferrocenium neutralizes the excess positive charge created at the SAM/electrolyte solution interface.[62, 64-65, 67] It should be noted that the ion-

pairing interactions are not driven simply by an electrostatic force. Certain anions (X^-) exhibit better capacity to pair with the ferrocenium (greater *K*) to stabilize the oxidized form of the SAM. More "hydrophobic" (less hydrated) anions ion pair more effectively than "hydrophilic" ones.[62, 64-65, 68-70] The ion-pairing ability is $PF_6^- > ClO_4^- > BF_4^- > NO_3^- > F^-$.[62] The ability of the anion to pair with the ferrocenium in the typically nonpolar and sterically crowded environment of the SAM determines the electrochemical response of the ferrocene-terminated SAM in terms of the redox potential, number of surface-available ferrocenes oxidized, peak current intensity, and stability to multiple oxidation-reduction cycles (Figure 1.8).[62, 64-65] Fc^+X^- ion pair formation is also known to cause structural changes in the oxidized SAM.[62, 71]

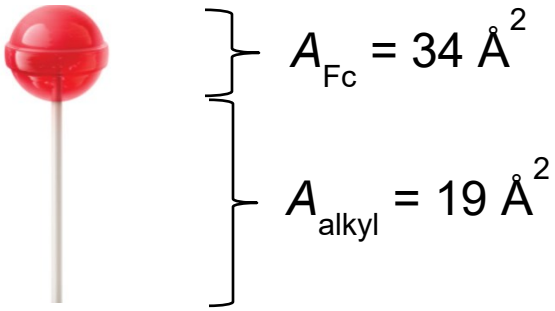

Figure 1.9. Schematic illustration of the structure of ferrocenylalkanethiol.

Ferrocenylalkanethiols have a lollipop shape (Figure 1.9) − there is a mismatch between the size of the ferrocene head and alkyl tail. The maximum surface coverage of the FcC_nS assuming a hexagonal packing of ferrocene spheres of diameter of 6.6 Å is Γ_{max} = 4.5×10^{-10} mol·cm^{-2}.[56] Due to the high density of the ferrocene groups in the SAM, the pairing of anions to the ferrocenium cations is sterically constrained. Spectroelectrochemical measurements show that either the ferrocene heads and/or the alkyl chains adopt a more vertical position so that the ferrocenium can pair with the anions (Figure 1.10).[5, 72] However, there is still a debate as to which one of these reorientations is operative. Oxidation of the SAM-bound ferrocenes has been found to produce a film thickeness change of 0.1-0.5nm,[5, 72] depending on the technique used (ellipsometry, SPR or AFM), and a film volume expansion of the order of 10-20 cm^3·mol^{-1}.[73]

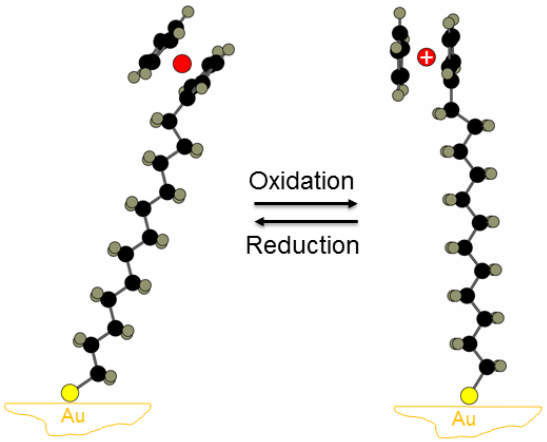

Figure 1.10. Illustration of the $FcC_{12}S/Fc^{+}C_{12}SAu$ reorientation induced by the redox reaction. The anion is not shown.

1.4 Odd-Even Effects in SAMs

Odd-even effects in the structure and properties of materials are a widely observed phenomenon in the field of chemistry, biology, physics and materials science. In general, the odd-even effect describes an alteration of the structure caused by an odd versus even number of structural units in the molecule, such as a methylene group CH_2 in an alkyl chain. These small changes in molecular structure can cause large changes in the overall intermolecular interaction energy and, as a result, a huge difference in the macroscopic structure and properties of the material or films.[74] The odd-even effect manifests itself in bulk materials, including nanomaterials, and at various organic/solid surfaces and interfaces, and it can be applied in crystal engineering,[75] drug design,[76] exchange kinetics,[77] and nanomechanical redox electronics.[78]

Melting points are a classic manifestation of odd-even differences in the molecular structure of a solid. The melting points of the ferrocenylalkanethiols are a good example. Although there is a mismatch in the size of the ferrocene head and the alkyl chain, the melting points of the bulk state ferrocenylalkanethiols, measured by differential scanning calorimetry, exhibit an odd-even alternation as shown in Figure 1.11. The ferrocenylalkanethiols with an even number of CH_2 units exhibit a closer molecular packing compared to the odd number ones, and therefore, the ferrocenylalkanethiols with n^{even} melt at a higher temperature than their n^{odd} homologues.

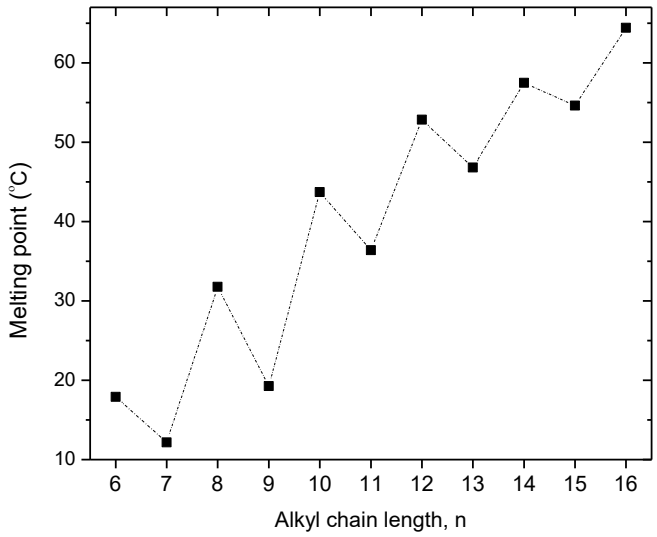

Figure 1.11. Melting points of ferrocenylalkanethiols (bulk or 3D material).

However, when the same molecules are chemically bonded to a solid surface to form 2D organic self-assembled monolayers, the all trans chain conformation results in a different orientation of the terminal group. This odd-even effect originates from the fixed bond angle of the chemical binding group and substrate, such as M-S-C bond angle (i.e., ~100° for Ag-S-C and 110° for Au-S-C)[79] for all SAMs independent of the odd or even number of the methylenes (*n*) in the alkyl chain (Figure 1.12), which leads to an odd-even alternation in the tilt angle (α) of the terminal group with respect of the surface normal and a difference in the molecular packing pattern of the SAMs to meet the energetic equilibrium.

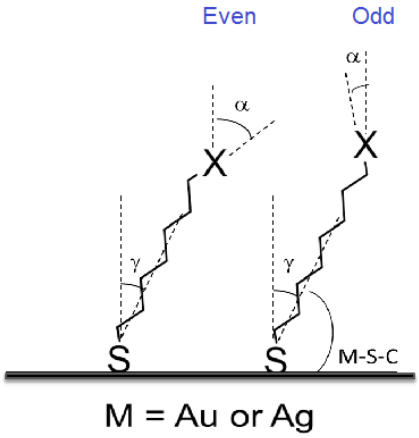

Figure 1.12. Schematic illustration of ω-functionalized alkanethiolates ($S(CH_2)_nCH_2X$) chemisorbed onto a metallic surface.

Recently, several investigations have explored the capabilities of variants of scanning force microscopy (SFM) to map differences in the spatial orientations of terminal chemical groups and to exploit a range of interfacial properties such as adhesion and friction. For instance, Porter and coworkers demonstrated that the difference in the orientation of the terminal group of an organic monolayer has a detectable impact on the friction measured by friction force microscopy (FFM).[80] To test the mapping concept, FFM was used to image $CH_3(CH_2)_nS$ monolayers on gold films and the series of friction images, shown in Figure 1.13, demonstrate two distinct contrasts, with brighter contrast corresponding to areas of higher friction. Figure A, C, D and Figure B, D, F are control experiments, in which the patterning sequence used to prepare the sample were inversed for the latter, to prove that the friction difference was independent from the preparative method. The dipole moment of the methyl groups in the odd-numbered SAM domains is oriented more close to the surface normal compared to that of the methyl groups in the even-numbered domains. The surface free energies of the systems are also correlated with the spatial orientation of the terminal methyl groups.[81] Thus, the friction between the probe tip and the even-numbered domains is greater than that of the odd-numbered domains.

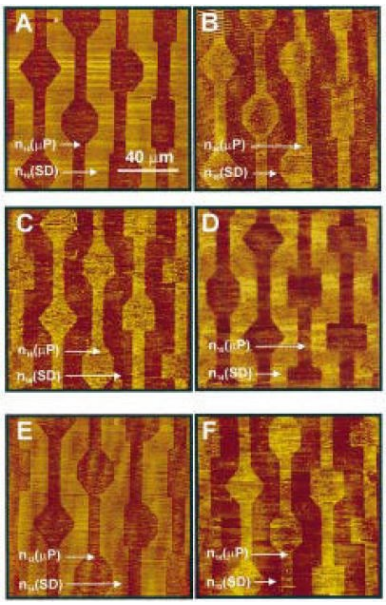

Figure 1.13. Friction images of $CH_3(CH_2)_nS$ monolayers patterned on smooth gold at a contact load of ~25 nN by microcontact printing (μP), followed by solution deposition (SD): (A) *n*15(μP), *n*16(SD); (B) *n*16(μP), *n*15(SD); (C) *n*14(μP), *n*15(SD); (D) *n*15(μP), *n*14(SD); (E) *n*13(μP), *n*14(SD) and (F) *n*14(μP), *n*13(SD). The brighter contrast corresponds to higher friction. Reprinted from ref 80. Copyright 1998, American Chemical Society.

A more quantitative analysis, shown in Figure 1.14, represents the friction (*f*) as a function of the contact load (F_N) on flat regions without contributions from substrate topography. Apart from the linear relation between *f* and F_N, the slopes (the coefficient of friction) follow the trend, 15 < 16 < 13 < 14 < 12, in which the friction measured on adlayers with even-numbered chain length is higher compared to adjacent odd chain length ones. The inset also shows the absorbance of the lower energy $\nu_s(CH_3)$, which implies that the permanent dipole moment of the methyl group is canted more from the surface normal of the gold substrate when *n* is even (~53°) than *n* is odd (~26°).[82] The contact angle of the *n*-alkanethiolates monolayers is only ~2° larger when *n* is odd.[80, 83] The surface free energies are then determined by the spatial orientation of the terminal group and results in a detectable difference in friction.

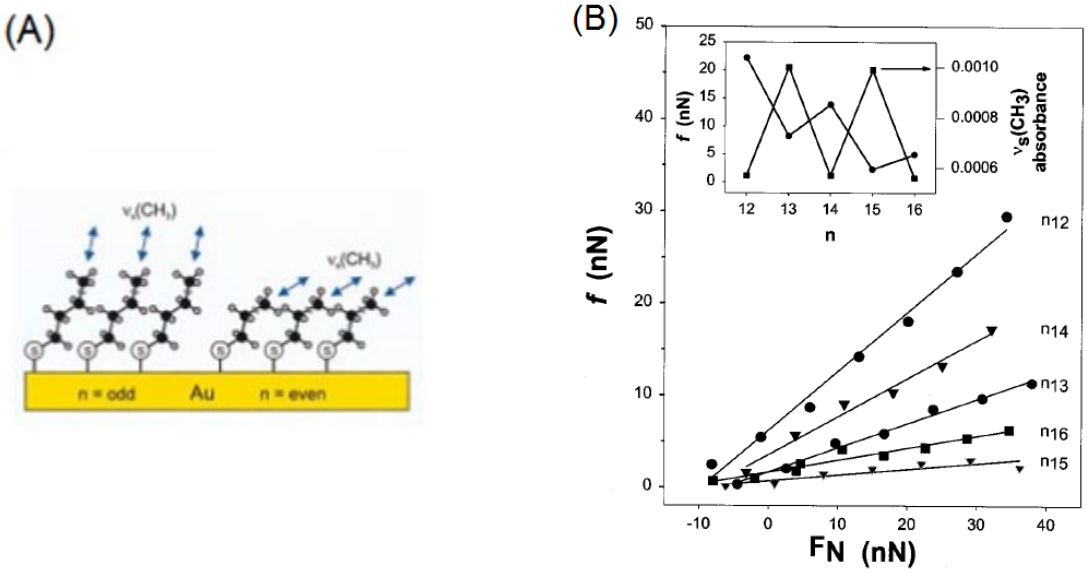

Figure 1.14. (A) Idealized structure of n-alkanethiolates on gold substrate. (B) Plots of friction force (f) vs. the contact load (FN) for n-alkanethiolates monolayers chemisorbed on gold. The inset plots represents the f and the absorbance of the s(CH3) obtained from infrared reflection spectroscopy in function of n. Reprinted from ref 80. Copyright 1998, American Chemical Society.

The wettability was extensively studied for various organic SAMs on Au (111) and Ag (111) via measurements of the contact angle of liquid drops on the SAM (Figure 1.15).[21] The wettability of the SAMs is sensitive to the contact area of the organic monolayers with the contacting liquid,[18, 83-85] and the contact angle of SAMs typically varies from 0° (complete wetting) to 114° (partial or incomplete wetting) determined by the terminal groups.[9] The wetting properties of a number of organic monolayers exhibit an odd-even effect of the chain length, which is generally determined by the topmost structure of the SAM, such as the orientation and dipole of the terminal group, the geometry of the alkyl chain, and the binding of the tethered functional group. For instance, the CF_3-terminated *n*-alkanethiols SAMs exhibit a measurable odd-even effect on rough surfaces whereas the CH_3-terminated SAMs do not. One explanation is that the terminal -CH_2CF_3 has a larger dipole moment and interacts more strongly with relatively weak dipole, such as water, which helps to overcome surface roughness effects and shows the interfacial property of SAMs.

Figure 1.15. Contact angle measurement: contact angle (θ). Reprinted from ref 21. Copyright 1992 Annual Reviews.

More specifically, Thuo and coworkers report that the hydrophobicity of SAMs is dominated by the nature of the substrate (surface roughness and identity) and SAM tilt angle (Figure 1.15), which results in surface dipoles and orientation of the terminal moiety.[86] The static contact angle formed by water droplets on *n*-alkanethiolate SAMs with an odd (SAM^{odd}) or even (SAM^{even}) number of carbons is characterized by a zigzag oscillation in the values of θ_s. An odd-even effect is only observed on SAMs fabricated on ultraflat template-stripped (TS) metal surfaces, in which the interfacial properties are dictated by the SAMs rather than the roughness of the substrates. The contact angle observed with SAM^{odd} on Au^{TS} is lower than that of SAM^{even} which implies water spreads better on SAM^{odd} surfaces than on the analogous SAM^{even} and, therefore, leads to a difference in the interfacial surface energy.

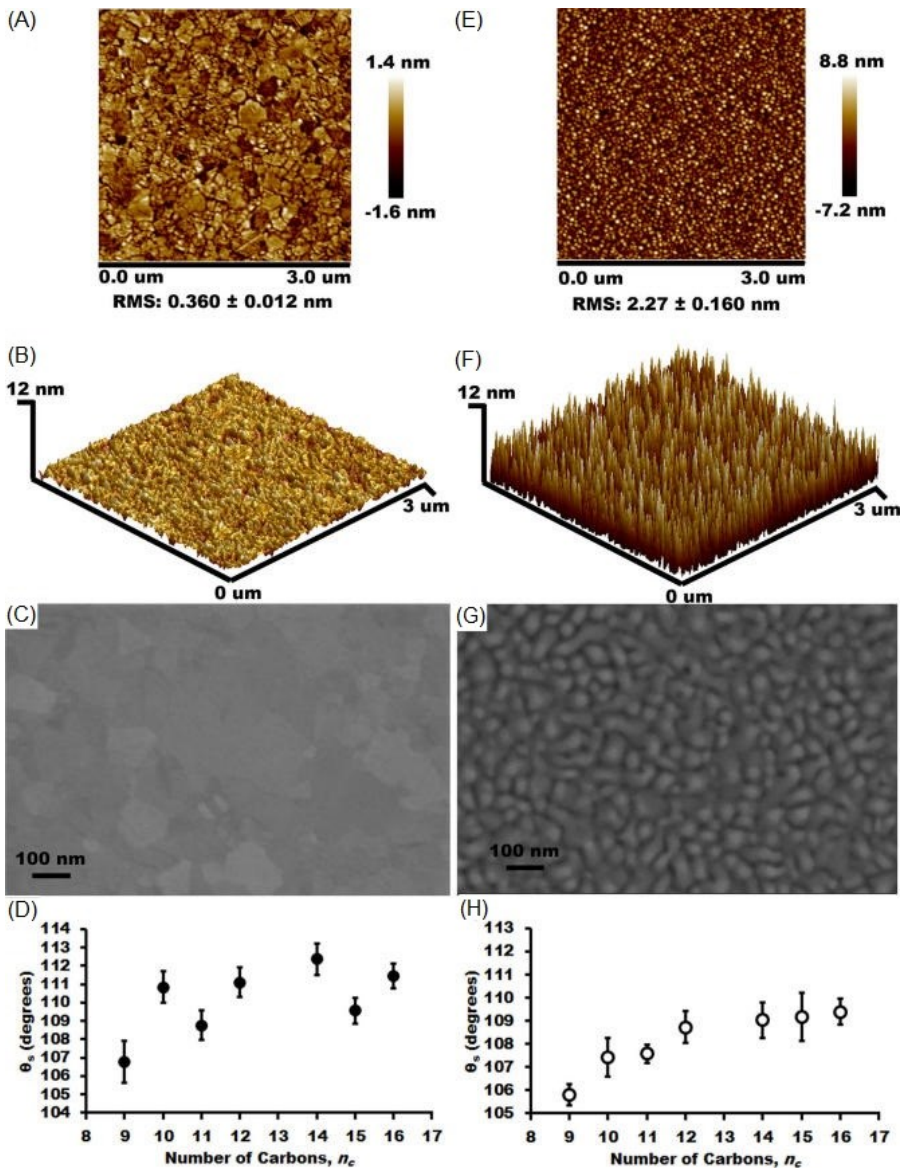

Figure 1.16. Surface roughness and contact angles observed on Au surfaces. AFM images of the Au^{TS} substrate: (A) two-dimensional (2D) view. (B) tilted three-dimensional (3D) view of a 3 × 3 μm surface. (C) Surface roughness and polycrystallinity were confirmed by SEM. (D) Static contact angles measured by a drop of water on *n*-alkanethiolate SAMs formed on Au^{TS} substrate. (E-H) Similar images for the Au^{AD} ("as-deposited") surface. Reprinted from ref 86. Copyright 2014 American Chemical Society.

Christian Nijhuis's group found significant differences in the electrical properties of molecular diodes comprised of FcC_nSAu or FcC_nSAg with n = 6-15.[6] Even though strong π-π interactions (~40 $kJ \cdot mol^{-1}$) have been widely considered to be key for the rational optimization of the performance of organic electronic devices,[87] Nijhuis *et al*. were the first to show that weak intermolecular van der Waals interactions (~15 $kJ \cdot mol^{-1}$) play a crucial role where the film properties change as a function of the number n of the repeat unit.[74] In their experiments, they employed the 'EGaIn' technique,[6, 74] in which SAMs of $Fc(CH_2)_nS$ are covalently bound to template-stripped silver or gold bottom electrodes by Ag-S or Au-S bonds, and the ferrocene termini build van der Waals interactions with the Ga_2O_3/EGaIn top electrodes (Figure 1.17 A). For junctions with FcC_nSAg SAMs of n = 8-13, the values of the rectification ratio for the odd number chain lengths are tenfold larger for the even chain length homologues (Figure 1.17 B). For the shortest chain lengths where n = 6 and 7, the SAMs are disordered with weak alkyl-alkyl chain interactions, and the junctions give low yields of working devices (i.e., molecular diodes). For the longest chain length, where n = 14 and 15, these SAMs are also disordered due to the back-bending of the ferrocene moieties.[6] As a result, an odd-even effect exists only for the middle chain lengths in which van der Waals interactions are more favorable and more ordered SAMs are hypothesized to be formed.

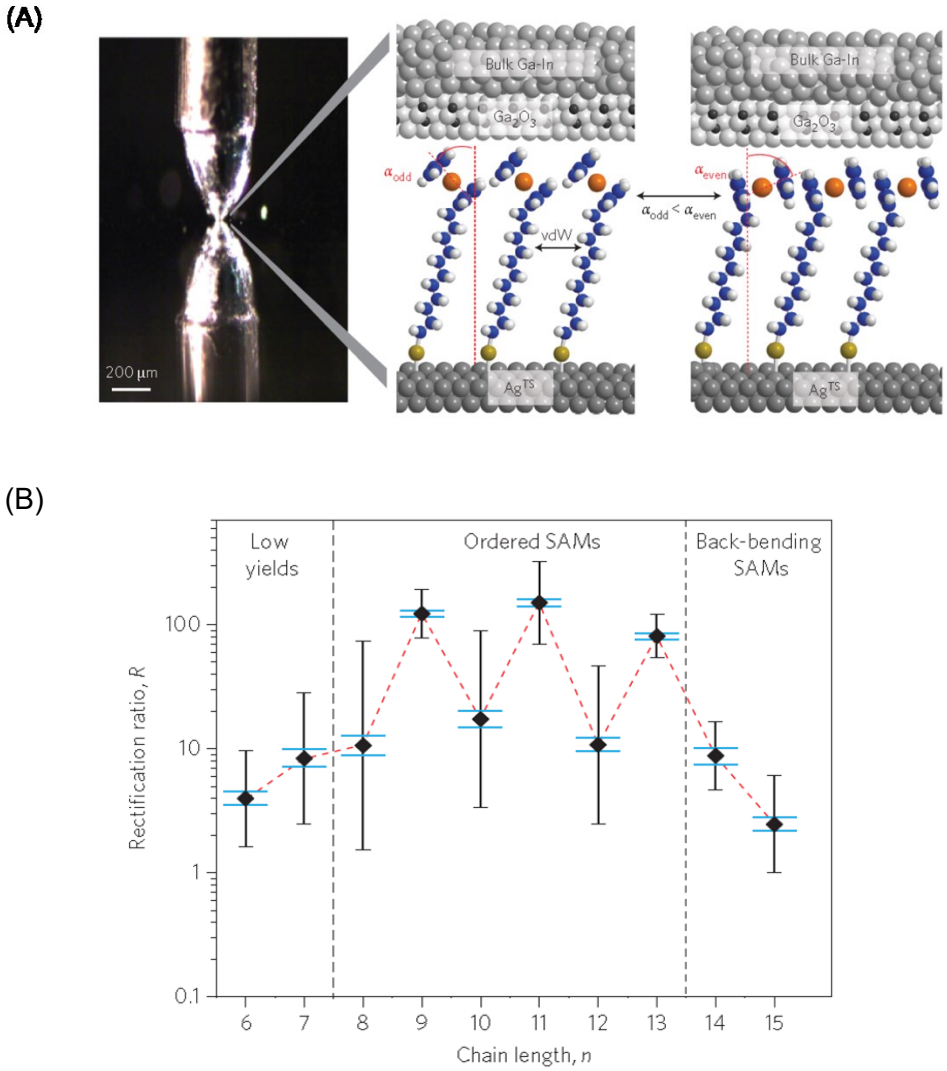

Figure 1.17. (A) Schematic illustration of junctions of Ag^{TS}-SC_nFc//Ga_2O_3/EGaIn; (B) Values of the rectification ratio R as a function of the alkyl chain length *n*. Reprinted from ref 6 and 79. Copyright 2015, American Chemical Society.

In the neutral state, molecular dynamics suggest that the alkyl chains are tilted about 20 degrees from the vertical. NEXAFS (Near Edge X-ray Absorption Fine Structure) measurements indicate that the ferrocene heads are oriented around 55 degrees from the surface normal.[6] It is also noted there is ~5° difference in the tilt angle of the ferrocene heads in the neutral state for FcC_nS SAMs of odd versus even number of methylenes (Figure 1.18). On gold, the ferrocene headgroups are standing more upright towards the surface normal when

n is even-numbered, which results in improvements in the computed SAM packing energy. The odd-even effect in the tilt angle of the Fc units in turn results in an odd-even effect in the surface dipole, work function, rectification ratio, tunneling current, and SAM packing energy (Figure 1.19).[6] Less steric hindrance between the Fc termini when ferrocenes stand more upright causes a more ordered supramolecular structure which is less susceptible to substrate defects. A completely reverse trend is observed on Ag.

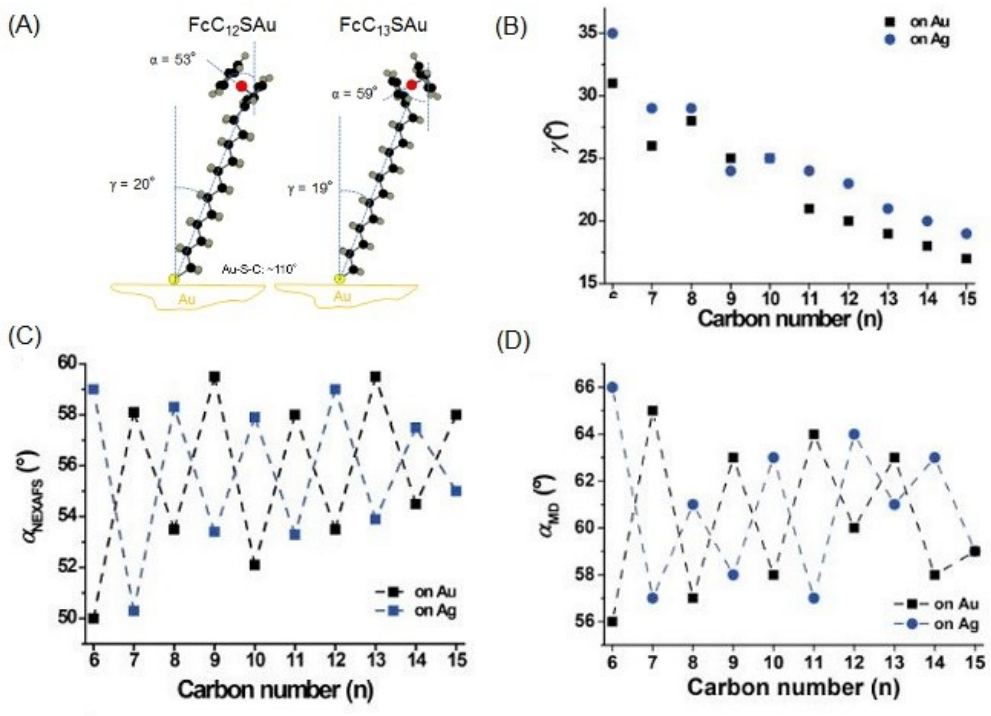

Figure 1.18. (A) Schematic illustration of the odd-even difference in the orientation of the terminal ferrocene unit suggested by NEXAFS and MD simulations in FcC_nSAu SAMs of n_{even} and n_{odd} for an ideal all-trans extended conformation of the alkyl chains. (B) Tilt angle (γ) of the linear backbone of the alkyl chain away from the surface normal as a function of the number of methylenes (n), is estimated by molecular dynamics. (C) The ferrocene tilt angles (α_{NEXAFS}) as a function of n are derived from the angular dependence of the NEXAFS spectra. (D) The ferrocene tilt angles (α_{MD}) calculated by MD simulations. (B), (C) and (D) are from ref 6. Copyright 2015, American Chemical Society.

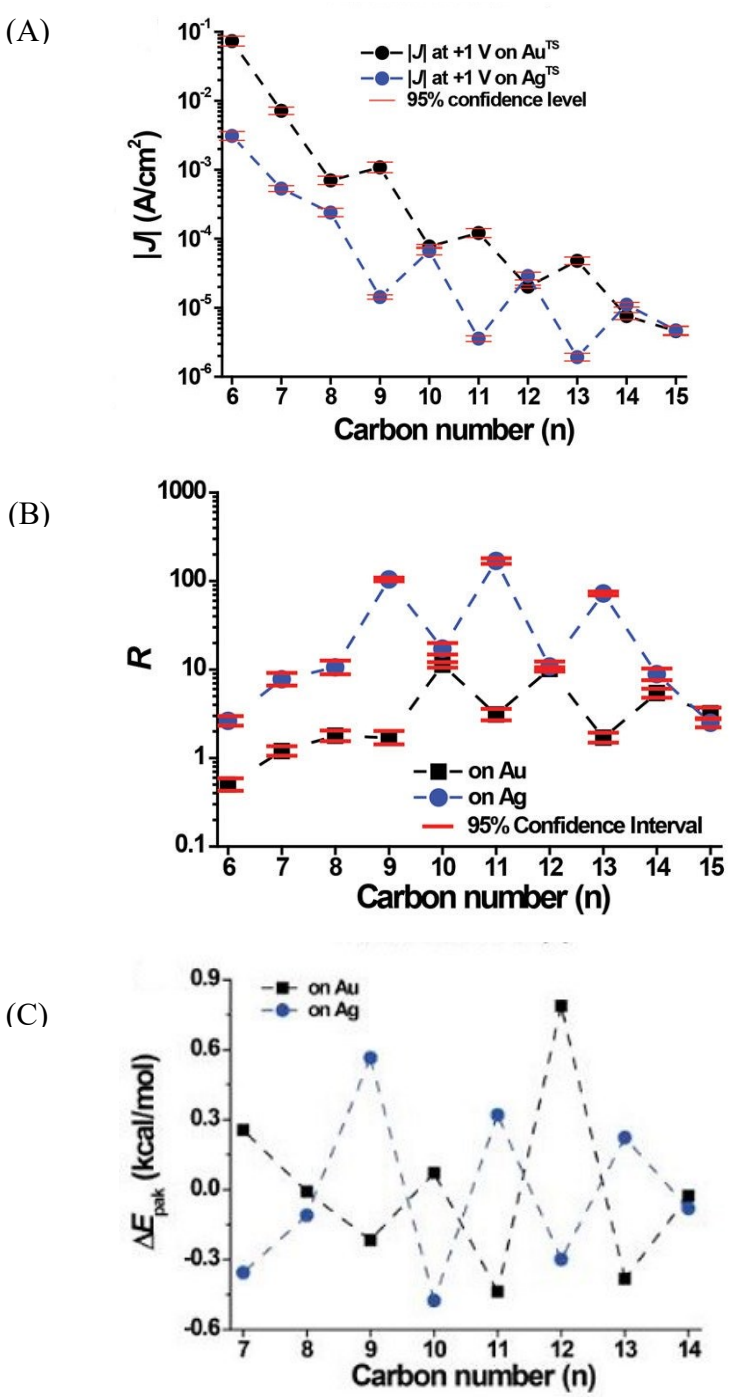

Figure 1.19. Characteristics of junctions with SAMs of SC_nFc on Au and Ag as a function of *n*. (A) Tunneling current, |J| of the junctions at +1.0 V, (B) Rectification ratio, R and (C) Calculated SAM packing energy. Reproduced from 6. Copyright 2015, American Chemical Society.

Although several studies have focused on the electrical and electrochemical properties of ferrocenylalkanethiolate SAMs, there is a lack of information concerning the FcC_nSAu packing structure and conformational order, and how the alkyl chain length impacts the Fc^+X^- ion pair formation and the redox-induced SAM reorganization.

1.5 SAM Characterization

1.5.1 Surface Plasmon Resonance (SPR)

During the last two decades, surface plasmon resonance (SPR) has become a remarkably popular label-free analytical tool due to its high sensitivity and relatively simple instrumentation required.[88-93] SPR is an all-optical technique used to follow in situ and in real time molecular processes occurring on metal and dielectric interfaces in gas or liquid environments. The detection relies on the resonant excitation of freely oscillating electrons (plasmons) at the metal/dielectric interface by *p*-polarized light, resulting in a surface-bound evanescent electromagnetic wave of optical frequency (Figure 1.20).[94] The resonance excitation is extremely sensitive to the refractive index (RI) of the medium adjacent to the metal surface as small as 10^{-7} with a time resolution of seconds[97], which leads SPR to many potential applications in the field of chemistry, physics and biology, for example, it, as a surface-oriented technique, has shown great potential for affinity biosensors, allowing the examination of the kinetics of biomolecular interactions. SPR can detect the adsorption or desorption of molecules from the metal sensing surface and changes in the molecular orientation of the adsorbate with sub-monolayer sensitivity. This makes the SPR technique ideal for accurately monitoring molecular events occurring at the interface.

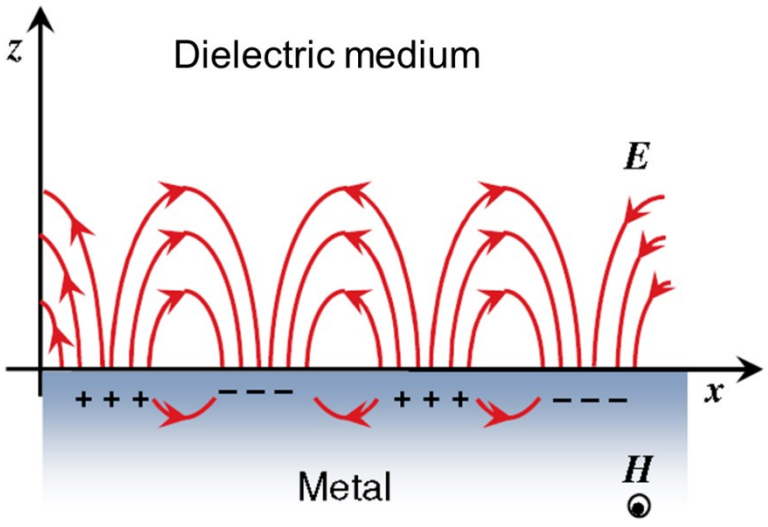

Figure 1.20. Schematic illustration of the electromagnetic field with surface plasmons traveling along a metal/dielectric interface. From ref 94. Copyright IOP science, 2012.

SPR is a quantum phenomenon, which has been reviewed extensively in the literature.[90, 95-97] and can readily be understood with Maxwell equation for the electromagnetic waves. In the classical model, a semi-infinite media with frequency-dependent dielectric functions ε_i (ω) separated by a plane at $z = 0$ is considered. Maxwell's solutions, "surface waves", at the boundary between the two media have the relation:

$$E_i = (E_{xi}, 0, E_{zi}) exp^{i(k_{xi}x + k_{zi}z - \omega t)} \quad (4)$$

$$H_i = (0, H_{yi}, 0) exp^{i(k_{xi}x + k_{zi}z - \omega t)} \quad (5)$$

Where E and H represent the electric and magnetic fields, k_i is the magnitude of the wave vector and the parameter i denotes the different media (i = m for the metal and i = d for the dielectric medium). Even though every lineally polarized radiation can be represented as a superposition of p- and s-polarization, it is only the p-polarization that can lead to a charge density oscillation in the z-direction at an interface, as shown in Figure 1.20.

The interfacial boundary conditions require that the E and H fields should be continuous at the interface and results in a nontrivial solution:

$$\frac{k_{z1}}{k_{z2}} = -\frac{\varepsilon_2}{\varepsilon_1} \quad (6)$$

where k_{z1} and k_{z2} are the wave vectors at the interface between two media. This equation indicates that the surface plasmons can only exist at the interface between two media with dielectric constants of opposite sign, so the case where one media is dielectric ($\varepsilon_d > 0$) and the other is a metal ($\varepsilon_m < 0$) follows the rule. The interfacial boundary conditions also stipulate the continuity of the two-dimensional wave vector, i.e. $k_{xm} = k_{xd} = k_x$, and for any electromagnetic mode, the wave vector k_{zi} is given by:

$$k_{zi} = \sqrt{\varepsilon_i (\frac{\omega}{c})^2 - {k_x}^2} \quad (7)$$

With the equations (6) and (7), the wave vector of the surface plasmons at the metal/dielectric interface is given by:

$$k_x = k_{sp} = \frac{\omega}{c}\sqrt{\frac{\varepsilon_m \cdot \varepsilon_d}{(\varepsilon_m + \varepsilon_d)}} \quad (8)$$

where both the dielectric functions and wave vectors are complex. The real part of k_x indicates the finite surface plasmon propagation and the imaginary part describes the dampening of the surface plasmon in the metal and dielectric media. Since the refractive index (n) is defined as the square root of its dielectric constant ($n = \sqrt{\varepsilon}$), the surface plasmon resonance also depends on n.

The coupling and excitation of the surface resonance plasmons require that the both angular frequency and momentum are matched with that of the incident photon and surface plasmon, which means that the wave vectors of the photons and surface plasmons are equal in both magnitude and direction with the same wave frequency. The momentum of a free photon propagating in a dielectric medium is given as

$$k_{ph} = (\frac{\omega}{c_d})\sqrt{\varepsilon_d} \quad (9)$$

where the dispersion of the photons is described by the light line ($\omega = c_d k$). While the wave vector of the plasmon is bound to the planar metal/dielectric interface, it is only the part in parallel direction that is taken into consideration by

$$k_{ph}^{x} = (\frac{\omega}{c_d}) \sin\Theta\sqrt{\varepsilon_d} \quad (10)$$

where Θ is the incident angle of incidence. The wave vector k_{ph}^{x} can be tuned to equate the surface plasmon k_{sp} by changing the incidence angle (Θ). Nevertheless, it is obvious that there is no angle of incidence on the metal surface for which the horizontal component of light matches the surface plasmon for any value of Θ and ω. In other words, the momentum of the photon (k_{ph}^{x}) in a dielectric medium is always smaller than the momentum of the surface plasmon (k_{sp}) along the interface between the same medium and the metal.

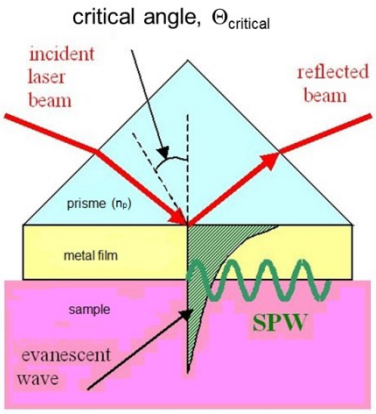

Figure 1.21. Schematic illustration of the Kretschmann attenuated total reflectance (ATR) geometry for the excitation of surface plasmons from ref 92. Copyright 1968, Verlag der Zeitschrift für Naturforschung.

However, there are mechanisms which make the external radiation possible to be coupled with surface plasmons, called attenuated total reflection (ATR).[91-92] Two most popular configurations of the ATR method are the Kretschmann geometry[91] and the Otto geometry.[92] In the Kretschmann geometry, a high refractive index prism with refractive index (n_p) is interfaced with a metal-dielectric waveguide consisting of a thin metal film of permittivity (ε_m) and a semi-infinite dielectric with a refractive index (n_d) where $n_d < n_p$, Figure 1.21. The effect of the more optically dense medium (prism) is to modify the wave vector of the incident light by increasing the momentum of the photons, so that the new dispersion relation of the photon is given by

$$k_{ph} = (\frac{\omega}{c_d}) \sin \Theta \sqrt{\varepsilon_p} \qquad (11)$$

With the involvement of the prism, k_{ph} can be easily modified by the refractive index of the prism. The Kretschmann configuration is one of the optical techniques which rely on the phenomenon of the total internal reflection (TIR) of light at a two-media boundary. For the incident light beam propagating through the optically dense prism, Snell's law[98] requires that at an incident angle exceeding the critical value all light will be completely reflected. As the angle of incidence approaches the critical angle, gradually improved energy accumulates in the reflected beam, and the reflectivity reaches its maximum (unity) at the critical value.

Although the incident light is internally reflected, there still exists a proportion of light that penetrates into the adjacent medium with a lower refractive index (Figure 1.21). The amplitude of this evanescent field wave decreases exponentially with increasing distance from the interface. When a high refractive index substrate is coated with a metal film of an appropriate thickness (typically 45-50 nm), the electrical field of the evanescent wave can overlap with that of the surface plasmon and energy transfer between the two waves is possible. The angle at which the phenomenon occurs is called the resonance angle, Θ_{SPR} or Θ_{min}.

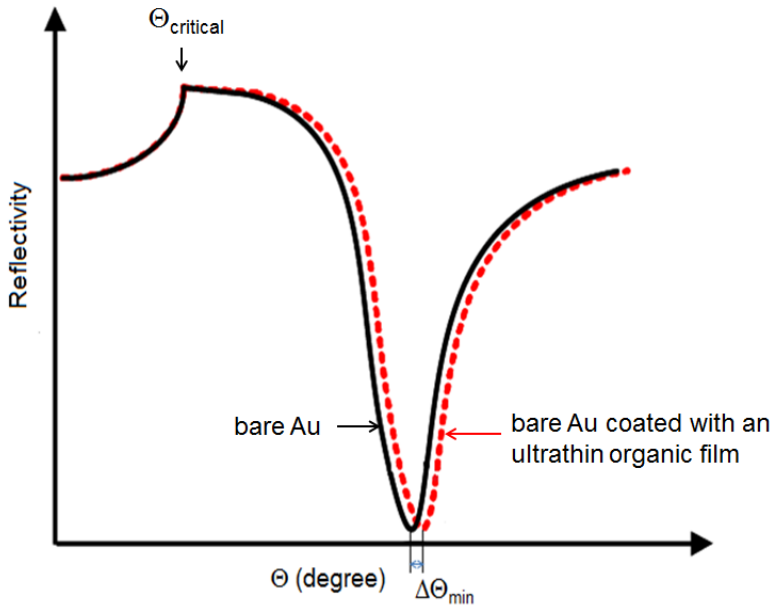

Figure 1.22. Illustration of a reflectivity-incident angle (R-Θ) or SPR curves.

When the reflectivity is monitored as a function of Θ_i, it shows a minimum in the reflectance that corresponds to the resonant coupling of photon energy by the surface plasmon, as shown in Figure 1.22. Θ_{min} is extremely sensitive to the refractive index of the solution directly adjacent to the metal film, and a shift in the resonance angle ($\Delta\Theta_{min}$) is observed if the refractive index of the medium changes. Because it senses evanescent waves, SPR-based sensor responds to the refractive index of the analyte within a depth of 200 nm from the sensor

(metal) surface. Notably, layer thickness changes of 1-2 Å or nanograms of adsorbed mass are readily measured.

The reflectivity vs. Θ profiles are generally analyzed using a multilayer Fresnel model to obtain the structural information at the interface. It is assumed that each phase is homogeneous and parallel to the planar interface. Moreover, the analysis requires knowledge of the refractive index in each phase. Gold and silver are the two most frequently used metals for SPR, with the inherent stability of gold in air and a sharper peak is provided by silver. The metal surface can act as a surface for chemisorption or deposition of an organic film with specific chemical functionality.

In the work herein, the SPR is used to detect redox-induced changes in molecular orientation of the terminal moieties by the changes in dielectric constant. Instead of using independently, SPR can also be coupled to cyclic voltammetry to follow in situ and in real time the oxidation and reduction on surface and demonstrate the possible effects on the surface-confined redox and ion-pairing reactions, and oxidation-induced changes of the SAM structure. If the study targets are SAMs, the modified metal substrate acts as both the working electrode in a conventional three-electrode cell and as the surface plasmon supporting surface (Figure 1.23). Changes in the thickness of the SAM cause an increase in the resonance angle (Figure 1.24A), and it is this angle shift which is monitored with applied potential during the cyclic voltammetric scans. The angle of minimum reflectivity, or resonance angle, can be tracked as the SAM is cycled between the reduced and oxidized state (Figure 1.24B).

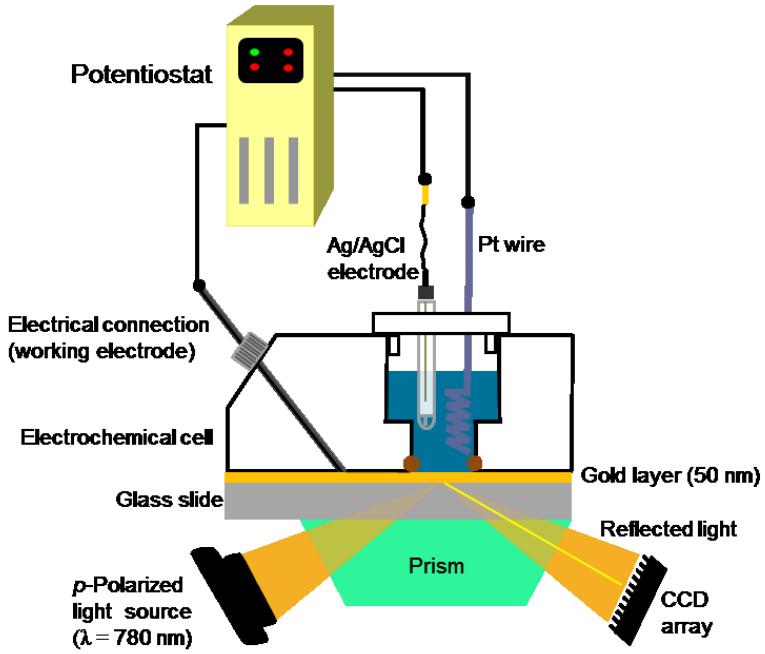

Figure 1.23 Illustration of the electrochemical surface plasmon resonance (EC-SPR) setup used for the investigations of the FcC_nSAu SAMs.

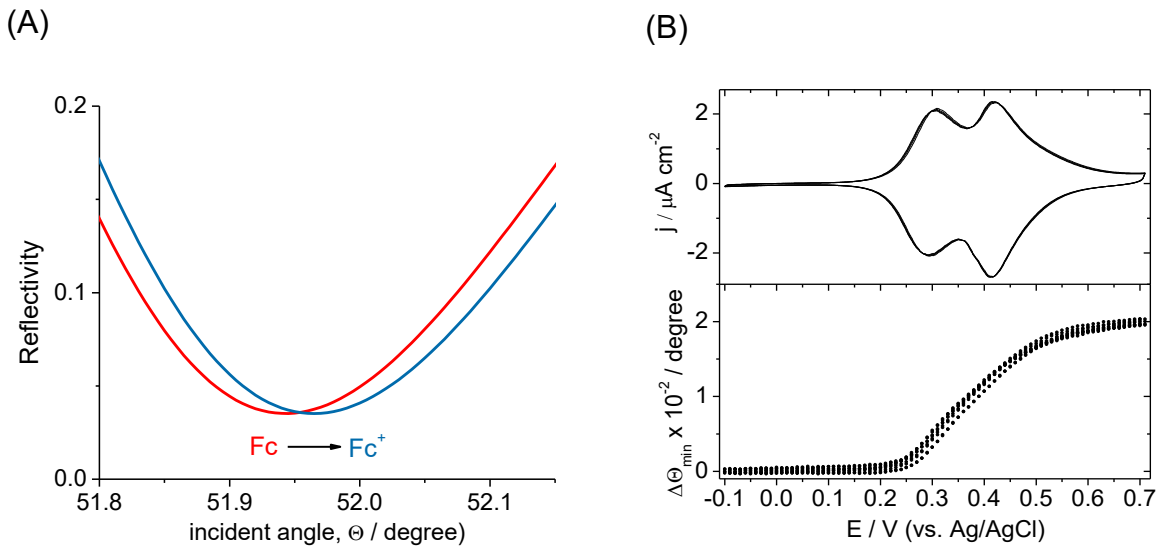

Figure 1.24. (A) Surface plasmon resonance angle shifts to higher value when Fc is oxidized into Fc^+ due to an oxidation-induced structural rearrangement of the SAM. (B) Current density j and resonance angle change $\Delta\Theta_{min}$ for five consecutive voltammetric cycles of a $FcC_{16}SAu$ SAM in 0.1 M $NaClO_{4(aq)}$ are shown.

1.5.2 Cyclic Voltammetry (CV)

Cyclic voltammetry (CV) is a potentiodynamic electrochemical technique used to investigate the mechanisms of heterogeneous electron transfer at molecule-electrode interfaces. In a CV experiment, the working electrode potential is ramped by sweeping the voltage linearly between two set potentials with a sweep rate (ν) ranging from 1 mV/s to about 1000 V/s with conventional electrodes, and up to 10^6 V/s with UMEs. The current at the working electrode is customarily plotted against the applied voltage in a typical cyclic voltammogram. (Figure 1.25) The parameters of interest (peak position E_p, peak current i_p, and peak area) are shown in Figure 1.26. Before an experiment, the SAM-modified working electrode is thoroughly rinsed with the incubation solvent to remove all of the physisorbed redox-active species from the surface, so that there is no redox-active residue that can diffuse to or from the electrode surface.[99] Consequently, the current response in CV arises completely from the immobilized redox moieties.

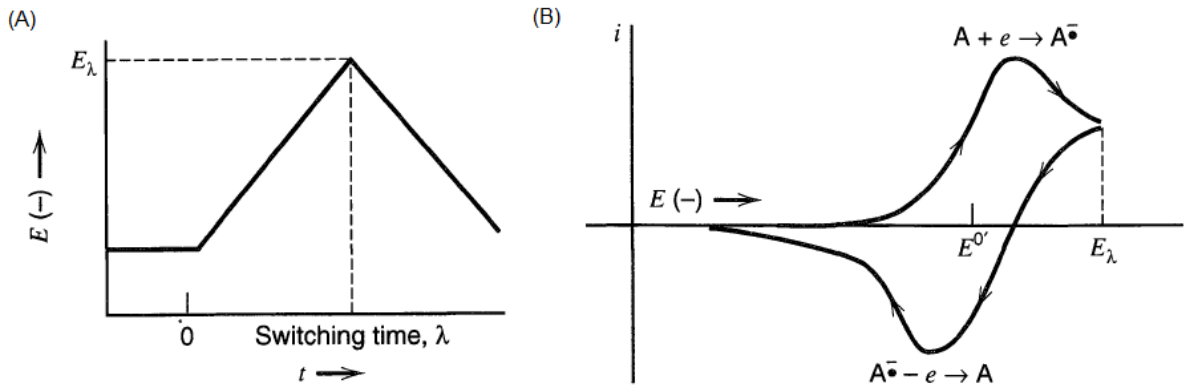

Figure 1.25. (A) Cyclic potential sweep. (B) Typical reversible cyclic voltammogram for a soluble redox species at a bare electrode surface. Reprinted from ref 99. Copyright 2001 John Wiley & Sons, Inc.

The so-called ideal CV for a surface-tethered species shows single, reversible and symmetric redox peaks for a one-step one-electron process.[79] The average of the anodic (E_a)

and cathodic (E_c) peaks of the cyclic voltammograms is used as the apparent formal redox potential ($E^{o\prime}$).

$$E^{o\prime} = \frac{E_a + E_c}{2} \tag{12}$$

For an ideal Nernstian reaction where species interact independently and the rate of electron transfer is rapid on the experimental time scale, the CV has several distinct characteristics. The difference between the oxidation (anodic) peak and reduction (cathodic) peak potentials is zero ($\Delta E_p = 0$), the ratio of the anodic to cathodic peak current is unity ($I_a/I_c = 1$), the anodic and cathodic peak currents, I_a and I_c, are proportional to the scan rate (v) and the full width at half-maximum of the redox peaks (ΔE_{FWHM}) is around 90.6 mV at 25 °C for a one electron transfer. In this case, the peak current (I_p) is given by:

$$I_p = \frac{n^2F^2}{4RT} vA\Gamma = \frac{nFvQ}{4RT} \tag{13}$$

where n is the number of electrons transferred, F is the Faraday constant (96 485 C mol^{-1}), v is the scan rate, R is the gas constant, T is the absolute temperature, A is the true contact surface area which is probed electrochemically and Γ is the surface coverage or concentration of the redox-active components (in mol·cm^{-2}). The surface coverage or concentration of the redox species can be readily obtained from the Faradaic charge Q using Equation 14:

$$\Gamma = Q_a/nFA \tag{14}$$

where Q_a is the charge associated with ferrocene oxidation determined by integration of the sigmoidal baseline-corrected anodic peak(s), n = 1 for the oxidation of ferrocene to ferrocenium. The full-width at half-maximum follows the general relationship:

$$\Delta E_{FWHM} = 3.53\frac{RT}{nF} = \frac{90.6}{n} \text{ mV} \tag{15}$$

Nearly ideal cyclic voltammograms are only observed, however, when the ferrocene heads are sufficiently diluted or dispersed with electro-inactive molecules (i.e. *n*-alkanethiolates). (Figure 1.26)

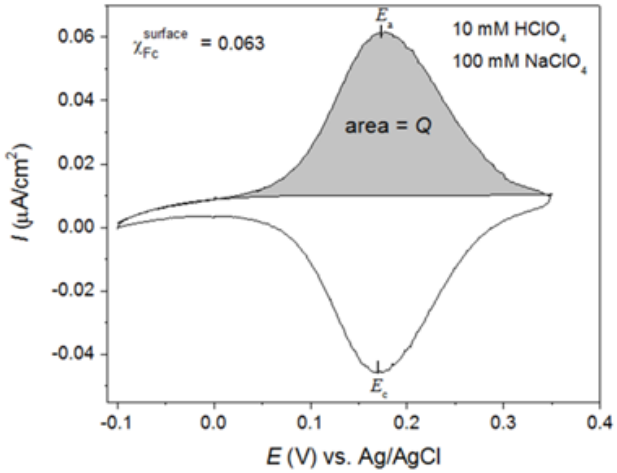

Figure 1.26. Characteristics of a cyclic voltammogram of a redox-active component adsorbed to an electrode surface.

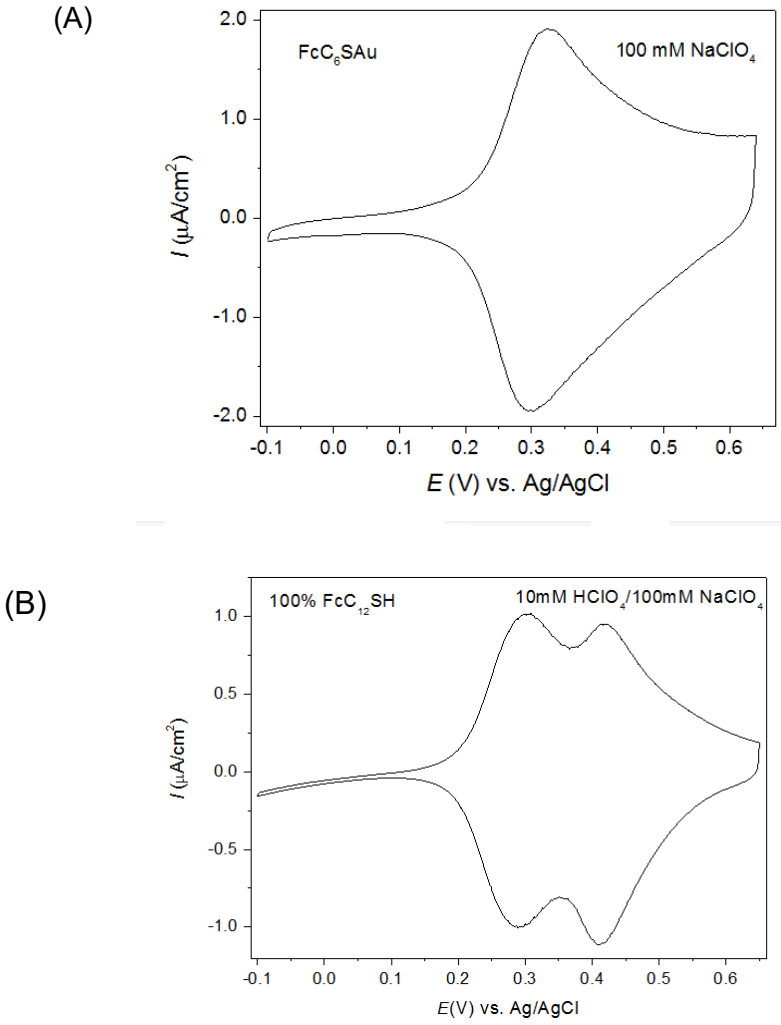

Figure 1.27. Characteristics of a cyclic voltammogram of a redox-active component adsorbed on an electrode surface. (A) A peak-broadening CV scan of FcC_6SAu SAM in perchlorate solution. (B) A CV of a single component $FcC_{12}SAu$ SAM with peak splitting. CVs in (A) and (B) were scanned at 10 mV s^{-1}.

In general, the aforementioned ideal electrochemical behavior is rarely observed in single-component SAMs of ferrocene-alkanethiolates ($S(CH_2)_nFc$). Deviations include peak broadening (Figure 1.27 A) or narrowing, peak splitting or multiplicity (Figure 1.27 B), and non-zero anodic-to-cathodic peak separation. These non-ideal behaviors are usually due to the inhomogeneity of the SAM structure and lateral interactions between the ferrocenes.[79] One

explanation for the peak splitting is the presence of different microenvironments induced by defects from the metal substrate (grain boundaries, surface roughness, polycrystallinity).[1] This results in two phases of different packing densities and differing redox potentials.

Another explanation for the peak splitting is proposed by Nijhuis and coworkers.[79] They ascribe the peak splitting and broadening to the buildup of strain in the SAM because of the mismatch in the sizes of the Fc heads and alkyl tails. The lower potential peak represents Fc units directly in contact with the electrolyte solution and interacting with neighboring Fc units, and a second peak at higher potential is from partially-buried Fc units.

1.5.3 Electrochemical Impedance Spectroscopy (EIS)

Instead of studying electrode reactions through large perturbations by imposing potential sweeps, potential steps or current steps far from equilibrium, another approach is to perturb the cell with a small-magnitude alternating signal and observe the system at steady state, which makes it possible to conduct higher precision measurements over a wide frequency range (10^{-4} to 10^{6} Hz) thereby providing important simplification over kinetics and diffusion studies.[99] Faradaic impedance is one of the prototypical experiments, in which the potential of the working electrode is fixed with existence of both forms of the redox species. The impedance is measured as a function of frequency of the ac source and the technique is referred to as electrochemical impedance spectroscopy (EIS). In this section, a brief introduction on EIS, which is based on circuit analysis, is given by using two ideal cases. EIS involves excitation signals E_{ac} of very high frequency (1 Hz to 0.1MHz) and relies on the fact that current-overpotential relation is virtually linear at low overpotentials, in which excitation at a frequency ω provides a current with the same frequency, ω.

A pure sinusoidal voltage (e) can be expressed in equation 16 and shown in Figure 1.28 A, where ω is the angular frequency.

$$e = E \sin \omega t \tag{16}$$

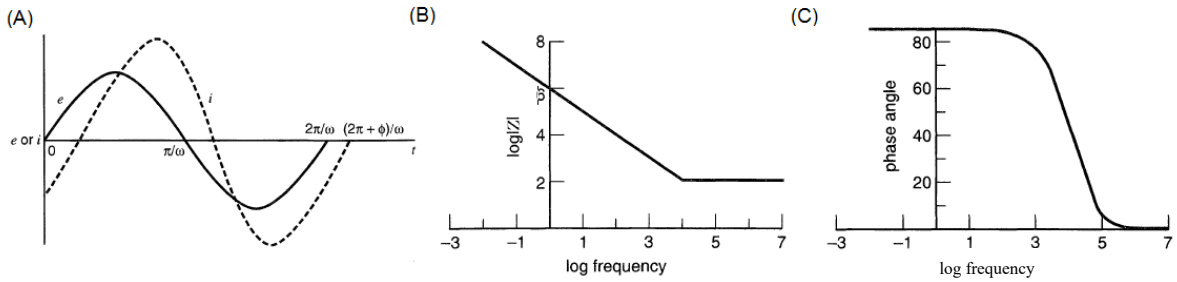

Figure 1.28. (A) Phasor diagram for alternating current and voltage signals at frequency ω. (B) (C) An impedance response displayed on Bode plots for a series circuit with R = 100 Ω and C = 1 μF. Reprinted from ref 99. Copyright 2001 John Wiley & Sons, Inc.

Two related sinusoidal signals, the current (i) and the voltage (e), are represented as phasors (rotative vectors), $\dot{I}$ and $\dot{E}$, and separated by a phase angle (ϕ), with E taken as the amplitude of the sin wave. Similarly, the current can be generally expressed as:

$$i = I\sin(\omega t + \phi) \tag{17}$$

At a given frequency controlled by the frequency generator, the phase angle is constant. The value of ϕ can be regarded as the delay between the perturbation applied on the system and the generation of the measured signal. Depending on the electrochemical system, it represents the current which will respond rapidly or slowly toward the applied potential.

Since Ohm's law always holds, a pure resistance (R) with $\phi = 0$ (limit case 1) is involved, so the current is given by:

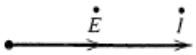

$$i = \frac{E}{R}\sin(\omega t) \tag{18}$$

Suppose the resistor is replaced by a pure capacitance (C), and $q = Ce$ (or $i = C(de/dt)$); thus

$$i = \omega CE\cos\omega t \tag{19}$$

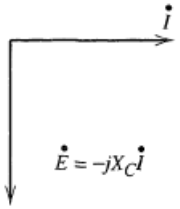

$$i = \frac{E}{X_C}\sin(\omega t + \frac{\pi}{2}) \qquad \text{with } \phi = 90° \tag{20}$$

where X_C is the capacitive reactance and $X_C = 1/\omega C$. Since the vector diagram is expressed on a plane, phasors can also be defined by complex numbers representing a sinusoidal function and simplifying the equations. Components along the abscissa are the real part and those along the ordinate are assigned as imaginary; however both of the components are measurable. In the case where R is series with C with a sinusoidal source, the voltage on resistance ($\dot{E_R}$) is displayed on real part and the voltage ($\dot{E}c$) on capacitance is represented on imaginary part as

$$\dot{E_C} = -jX_C\dot{I} \tag{21}$$

A voltage, E, is applied across the resistance, R, and a capacitance, C, in sequence and the overall voltage equals the sum of the individual voltages from the resistor and the capacitor

$$\dot{E} = \dot{E_R} + \dot{E_C} \tag{22}$$

$$\dot{E} = \dot{I}(R - jX_C) \tag{23}$$

$$\dot{E} = \dot{I}Z \tag{24}$$

where $Z = R - jX_C$ is called the impedance. Generally, the impedance can be represented as

$$\mathrm{Z}(\omega) = \mathrm{Z_{Re}} - j\mathrm{Z_{Im}} \tag{25}$$

where Z_{Re} and Z_{Im} are the real and imaginary parts of the impedance and the magnitude of Z ($|Z|$) is given by:

$$|\mathrm{Z}|^2 = R^2 + {X_C}^2 = (\mathrm{Z_{Re}})^2 + (\mathrm{Z_{Im}})^2 \tag{26}$$

The phase angle, ϕ, is given by:

$$\tan\emptyset = \frac{\mathrm{Z_{Im}}}{\mathrm{Z_{Re}}} = \frac{\mathrm{X_C}}{\mathrm{R}} = \frac{1}{\omega RC} \tag{27}$$

The variation of the impedance with frequency is often of interest and can be shown in different ways. For example, a Bode plot displays log |Z| and ϕ as a function of log ω (Figure 1.28), and Z_{Re} and Z_{Im} are plotted against ω in a Nyquist plot.

Even though the chemical modification of metallic surfaces with immobilized electroactive species for electrochemistry makes it possible to generate barrier layers which prevent free diffusion of electroactive species to the SAMs' surface, the redox-induced molecular reorientations that occurred in odd-even chain length of typical electroactive molecules, ferrocenylalkanethiolates are still poorly understood. This work investigated the underlying mechanisms with the film thickness change induced by refractive index variations in the medium and the different packing structures of the SAMs observed by CV.

Reference

(1) Love, J. C.; Estroff, L. A.; Kriebel, J. K.; Nuzzo, R. G.; Whitesides, G. M., Self-assembled monolayers of thiolates on metals as a form of nanotechnology. *Chem. Rev.* **2005,** *105* (4), 1103-1170.

(2) Irving, D. L.; Brenner, D. W., Diffusion on a self-assembled monolayer: molecular modeling of a bound+ mobile lubricant. *J. Phys. Chem. B.* **2006,** *110* (31), 15426-15431.

(3) Ansari, S. A.; Husain, Q., Potential applications of enzymes immobilized on/in nano materials: a review. *Biotechnol. Adv.* **2012,** *30* (3), 512-523.

(4) Boussicault, F.; Robert, M., Electron transfer in DNA and in DNA-related biological processes. Electrochemical insights. *Chem. Rev.* **2008,** *108* (7), 2622-2645.

(5) Ye, S.; Sato, Y.; Uosaki, K., Redox-induced orientation change of a self-assembled monolayer of 11-ferrocenyl-1-undecanethiol on a gold electrode studied by in situ FT-IRRAS. *Langmuir* **1997,** *13* (12), 3157-3161.

(6) Yuan, L.; Thompson, D.; Cao, L.; Nerngchangnong, N.; Nijhuis, C. A., One carbon matters: The origin and reversal of odd–even effects in molecular diodes with self-assembled monolayers of ferrocenyl-alkanethiolates. *J. Phys. Chem. C.* **2015,** *119* (31), 17910-17919.

(7) Bigelow, W.; Pickett, D.; Zisman, W., Oleophobic monolayers: I. Films adsorbed from solution in non-polar liquids. *J. Colloid Sci.* **1946,** *1* (6), 513-538.

(8) Ulman, A., Formation and structure of self-assembled monolayers. *Chem. Rev.* **1996,** *96* (4), 1533-1554.

(9) Bain, C. D.; Troughton, E. B.; Tao, Y. T.; Evall, J.; Whitesides, G. M.; Nuzzo, R. G., Formation of monolayer films by the spontaneous assembly of organic thiols from solution onto gold. *J. Am. Chem. Soc.* **1989,** *111* (1), 321-335.

(10) Nuzzo, R. G.; Fusco, F. A.; Allara, D. L., Spontaneously organized molecular assemblies. 3. Preparation and properties of solution adsorbed monolayers of organic disulfides on gold surfaces. *J. Am. Chem. Soc.* **1987,** *109* (8), 2358-2368.

(11) Nuzzo, R. G.; Dubois, L. H.; Allara, D. L., Fundamental studies of microscopic wetting on organic surfaces. 1. Formation and structural characterization of a self-

consistent series of polyfunctional organic monolayers. *J. Am. Chem. Soc.* **1990,** *112* (2), 558-569.

(12) Porter, M. D.; Bright, T. B.; Allara, D. L.; Chidsey, C. E., Spontaneously organized molecular assemblies. 4. Structural characterization of n-alkyl thiol monolayers on gold by optical ellipsometry, infrared spectroscopy, and electrochemistry. *J. Am. Chem. Soc.* **1987,** *109* (12), 3559-3568.

(13) Sandroff, C.; Herschbach, D., Surface-enhanced Raman study of organic sulfides adsorbed on silver: facile cleavage of sulfur-sulfur and carbon-sulfur bonds. *J. Phys. Chem.* **1982,** *86* (17), 3277-3279.

(14) Garrell, R. L.; Chadwick, J. E.; Severance, D. L.; McDonald, N. A.; Myles, D. C., Adsorption of sulfur containing molecules on gold: the effect of oxidation on monolayer formation and stability characterized by experiments and theory. *J. Am. Chem. Soc.* **1995,** *117* (46), 11563-11571.

(15) Bryant, M. A.; Pemberton, J. E., Surface Raman scattering of self-assembled monolayers formed from 1-alkanethiols: behavior of films at gold and comparison to films at silver. *J. Am. Chem. Soc.* **1991,** *113* (22), 8284-8293.

(16) Nuzzo, R. G.; Zegarski, B. R.; Dubois, L. H., Fundamental studies of the chemisorption of organosulfur compounds on gold (111). Implications for molecular self-assembly on gold surfaces. *J. Am. Chem. Soc.* **1987,** *109* (3), 733-740.

(17) Curreli, M.; Li, C.; Sun, Y.; Lei, B.; Gundersen, M. A.; Thompson, M. E.; Zhou, C., Selective functionalization of In2O3 nanowire mat devices for biosensing applications. *J. Am. Chem. Soc.* **2005,** *127* (19), 6922-6923.

(18) Laibinis, P. E.; Whitesides, G. M.; Allara, D. L.; Tao, Y. T.; Parikh, A. N.; Nuzzo, R. G., Comparison of the structures and wetting properties of self-assembled monolayers of n-alkanethiols on the coinage metal surfaces, copper, silver, and gold. *J. Am. Chem. Soc.* **1991,** *113* (19), 7152-7167.

(19) Bain, C. D.; Biebuyck, H. A.; Whitesides, G. M., Comparison of self-assembled monolayers on gold: coadsorption of thiols and disulfides. *Langmuir* **1989,** *5* (3), 723-727.

(20) Bourg, M.-C.; Badia, A.; Lennox, R. B., Gold− sulfur bonding in 2D and 3D self-assembled monolayers: XPS characterization. *J. Phys. Chem. B.* **2000,** *104* (28), 6562-6567.

(21) Dubois, L. H.; Nuzzo, R. G., Synthesis, structure, and properties of model organic surfaces. *Annu. Rev. Phys. Chem.* **1992,** *43* (1), 437-463.

(22) Ulman, A., Surface absorption of monolayers. *MRS Bulletin* **1995,** *20* (6), 46-51.

(23) Schreiber, F., Structure and growth of self-assembling monolayers. *Prog. Surf. Sci.* **2000,** *65* (5), 151-257.

(24) Bain, C. D.; Whitesides, G. M., A study by contact angle of the acid-base behavior of monolayers containing. omega.-mercaptocarboxylic acids adsorbed on gold: an example of reactive spreading. *Langmuir* **1989,** *5* (6), 1370-1378.

(25) Bain, C. D.; Whitesides, G. M., Correlations between wettability and structure in monolayers of alkanethiols adsorbed on gold. *J. Am. Chem. Soc.* **1988,** *110* (11), 3665-3666.

(26) Bain, C. D.; Evall, J.; Whitesides, G. M., Formation of monolayers by the coadsorption of thiols on gold: variation in the head group, tail group, and solvent. *J. Am. Chem. Soc.* **1989,** *111* (18), 7155-7164.

(27) Kawasaki, M.; Sato, T.; Tanaka, T.; Takao, K., Rapid self-assembly of alkanethiol monolayers on sputter-grown Au (111). *Langmuir* **2000,** *16* (4), 1719-1728.

(28) Peterlinz, K. A.; Georgiadis, R., In situ kinetics of self-assembly by surface plasmon resonance spectroscopy. *Langmuir* **1996,** *12* (20), 4731-4740.

(29) Bensebaa, F.; Voicu, R.; Huron, L.; Ellis, T. H.; Kruus, E., Kinetics of formation of long-chain n-alkanethiolate monolayers on polycrystalline gold. *Langmuir* **1997,** *13* (20), 5335-5340.

(30) Love, J. C.; Wolfe, D. B.; Haasch, R.; Chabinyc, M. L.; Paul, K. E.; Whitesides, G. M.; Nuzzo, R. G., Formation and structure of self-assembled monolayers of alkanethiolates on palladium. *J. Am. Chem. Soc.* **2003,** *125* (9), 2597-2609.

(31) Morgenthaler, S.; Lee, S.; Zürcher, S.; Spencer, N. D., A simple, reproducible approach to the preparation of surface-chemical gradients. *Langmuir* **2003,** *19* (25), 10459-10462.

(32) Delamarche, E.; Michel, B.; Gerber, C.; Anselmetti, D.; Güntherodt, H.-J.; Wolf, H.; Ringsdorf, H., Real-space observation of nanoscale molecular domains in self-assembled monolayers. *Langmuir* **1994,** *10* (9), 2869-2871.

(33) Strong, L.; Whitesides, G. M., Structures of self-assembled monolayer films of organosulfur compounds adsorbed on gold single crystals: electron diffraction studies. *Langmuir* **1988,** *4* (3), 546-558.

(34) Fenter, P.; Eisenberger, P.; Liang, K., Chain-length dependence of the structures and phases of CH 3 (CH 2) n− 1 SH self-assembled on Au (111). *Phys. Rev. Lett,* **1993,** *70* (16), 2447.

(35) Camillone Iii, N.; Eisenberger, P.; Leung, T.; Schwartz, P.; Scoles, G.; Poirier, G.; Tarlov, M., New monolayer phases of n-alkane thiols self-assembled on Au (111): Preparation, surface characterization, and imaging. *J. Chem. Phys.* **1994,** *101* (12), 11031-11036.

(36) Schönenberger, C.; Jorritsma, J.; Sondag-Huethorst, J.; Fokkink, L., Domain structure of self-assembled alkanethiol monolayers on gold. *J. Phys. Chem.* **1995,** *99* (10), 3259-3271.

(37) Poirier, G.; Tarlov, M., The c (4x2) superlattice of n-alkanethiol monolayers self-assembled on Au (111). *Langmuir* **1994,** *10* (9), 2853-2856.

(38) Liu, G.-y.; Salmeron, M. B., Reversible displacement of chemisorbed n-alkanethiol molecules on Au (111) surface: An atomic force microscopy study. *Langmuir* **1994,** *10* (2), 367-370.

(39) Bucher, J.-P.; Santesson, L.; Kern, K., Thermal healing of self-assembled organic monolayers: hexane-and octadecanethiol on Au (111) and Ag (111). *Langmuir* **1994,** *10* (4), 979-983.

(40) Schönenberger, C.; Sondag-Huethorst, J.; Jorritsma, J.; Fokkink, L., What Are the" Holes" in Self-Assembled Monolayers of Alkanethiols on Gold? *Langmuir* **1994,** *10* (3), 611-614.

(41) Kim, Y. T.; McCarley, R. L.; Bard, A. J., Scanning tunneling microscopy studies of gold (111) derivatized with organothiols. *J. Phys. Chem.* **1992,** *96* (18), 7416-7421.

(42) Widrig, C. A.; Alves, C. A.; Porter, M. D., Scanning tunneling microscopy of ethanethiolate and n-octadecanethiolate monolayers spontaneously absorbed at gold surfaces. *J. Am. Chem. Soc.* **1991,** *113* (8), 2805-2810.

(43) Dubois, L. H.; Zegarski, B. R.; Nuzzo, R. G., Molecular ordering of organosulfur compounds on Au (111) and Au (100): Adsorption from solution and in ultrahigh vacuum. *J. Chem. Phys.* **1993,** *98* (1), 678-688.

(44) Poirier, G. E., Characterization of organosulfur molecular monolayers on Au (111) using scanning tunneling microscopy. *Chem. Rev.* **1997,** *97* (4), 1117-1128.

(45) Poirier, G., Mechanism of formation of Au vacancy islands in alkanethiol monolayers on Au (111). *Langmuir* **1997,** *13* (7), 2019-2026.

(46) Camillone III, N.; Chidsey, C. E.; Liu, G. y.; Scoles, G., Superlattice structure at the surface of a monolayer of octadecanethiol self-assembled on Au (111). *J. Chem. Phys.* **1993,** *98* (4), 3503-3511.

(47) Stroeve P., Self-Assembled Monolayers: Adsorption and Desorption from Alkanethiols on Gold. *Structure* **2009,** *3*, R30.

(48) Bhushan, B.; Kawata S., *Applied scanning probe methods VI: Characterization*; Springer: Berlin Heidelberg, **2007**.

(49) Snyder, R.; Maroncelli, M.; Strauss, H.; Hallmark, V., Temperature and phase behavior of infrared intensities: the poly (methylene) chain. *J. Phys. Chem.* **1986,** *90* (22), 5623-5630.

(50) Snyder, R.; Strauss, H.; Elliger, C., Carbon-hydrogen stretching modes and the structure of n-alkyl chains. 1. Long, disordered chains. *J. Phys. Chem.* **1982,** *86* (26), 5145-5150.

(51) Camillone III, N.; Chidsey, C. E.; Liu, G. y.; Putvinski, T.; Scoles, G., Surface structure and thermal motion of n-alkane thiols self-assembled on Au (111) studied by low energy helium diffraction. *J. Chem. Phys.* **1991,** *94* (12), 8493-8502.

(52) Gutmann, F.; Johnson, C.; Keyzer, H.; Molnár, J., Charge transfer complexes in microorganisms. *Charge Transfer Complexes in Biological Systems. Marcel Dekker Inc, USA* **1997**, 443-488.

(53) Ertl, G.; Knözinger, H.; Weitkamp, J., *Handbook of Heterogeneous Catalysis*; Wiley-VCH: Weinheim, **1997**.

(54) Yousaf, M. N.; Mrksich, M., Diels− Alder Reaction for the Selective Immobilization of Protein to Electroactive Self-Assembled Monolayers. *J. Am. Chem. Soc.* **1999,** *121* (17), 4286-4287.

(55) Mrksich, M.; Whitesides, G. M., Using self-assembled monolayers to understand the interactions of man-made surfaces with proteins and cells. *Annu. Rev. Biophys. Biom.* **1996,** *25* (1), 55-78.

(56) Chidsey, C. E.; Bertozzi, C. R.; Putvinski, T.; Mujsce, A., Coadsorption of ferrocene-terminated and unsubstituted alkanethiols on gold: electroactive self-assembled monolayers. *J. Am. Chem. Soc.* **1990,** *112* (11), 4301-4306.

(57) Chidsey, C. E., Free Energy and Temperature Dependence of Electron Transfer at the Metal/Electrolyte Interface. *Science* **1991,** *251* (4996), 919-922.

(58) Tran, E.; Rampi, M. A.; Whitesides, G. M., Electron Transfer in a Hg-SAM//SAM-Hg Junction Mediated by Redox Centers. *Angew. Chem. Intl. Ed.* **2004,** *43* (29), 3835-3839.

(59) Chidsey, C. E.; Murray, R. W., Electroactive polymers and macromolecular electronics. *Science* **1986,** *231*, 25-32.

(60) Salomon, A.; Cahen, D.; Lindsay, S.; Tomfohr, J.; Engelkes, V. B.; Frisbie, C. D., Comparison of electronic transport measurements on organic molecules. *Adv. Mater.* **2003,** *15* (22), 1881-1890.

(61) Beebe, J. M.; Engelkes, V. B.; Miller, L. L.; Frisbie, C. D., Contact resistance in metal− molecule− metal junctions based on aliphatic SAMs: Effects of surface linker and metal work function. *J. Am. Chem. Soc.* **2002,** *124* (38), 11268-11269.

(62) Valincius, G.; Niaura, G.; Kazakevičienė, B.; Talaikytė, Z.; Kažemėkaitė, M.; Butkus, E.; Razumas, V., Anion effect on mediated electron transfer through ferrocene-terminated self-assembled monolayers. *Langmuir* **2004,** *20* (16), 6631-6638.

(63) Lee, L. Y. S.; Sutherland, T. C.; Rucareanu, S.; Lennox, R. B., Ferrocenylalkylthiolates as a probe of heterogeneity in binary self-assembled monolayers on gold. *Langmuir* **2006,** *22* (9), 4438-4444.

(64) Rowe, G. K.; Creager, S. E., Redox and ion-pairing thermodynamics in self-assembled monolayers. *Langmuir* **1991,** *7* (10), 2307-2312.

(65) Ju, H.; Leech, D., Effect of electrolytes on the electrochemical behaviour of 11-(ferrocenylcarbonyloxy) undecanethiol SAMs on gold disk electrodes. *Phys. Chem. Chem. Phys.* **1999,** *1* (7), 1549-1554.

(66) Uosaki, K.; Sato, Y.; Kita, H., Electrochemical characteristics of a gold electrode modified with a self-assembled monolayer of ferrocenylalkanethiols. *Langmuir* **1991,** *7* (7), 1510-1514.

(67) Yokota, Y.; Yamada, T.; Kawai, M., Ion-pair formation between ferrocene-terminated self-assembled monolayers and counteranions studied by force measurements. *J. Phys. Chem. C.* **2011,** *115* (14), 6775-6781.

(68) Kondo, T.; Okamura, M.; Uosaki, K., Anion effect on the electrochemical characteristics of a gold electrode modified with a self-assembled monolayer of ferrocenylhexanethiol in aqueous and dichloromethane solutions. *J. Organomet. Chem.* **2001,** *637*, 841-844.

(69) Rowe, G. K.; Creager, S. E., Interfacial solvation and double-layer effects on redox reactions in organized assemblies. *J. Phys. Chem.* **1994,** *98* (21), 5500-5507.

(70) Conway, B. E., *Ionic Hydration in Chemistry and Biophysics*; Elsevier Science Ltd: New York, **1981**; Vol. 12.

(71) Kazakevičienė, B.; Valincius, G.; Niaura, G.; Talaikytė, Z.; Kažemėkaitė, M.; Razumas, V.; Plaušinaitis, D.; Teišerskienė, A.; Lisauskas, V., Mediated oxidation of ascorbic acid on a homologous series of ferrocene-terminated self-assembled monolayers. *Langmuir* **2007,** *23* (9), 4965-4971.

(72) Viana, A.; Jones, A.; Abrantes, L.; Kalaji, M., Redox induced orientational changes in a series of short chain ferrocenyl alkyl thiols self-assembled on gold (111) electrodes. *J. Electroanal. Chem.* **2001,** *500* (1), 290-298.

(73) Cruanes, M. T.; Drickamer, H. G.; Faulkner, L. R., Characterization of charge transfer processes in self-assembled monolayers by high-pressure electrochemical techniques. *Langmuir* **1995,** *11* (10), 4089-4097.

(74) Nerngchamnong, N.; Yuan, L.; Qi, D.-C.; Li, J.; Thompson, D.; Nijhuis, C. A., The role of van der Waals forces in the performance of molecular diodes. *Nat. Nanotechnol.* **2013,** *8* (2), 113-118.

(75) Fracasso, D.; Valkenier, H.; Hummelen, J. C.; Solomon, G. C.; Chiechi, R. C., Evidence for quantum interference in SAMs of arylethynylene thiolates in tunneling junctions with eutectic Ga–In (EGaIn) top-contacts. *J. Am. Chem. Soc.* **2011,** *133* (24), 9556-9563.

(76) Reus, W. F.; Nijhuis, C. A.; Barber, J. R.; Thuo, M. M.; Tricard, S.; Whitesides, G. M., Statistical tools for analyzing measurements of charge transport. *J. Phys. Chem. C.* **2012,** *116* (11), 6714-6733.

(77) Felgenhauer, T.; Rong, H.-T.; Buck, M., Electrochemical and exchange studies of self-assembled monolayers of biphenyl based thiols on gold. *J. Electroanal. Chem.* **2003,** *550*, 309-319.

(78) Yu, X.; Wilhelmi, O.; Moser, H. O.; Vidyaraj, S. V.; Gao, X.; Wee, A. T.; Nyunt, T.; Qian, H.; Zheng, H., New soft X-ray facility SINS for surface and nanoscale science at SSLS. *J. Electron. Spectrosc. Relat. Phenom.* **2005,** *144*, 1031-1034.

(79) Nerngchamnong, N.; Thompson, D.; Cao, L.; Yuan, L.; Jiang, L.; Roemer, M.; Nijhuis, C. A., Nonideal Electrochemical Behavior of Ferrocenyl–Alkanethiolate SAMs Maps the Microenvironment of the Redox Unit. *J. Phys. Chem. C.* **2015,** *119* (38), 21978-21991.

(80) Wong, S.-S.; Takano, H.; Porter, M. D., Mapping orientation differences of terminal functional groups by friction force microscopy. *Anal. Chem.* **1998,** *70* (24), 5209-5212.

(81) Jasper, J. J., The surface tension of pure liquid compounds. *J. Phys. Chem.* **1972,** *1* (4), 841-1010.

(82) Parikh, A. N.; Allara, D. L., Quantitative determination of molecular structure in multilayered thin films of biaxial and lower symmetry from photon spectroscopies. I. Reflection infrared vibrational spectroscopy. *J. Chem. Phys.* **1992,** *96* (2), 927-945.

(83) Chang, S.-C.; Chao, I.; Tao, Y.-T., Structure of self-assembled monolayers of aromatic-derivatized thiols on evaporated gold and silver surfaces: Implication on packing mechanism. *J. Am. Chem. Soc.* **1994,** *116* (15), 6792-6805.

(84) Graupe, M.; Takenaga, M.; Koini, T.; Colorado, R.; Lee, T. R., Oriented surface dipoles strongly influence interfacial wettabilities. *J. Am. Chem. Soc.* **1999,** *121* (13), 3222-3223.

(85) Shon, Y.-S.; Lee, S.; Colorado, R.; Perry, S. S.; Lee, T. R., Spiroalkanedithiol-based SAMs reveal unique insight into the wettabilities and frictional properties of organic thin films. *J. Am. Chem. Soc.* **2000,** *122* (31), 7556-7563.

(86) Newcomb, L. B.; Tevis, I. D.; Atkinson, M. B.; Gathiaka, S. M.; Luna, R. E.; Thuo, M., Odd–even effect in the hydrophobicity of n-alkanethiolate self-assembled monolayers depends upon the roughness of the substrate and the orientation of the terminal moiety. *Langmuir* **2014,** *30* (40), 11985-11992.

(87) Auletta, T.; van Veggel, F. C.; Reinhoudt, D. N., Self-assembled monolayers on gold of ferrocene-terminated thiols and hydroxyalkanethiols. *Langmuir* **2002,** *18* (4), 1288-1293.

(88) Brecht, A.; Gauglitz, G., Optical probes and transducers. *Biosens. Bioelectron.* **1995,** *10* (9-10), 923-936.

(89) Gauglitz, G., Opto-Chemical and Opto-Immuno Sensors. *Sensors Update* **1996,** *1* (1), 1-48.

(90) Homola, J.; Yee, S. S.; Gauglitz, G., Surface plasmon resonance sensors. *Sens. Actuators, B* **1999,** *54* (1), 3-15.

(91) Wood, R. W., XLII. On a remarkable case of uneven distribution of light in a diffraction grating spectrum. *Lond.Edinb.Dubl.Phil.Mag.* **1902,** *4* (21), 396-402.

(92) Kretschmann, E.; Raether, H., Radiative decay of non radiative surface plasmons excited by light. *Z. Naturforsch. A.* **1968,** *23* (12), 2135-2136.

(93) Otto, A., Excitation of nonradiative surface plasma waves in silver by the method of frustrated total reflection. *Z. Phys.* **1968,** *216* (4), 398-410.

(94) Zhang, J.; Zhang, L.; Xu, W., Surface plasmon polaritons: physics and applications. *J. Phys. D: Appl. Phys.* **2012,** *45* (11), 113001.

(95) Pitarke, J.; Silkin, V.; Chulkov, E.; Echenique, P., Theory of surface plasmons and surface-plasmon polaritons. *Rep. Prog. Phys.* **2006,** *70* (1), 1-54.

(96) Knoll, W., Interfaces and thin films as seen by bound electromagnetic waves. *Annu. Rev. Phys. Chem.* **1998,** *49* (1), 569-638.

(97) Davies, J., 'Surface plasmon resonance—The technique and its applications to biomaterial processes. *Nanobiology* **1994,** *3*, 5-16.

(98) Hecht, E.; Zajac, A., Optics addison-wesley. *Reading, Mass* **1974,** *19872*, 350-351.

(99) Bard, A. J.; Faulkner, L. R.; Leddy, J.; Zoski, C. G., *Electrochemical Methods: Fundamentals and Applications*; Wiley: New York, **2001**; Vol. 2.

Chapter 2. Experimental Section

2.1 Materials

The procedures for the synthesis of the ferrocenylalkanethiols ($Fc(CH_2)_nSH$, henceforth referred to as FcC_nSH), where n = 6−16, and accompanying characterization data are provided as Supporting Information. The preparations of ferrocenylalkanethiols are accomplished by Dr. Violeta Doader from Mcgill Univerversity. The FcC_nSH precursors were stored in sealed vials at 4 °C. All other chemicals used were of reagent grade. Electrolyte solutions were prepared from ultrapure water of resistivity of 18.2 MΩ cm and total organic carbon of ≤ 5 ppb (Milli-Q Gradient system).

2.2 Choice of FcC_nSH Chain Lengths and Gold Substrates

We used FcC_nSHs of chain lengths n = 6–16 based on literature reports which demonstrate odd-even effects in the electron transport properties of FcC_nSAg-based tunneling junctions for n = 8–13,[1] Faradaic electrochemistry of FcC_nSAu SAMs between n = 5–13,[2] and average tilt angle of the ferrocene terminus for n = 2–15 (longer chain lengths were not investigated).[2]

Polycrystalline gold thin films supported on glass substrates were used for the EC-SPR measurements as the excitation of surface plasmons in the typical Kretschmann-ATR configuration requires a 45–50 nm thick metal layer on an optically transparent substrate as the sensing element.[4] Annealed polycrystalline gold beads were used for EIS as these present atomically-flat terraces of ≳ 0.1 μm^2 (Figure 2.1B).

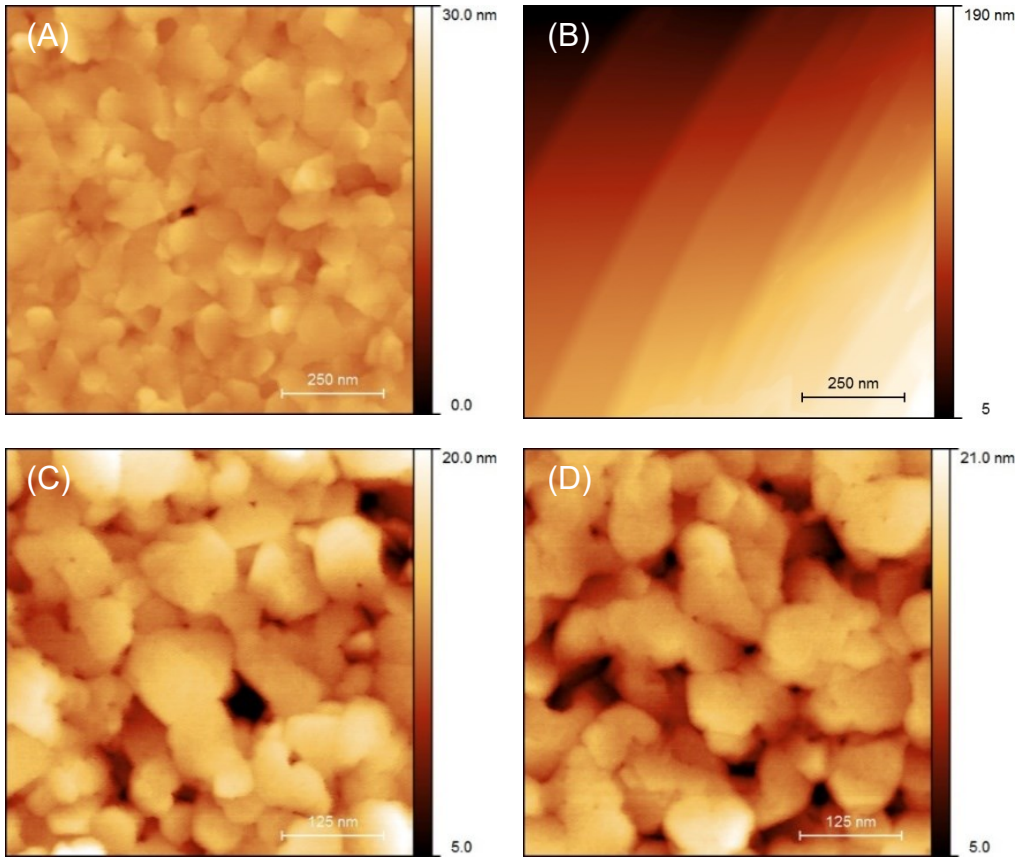

Figure 2.1. AFM height images of (A) thermally-evaporated gold on B270 glass used for ESPR, (B) annealed gold bead electrode used for EIS, (C) FcC_8SAu SAM, and (D) $FcC_{14}SAu$ SAM. Image sizes are (A), (B) 1 μm × 1 μm and (C), (D) 0.5 μm × 0.5 μm.

2.3 Preparation of FcC$_n$SAu SAMs

B270 ultrawhite crown glass slides (n_D^{20} = 1.5229, Esco Products Inc.) of dimensions of 12.5 mm × 22.0 mm × 0.9 mm were cleaned by immersing three times, for 15 min each time, in a freshly-prepared solution of 3:1 v/v concentrated H_2SO_4/30% H_2O_2 (piranha) at room temperature. The glass slides were rinsed copiously with ultrapure water, sonicated thrice in ultrapure water to completely remove traces of sulfuric acid, sonicated once in absolute ethanol, and dried under a stream of nitrogen gas.

Gold thin film substrates were prepared by thermal evaporation using a VE-90 vacuum evaporator (Thermionics Vacuum Products) equipped with a 1 kVA resistive power supply and a turbomolecular pump. A 2 nm layer of titanium (99.99%, Alfa Aesar) was first deposited onto the clean glass at a rate of 0.01 nm s^{-1}, followed by a 50 nm layer of Au (99.99%, Kitco Metals, Inc.), deposited at 0.1 nm s^{-1}. The metal thickness and deposition rate were monitored using a calibrated quartz crystal microbalance. The deposition of metal was initiated once the pressure inside the evaporation chamber reached ~2 × 10^{-7} Torr. The pressure at the end of the gold evaporation was ~2 × 10^{-6} Torr. Radiative heating from the evaporation boats increased the sample temperature to 185 ± 15 °C.

The vacuum was broken with nitrogen once the sample temperature dropped below 35 °C. The gold-coated glass slides were removed from the evaporator chamber and immediately immersed into the Fc$(CH_2)_n$SH solution.

Gold bead electrodes were formed by bonding a 2–3 mm diameter gold granule (99.99%, Kitco Metals, Inc.) to a 0.5 mm diameter gold wire (99.99%, Alfa Aesar) with a butane torch. The surface areas of the gold beads were regularly measured by chronocoulometry using potassium ferricyanide as the redox probe and ranged from 0.20 to 0.28 cm^2. Prior to SAM formation, a gold bead was immersed in dilute aqua regia (3:1:6 $HCl/HNO_3/H_2O$) for ca. 1 min to dissolve away gold from the bead surface and remove surface impurities, rinsed copiously with ultrapure water, sonicated in ultrapure water for 10 min to remove traces of acid, flame-annealed, quenched in ultrapure water, rinsed thoroughly with absolute ethanol, and immersed in the Fc$(CH_2)_n$SH solution. To remove the Fc$(CH_2)_n$SAu SAM from the gold bead surface, the bead was subjected to a 3.5 h photooxidation treatment

in a UV-ozone cleaner (BioForce Nanosciences), followed by 2 h (high RF power setting) in an oxygen-plasma cleaner (Harrick model PDC-32G).

The $Fc(CH_2)_nSAu$ SAMs were formed from 0.2 mM ethanolic solutions of the corresponding thiols for 18 – 24 h at room temperature.[3] The sealed incubation vials were kept in the dark. Prior to use, the $Fc(CH_2)_nSAu$ SAM-modified electrode was removed from the $Fc(CH_2)_nSH$ solution, rinsed copiously with absolute ethanol, followed by ultrapure water, and dried with nitrogen. If water wet the surface of the $Fc(CH_2)_nSAu$ SAM formed on the gold thin film electrode, instead of beading, it was discarded. The $Fc(CH_2)_nSAu$ SAM-modified gold beads were further cleaned by sonication for 3 min in 25 mM aqueous sodium dodecyl sulfate solution at approximately 10 ºC, followed by copious rinsing with ultrapure water, and immersed in the electrolyte. This treatment did not damage the SAM, as verified by cyclic voltammetry.

The surface topographies of the gold thin film and bead electrodes were analyzed by PeakForce tapping mode atomic force microscopy (AFM) in air using a Dimension Icon (Bruker Nano, Santa Barbara, CA) and Scanasyst-air probes (Bruker AFM Probes, Camarillo, CA) with nominal tip radius and spring constant of 2 nm and 0.4 N/m, respectively. Height images were acquired at a scan rate of 0.977 Hz with 512 points per line resolution. Images were processed and analyzed using either Nanoscope Analysis version 1.40 or Gwyddion version 2.47 software. The surface roughness of the gold thin films was evaluated using six substrates taken from three different evaporation lots. The average grain size was determined by manually measuring the widths and lengths of grains in the AFM images of four substrates derived from two different evaporations.

2.4 Electrochemical Surface Plasmon Resonance (EC-SPR)

EC-SPR measurements were carried out in the Kretschmann-type ATR configuration with a computer-controlled SR7000 single-channel instrument (Reichert Inc.). The SR7000 instrument uses stationary optics, a sapphire prism, a divergent fan-shaped beam from a LED source of finite spectral bandwidth (λ = 780 ± 10 nm), and a 3696-pixel linear CCD array to simultaneously measure the reflected light intensity over a range of incident angles (Θ from 48° to 66°). The temperature at the gold/liquid interface is controlled to ±0.015 °C by a Peltier device. The signal-to-noise ratio (peak-to-peak rms) quoted by the manufacturer for the SPR system is 7.3×10^{-5} degree.

A custom-built electrochemical cell fitted with a reference electrode (Ag/AgCl, 3M NaCl electrode inserted in a double-junction chamber, BASi) and counter electrode (Pt wire, 99.99%, Sigma-Aldrich) was mounted onto the FcC_nSAu SAM-modified gold-coated surface of the glass slide (working electrode) whose underside was in optical contact with the prism (Cargille immersion oil Type A liquid, n_D^{23} = 1.5150). The current and pixel position of minimum reflected light intensity were simultaneously recorded as the applied potential was cycled at a rate of 10 mV s^{-1} using an Epsilon potentiostat (BASi) to generate cyclic voltammograms and plots of the resonance angle change as a function of the voltage (Figure 1.28 and 1.29). Each FcC_nSAu SAM was subjected to five consecutive voltammetric cycles to verify the reversibility of the observed changes. The $NaClO_{4(aq)}$ electrolyte was deoxygenated by bubbling with nitrogen for at least 30 min prior to the start of an experiment. Experiments were carried out at 25.0 °C under stationary conditions.

The overlapping anodic peaks were deconvoluted after baseline subtraction using the peak analyzer function in OriginPro 2015 (OriginLab Corporation). The peak position or center, full width at half maximum, and area were free parameters, unless otherwise specified.

The shift in the pixel position of minimum reflected light intensity was converted into a resonance angle change ($\Delta\Theta_{min}$) using the pixel-to-angle relation of 1 pixel = 0.00506° determined by calibration of the SR7000 instrument using binary mixtures of ethylene glycol and water of different refractive index.[5]

SPR (reflectivity versus Θ_{min}) curves were generated based on the Fresnel formalism (WinSpall version 3.02 software, MPI-P) to calculate the oxidation-induced change in the SAM thickness from the corresponding $\Delta\Theta_{min}$. Listed in Table 2.1 are the optical parameters used to generate the curves.

Table 2.1. Fresnel Layer Model Used to Determine the Oxidation-Induced Change in the Effective SAM Thickness

Layer	d / nm	ϵ'	ϵ''
sapphire prism	∞	3.1002[a]	0[a]
titanium	2.0	-3.274[b]	18.308[b]
gold	50	-23.886[b]	1.741[b]
$SC_{14}Fc$	1.95[c]	3.064[d]	0
$SC_{14}Fc^{+}ClO_4^{-}$	2.13[e]		
0.1 M $NaClO_{4(aq)}$	∞	1.7668[f]	0

[a]Value at 780 nm and 24 °C from ref 6. [b]Value at 780 nm from ref 7. [c]SAM thickness from ref 1. [d]ϵ_{SAM} value determined from the SAM capacitance using the parallel capacitor model. [e]Effective SAM thickness calculated to account for the oxidation-induced resonance angle change. [f]Value determined by critical angle refractometry at 780 nm.

2.5 Electrochemical Impedance Spectroscopy (EIS)

EIS measurements on FcC_nSAu SAMs formed on gold bead electrodes were carried out using a conventional three-electrode electrochemical cell and a SP-200 potentiostat (BioLogic Science Instruments) equipped with an impedance analyzer. The electrolyte solution in the electrochemical cell was deoxygenated by bubbling nitrogen for 20 min before starting an experiment. Measurements were carried out under a blanket of nitrogen at 21 ± 1 ^{o}C. Impedance spectra were acquired over a frequency span of six decades, from 100 kHz to 1 Hz, at 64 points per decade using an ac voltage amplitude of 10 mV and an applied voltage of 0 V versus Ag/AgCl. The frequency spectra were transferred to the ZView software (version 3.5b, Scribner Associates, Inc.) for complex nonlinear least-squares (CNLS) fitting to an appropriate electrical equivalent circuit.

Reference

(1) Nerngchamnong, N.; Yuan, L.; Qi, D.-C.; Li, J.; Thompson, D.; Nijhuis, C. A. The Role of van der Waals Forces in the Performance of Molecular Diodes. *Nat. Nanotechnol.* **2013,** *8*, 113-118.

(2) Nerngchamnong, N.; Thompson, D.; Cao, L.; Yuan, L.; Jiang, L.; Roemer, M.; Nijhuis, C. A. Nonideal Electrochemical Behavior of Ferrocenyl–Alkanethiolate SAMs Maps the Microenvironment of the Redox Unit. *J. Phys. Chem. C* **2015,** *119*, 21978-21991.

(3) Love, J. C.; Estroff, L. A.; Kriebel, J. K.; Nuzzo, R. G.; Whitesides, G. M. Self-Assembled Monolayers of Thiolates on Metals as a Form of Nanotechnology. *Chem. Rev.* **2005,** *105*, 1103-1169.

(4) Salamon, Z.; Tollin, G. Surface Plasmon Resonance, Applications. In *Encyclopedia of Spectroscopy and Spectrometry*, John, L., Ed.; Academic Press: Oxford, 1999, pp 2788-2795.

(5) Badia, A.; Chen, C.-I.; Norman, L. L. Calibration of a Fan-Shaped Beam Surface Plasmon Resonance Instrument for Quantitative Adsorbed Thin Film Studies-No Metal Film Thickness or Optical Properties Required. *Sens. Actuators, B* **2013,** *176*, 736-745.

(6) Gray, D. E. Section 6: Optics. In *American Institute of Physics Handbook, 3rd ed.*; McGraw-Hill: New York, 1972, pp 40-41.

(7) Palik, E. D. *Handbook of Optical Constants of Solids*; Academic Press, Inc.: Orlando, 1985.

Chapter 3. Results

In this chapter, the experimental results are presented and summarized into five sections: i) the electrode surface characterization including: topography, average grain size and roughness of the electrode surface characterized by AFM, ii) electrochemical results of FcC_nSAu SAMs measured by cyclic voltammetry and the relative contribution of two populations by the mathematical deconvolutions, iii) the redox-induced resonance angle shift observed by SPR, iv) the electrochemical impedance spectroscopy (EIS) results under non-Faradaic conditions and v) the calculated effective SAM thickness change using the five-layer model. The results presented here have been published.[†]

3.1 Electrode Surface Characterization

The development of scanning probe microscopies provides powerful possibilities to study both the structural organization of the bare electrode and SAMs surfaces, and the assembly process at a molecular level.

Figures 2.1A and S1 show AFM images of the 50 nm-thick gold films deposited on glass slides by thermal evaporation and used for EC-SPR. The surface topography exhibits three distinct height distributions (Figure S2), corresponding to holes (surface coverage of 0.4 ± 0.2 %), valleys (18 ± 2 %), and contiguous grains (81 ± 2%). The average grain size is 95 ± 30 nm (Figure S3). The rms roughness is 1.5 ± 0.4 nm over areas of 1 to 4 μm^2 and the corresponding surface roughness factor (R_q divided by R_a) is 1.02 ± 0.02 (Figure S4). The rms roughness within the grains, estimated to be 0.4 ± 0.2 nm (Figure S5), is comparable to that of ultraflat, template-stripped gold surfaces of ~0.5 nm.[1]

The surface topography of the flame-annealed gold beads consists of atomically-flat terraces with steps of 8 to 15 nm height (Figures 2.1B and S6A). The terraces are typically 100 to 300 nm in width and > 1 μm in length. The rms roughness within the terraces is < 0.2 nm (Figure S6B).

[†]Feng, Y.; Dionne, R. E.; Toader V.; Beaudoin G.; Badia A., Odd–Even Effects in Electroactive Self-Assembled Monolayers Investigated by Electrochemical Surface Plasmon Resonance and Impedance Spectroscopy. *J. Phys. Chem. C.* **2017**, *121*(44), 24626-24640.

The SAMs were prepared using standard procedures.[2-3] AFM images of the FcC_nSAu-modified gold thin films show that the surface of the grains is homogeneously covered with FcC_nS after chemisorption and monolayer formation (Figure 2.1C,D).

3.2 FcC$_n$SAu SAM Electrochemistry

3.2.1 Cyclic Voltammetry

Cyclic voltammograms (CVs) acquired in 0.1 M $NaClO_{4(aq)}$ for the different alkyl chain lengths are presented in Figure 3.1. Due to intermolecular lateral interactions imposed by the high redox load, the FcC$_n$SAu SAMs exhibit non-ideal voltammetric behaviour, i.e., peak broadening, peak asymmetry, peak multiplicity, and anodic-cathodic peak separations > 0 mV. [3-4] The CVs of the shorter-chain FcC$_6$SAu and FcC$_7$SAu SAMs present asymmetric redox peaks centered at 305 mV and 280 mV (vs. Ag/AgCl), respectively. The CVs of the FcC$_8$SAu and FcC$_9$SAu SAMs display principal peaks at $E^{o\prime}$ of 295 mV and 280 mV, respectively, and shoulders at higher potentials. FcC$_n$SAu SAMs with n = 10–16 consistently exhibit two distinct sets of overlapping peaks – a first pair, referred to as "peak 1", centered between 270 and 300 mV and a second pair, "peak 2", between 385 and 420 mV. FcC$_n$SAu SAMs formed on the gold beads also gave dual-peak CVs (Figure S7). The charging current at potentials positive of the redox peaks is higher in the case of the shorter chain FcC$_n$SAu SAMs with n = 6–9, possibly due to a higher degree of ion permeability of the oxidized SAM or greater perturbing effect of $Fc^+ClO_4^-$ ion-pair formation on the SAM structure.[5-6]

The pairwise comparison in Figure 3.1 indicates that the CV of the n_{even} is shifted to more positive potential than that of its n_{odd} homologue. The same behavior is observed for SAMs formed on the gold beads, in which the surface is much smoother (Figure S7). The variations in the anodic peak potential (E_{pa}), cathodic peak potential (E_{pc}), and apparent formal redox potential $E^{o\prime}$ with the number of methylene units n are presented in Figure 3.2A, B. An odd-even oscillation is observed for both sets of peaks. $E^{o\prime}$ for peak 1 of the FcC$_n$SAu SAMs is 21 ± 7 mV or 2.0 ± 0.7 kJ mol^{-1} higher for n_{even} versus n_{odd}, and in the case of peak 2, $E^{o\prime}$ is 13 ± 10 mV or 1.2 ± 1 kJ mol^{-1} higher for n_{even} than n_{odd}. An odd-even alternation in the anodic-cathodic peak separation (ΔE_p) is evident over the entire range of chain lengths for the more cathodic pair of redox peaks – ΔE_p for SAM^{even} > ΔE_p for SAM^{odd} – but is limited to n = 8–13 for the more anodic pair (Figure 3.2C). Nijhuis and coworkers report similar odd-even variations in $E^{o\prime}$ and ΔE_p for FcC$_n$SAu SAMs, where n = 5–13, formed on ultraflat template-

stripped gold.[7-8] Their SAMs exhibit asymmetric redox peaks centered between 275 and 330 mV (vs. Ag/AgCl, 1 M $HClO_{4(aq)}$) and a difference of 25 ± 9 mV (2.4 ± 0.9 kJ mol^{-1}) in $E^{o\prime}$ between n_{even} and n_{odd}.[8] The redox electrochemistry of chains of $n < 5$ is influenced by interactions of the ferrocene with the underlying gold surface and does not exhibit an odd-even effect

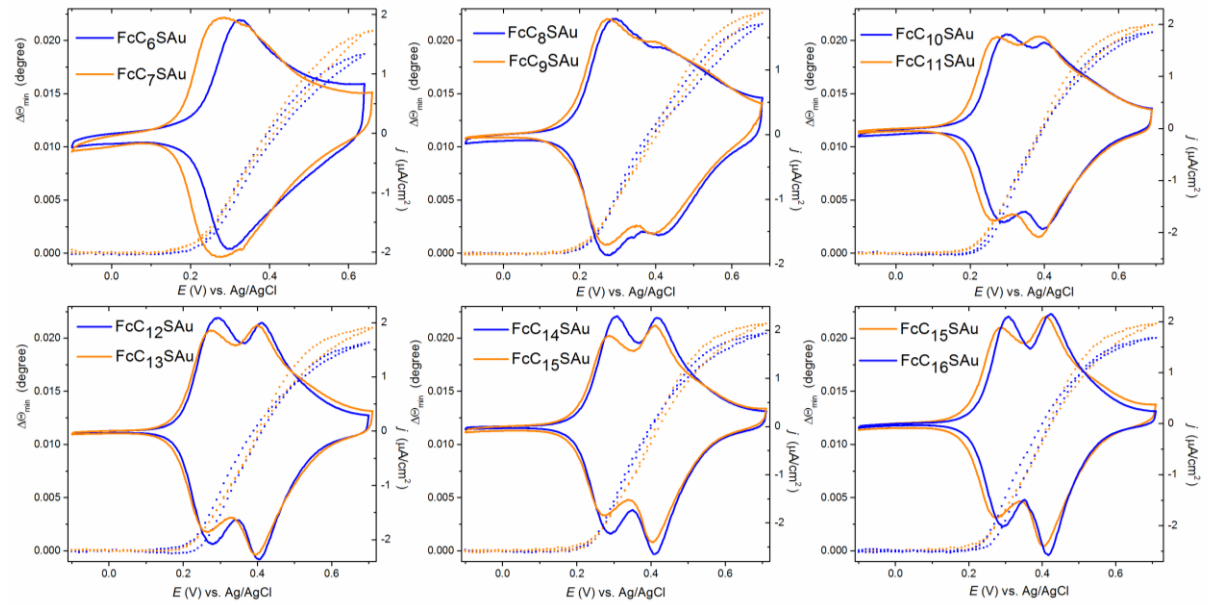

Figure 3.1. Cyclic voltammograms (current density *j*, right-hand axis) and corresponding resonance angle changes ($\Delta\Theta_{min}$, left-hand axis) recorded by ESPR for FcC_nSAu SAMs in 0.1 M $NaClO_{4(aq)}$ (pH = 5.0). Only data from the second of five consecutive oxidation-reduction cycles is shown for clarity. Scan rate of 10 mV s^{-1}.

No odd-even difference in the total ferrocene surface coverage Γ_{Fc}, obtained by integrating the complete anodic segment of the CV, is observed here or on the template-stripped gold (Figure 3.2D). The Γ_{Fc}'s calculated by MD simulations also do not show odd-even variations despite the more favorable molecular packing predicted for SAM^{even}.[8-9] The gold thin film and bead electrodes give identical surface coverages (Figure S8). Γ_{Fc} increases from 3.0×10^{-10} mol cm^{-2} for $n = 6$ to 4.9×10^{-10} mol cm^{-2} for $n = 15$–16. A similar increase is observed on the template-stripped gold (Figure 3.2D).[8] By contrast, MD calculations predict

that Γ_{Fc} increases from 4.6 × 10^{-10} mol cm^{-2} for n = 6 to 5.3 × 10^{-10} mol cm^{-2} for n = 15 (reported in the Supporting Information of ref 9). The theoretical maximum value of Γ_{Fc} is 4.5 × 10^{-10} mol cm^{-2} assuming a hexagonal packing of the ferrocene.[10] The difference between the experimental and theoretical results may result from the different packing structure, physical adsorption of the ferrocene stock on SAMs surfaces and the deviation from the baseline corrections. The areal footprint of the ferrocene (0.34 nm^2) yields a Γ_{Fc} of 4.85 × 10^{-10} mol·cm^{-2}.

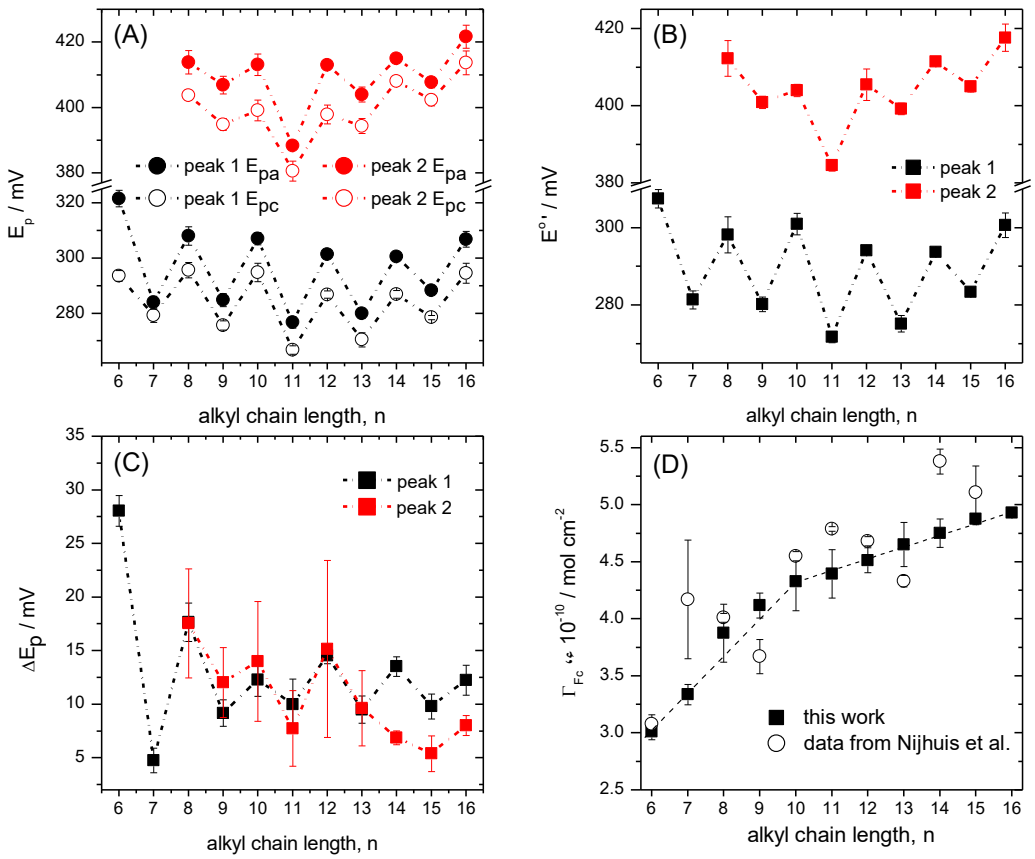

Figure 3.2. Electrochemical data for FcC_nSAu SAMs formed on gold thin film substrates. (A) Anodic and cathodic peak potentials E_{pa} and E_{pc}, (B) apparent formal redox potential $E^{o'}$, (C) anodic-cathodic peak separation ΔE_p, and (D) ferrocene surface coverage Γ_{Fc} as a function of the number of methylenes n in the alkyl chain. Values for peak 2 are not given for n = 6 and 7 in (A)–(C) because their positions are not discernable by eye. Data points and error bars represent the mean and standard deviation of N different FcC_nSAu SAMs: (A)–(C) N = 7–23

and (D) N = 10–15. The dotted lines are guides to the eye. The black open circles in (D) are the Γ_{Fc} values reported in ref 8 for FcC_nSAu SAMs formed on ultraflat, template-stripped gold films.

3.2.2 Peak Deconvolutions

Mathematical deconvolution of the anodic sweeps was used to estimate the relative peak contributions to the total ferrocene concentration. Examples of the peak deconvolutions are presented in Figure 3.3. The Gaussian (peak 1)−Lorentzian (peak 2) combination proposed by Lee *et al.*[11] for binary FcC_nSAu/CH_3C_nSAu SAMs generally gave good fits to the data for FcC_nSAu SAMs of n = 10–16 and should therefore reasonably approximate the relative contributions of the two overlapping peaks to the overall voltammogram. The anodic sweeps of FcC_nSAu SAMs of n = 6–7 could be deconvoluted into two distinct peaks using two Gaussian functions; the Gaussian-Lorentzian combination used for the longer chains gave poor fits. The shoulders on the anodic side of the main peaks of the anodic sweeps of FcC_nSAu SAMs of n = 8–9 (chain lengths for which there is a transition from one-peak CV for shorter chains to a two-peak CV for longer chains) were more difficult to fit. Different mathematical functions were applied and the peak positions deviated significantly from the peak maxima if not fixed. The Gaussian-Lorentzian combination gave the best fits. Nevertheless, the biggest differences between the voltammetric data and cumulative fits were observed for these two chain lengths. The results of the peak deconvolutions are summarized in Figure 3.4. While the anodic peak potentials adhere to a general trend with n (Figure 3.4A), the peak areas (Figure 3.4B), peak surface coverages (Figure 3.4C), and formal widths at half-maximum (Figure 3.4D) deviate from the overall trend at n = 8 or n= 8 and 9, which is probably due to the lower quality of the peak fits, as mentioned above. The values for FcC_8SAu and FcC_9SAu are therefore not considered in the discussion that follows; the focus is on the *overall* trends observed with chain length.

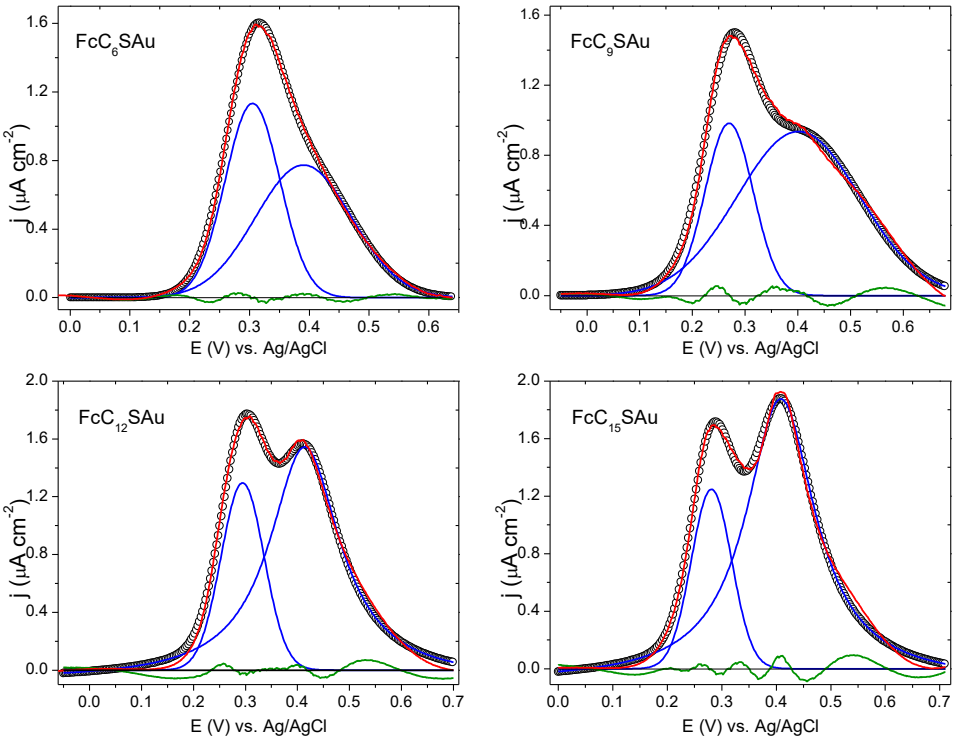

Figure 3.3. Examples of the anodic peak deconvolution. Blue curves are the individual Gaussian and Lorentzian peaks and red curves are the cumulative fits. The green curves are the fitting residuals. The anodic peaks were baseline corrected with Boltzmann function before mathematical deconvolution. Functions used for the peak deconvolutions: FcC_6SAu Gaussian-Gaussian, FcC_9SAu Gaussian-Gaussian, $FcC_{12}SAu$ Gaussian-Lorentzian, and $FcC_{15}SAu$ Gaussian-Lorentzian.

As with $E^{o\prime}$, the individual anodic peak positions (E_{pa}) for SAM^{even} and SAM^{odd} remain quasi-constant as a function of n (Figure 3.4A). E_{pa} of peak 1 is 303 ± 6 mV for SAM^{even} and 275 ± 7 mV for SAM^{odd}. E_{pa} of peak 2 is 422 ± 16 mV for SAM^{even} and 396 ± 19 mV for SAM^{odd}. The relative peak areas are almost constant with n – the relative areas of peaks 1 and 2 are 29 ± 6 % and 71 ± 6 %, respectively (Figure 3.4B). Odd-even fluctuations are evident. Figure 3.4C presents the individual ferrocene surface coverages of the two anodic peaks as a function of n calculated from the relative peak contributions (Figure 3.4B) to the total ferrocene concentration (Figure 3.1A). Γ_{Fc} associated with peak 1 increases from 0.98×10^{-10}

mol cm^{-2} for n = 6 to 1.4 × 10^{-10} mol cm^{-2} for n = 16, with an odd-even oscillation of 0.28 (±0.15) × 10^{-10} mol cm^{-2} between n = 7 and n = 14. There is a larger increase in the Γ_{Fc} of peak 2 with chain length, from 2.0 × 10^{-10} mol cm^{-2} for n = 6 to 3.6 × 10^{-10} mol cm^{-2} for n = 13–16. Odd-even fluctuations are present but less apparent because they are superimposed on an increasing Γ_{Fc}. Similar trends in the electrochemical parameters have been observed for $n \geq 5$ on ultraflat template-stripped gold.[8]

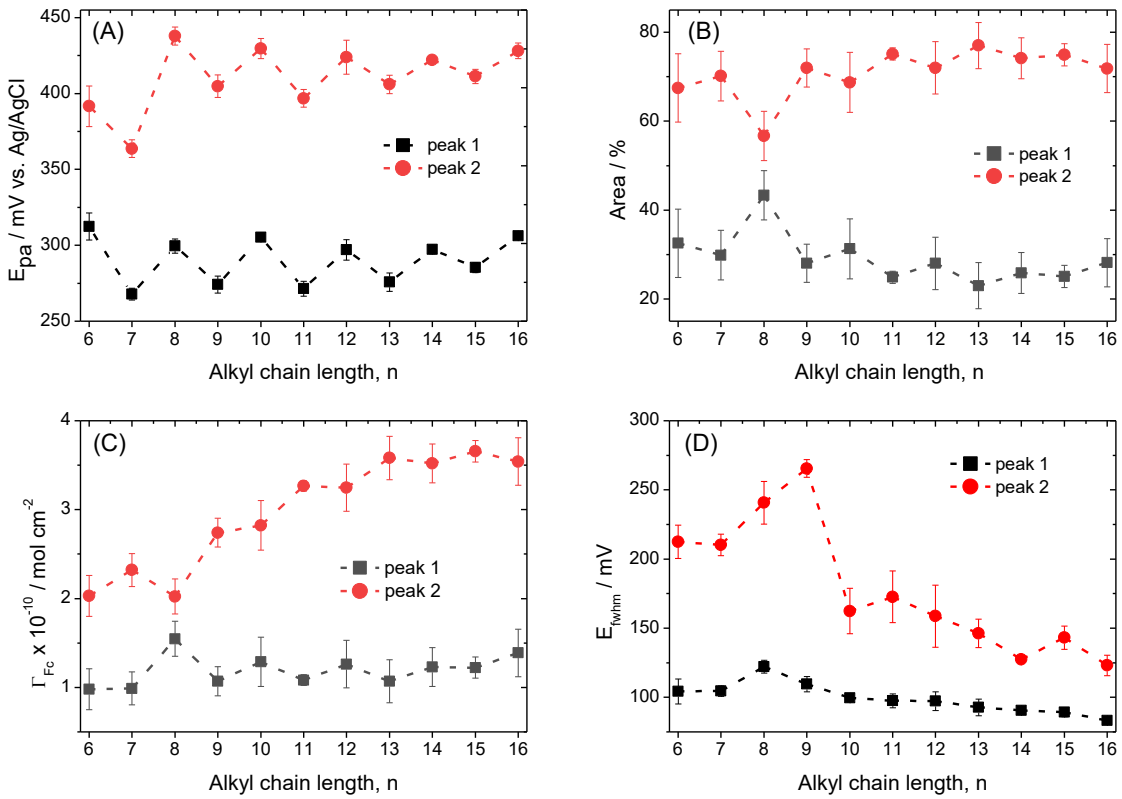

Figure 3.4. Anodic peak deconvolution results. (A) Peak potential E_{pa}, (B) percent area peak area, (C) ferrocene surface coverage Γ_{Fc}, and (D) full width at half maximum E_{fwhm} of the individual peaks as a function of n. N = 10 different voltammetric sweeps were deconvoluted for each n. The data points and error bars represent the mean and standard deviation. The dotted lines are guides to the eye.

The apparent formal potential of surface-confined redox species, ferrocene-terminated SAMs included, has been found to vary with the surface coverage.[10-15] How does one then explain that E_{pa} and $E^{o\prime}$ of SAM^{even} and SAM^{odd} remain remarkably constant as a function of the alkyl chain length even though Γ_{Fc} increases by more than 60% from $n = 6$ to $n = 16$?

The effect of non-ideal interactions on the peak potential E_p of surface-attached redox centers is given by equation 28:

$$E_p = E^{o\prime} - RT\Gamma_T(r_O - r_R) / 2nF \quad (28)$$

where $E^{o\prime}$ is the formal potential of the surface-confined redox moieties, Γ_T is the total surface concentration of the redox species, and r_O and r_R are the non-ideal interaction parameters.[13] This treatment assumes that the interaction parameters are independent of the applied potential. The term r_O (= $r_{OO} - r_{OR}$) describes the net perturbing influence experienced by the attached oxidized form O due to the presence of another attached O (r_{OO}) or reduced moiety R (r_{OR}), while r_R (= $r_{RR} - r_{RO}$) describes the analogous perturbation of a given R. In the case of the SAM-bound ferrocene, the electrogenerated ferrocenium will experience a greater perturbation from a neighboring ferrocenium (due to Coulomb repulsion) than from a neutral ferrocene (i.e., $r_{OO} > r_{OR}$ or r_{RO}). Since the surface coverages of both peaks vary with chain length (albeit to different extents), equation 28 suggests that the degree of the lateral interactions, given by $r_O - r_R$, must vary with n for the peak potentials to remain constant.

The Gaussian and Lorentzian functions used for the mathematical peak deconvolutions are not model specific. If we however assume that the E_{fwhm} values (Figure 3.4D) thus obtained reasonably describe the individual peak shapes, these can be used to estimate the intermolecular interaction parameters of the two ferrocene populations using expressions derived by Laviron based on the Frumkin isotherm:

$$nE_{fwhm} = (2RT/F)\left|ln\frac{1+\beta}{1-\beta} - \nu G\theta_T\beta\right| \quad (29)$$

with

$$\beta = \sqrt{2 - \nu G\theta_T}/\sqrt{4 - \nu G\theta_T} \quad (30)$$

where n is the number of electrons transferred per redox moiety and $\nu G\theta_T$ is the interaction parameter.[15] G is equal to $a_O + a_R - 2a_{OR}$, where a_O, a_R, and a_{OR} are the constants of interaction, analogous to the aforementioned interaction parameters r_O and r_R (equation 28).[13]

If the surface-confined redox centers do not interact with each other, E_{fwhm} is 90.6 mV, $\nu G\theta_\Gamma$ is 0, and the peak shape and properties obey the Langmuir isotherm. Lateral interactions cause a deviation from this ideal behavior. When $\nu G\theta_\Gamma < 0$, $E_{fwhm} > 90.6$ mV and repulsion forces dominate among the redox centers. For $\nu G\theta_\Gamma > 0$, $E_{fwhm} < 90.6$ mV and attraction forces predominate.[15]

The Laviron formalism is convenient because it relates the half-peak width to the interaction parameter. It was however formulated to describe a single symmetrical peak (i.e., single redox population).[15] We applied Laviron theory to generate $j - E$ curves to match the individual anodic peaks (as per ref 16 for example). The sum of the two calculated curves did not however fit the overall dual-peak voltammogram. The values of $\nu G\theta_\Gamma$ were therefore determined using the average E_{fwhm} values obtained from the Gaussian-Lorentzian or Gaussian-Gaussian peak deconvolutions and the linear relationship between E_{fwhm} and $\nu G\theta_\Gamma$ for $-3 \leq \nu G\theta_\Gamma \leq 1$ (Figure 3.5).[15] E_{fwhm} of peak 1, fit with a Gaussian function, is close to the ideal value and varies with n: E_{fwhm} decreases from 105 mV for $n = 6$ to 85 mV for $n = 16$ (Figure 3.4D). The $\nu G\theta_\Gamma$ values vary from -0.33 to 0.14 (if $n = 8$ is excluded). The interactions between the SAM-bound ferroceniums go from being repulsive for $n = 6 – 12$ to non-existent (near-ideal behavior) or weakly attractive for the longer chain lengths ($n \geq 13$). By contrast, E_{fwhm} of peak 2, fit using either a Gaussian or Lorentzian distribution, is significantly greater than 90.6 mV and exhibits a larger variation with n than peak 1: E_{fwhm} decreases from 210 mV for $n = 6$ to 125 mV for $n = 16$ (Figure 3.4D). The concomitant $\nu G\theta_\Gamma$ values range from -2.2 to -0.58 (excluding $n = 8$ and 9), implying that repulsive lateral interactions predominate and that the extent of the intermolecular interactions in this ferrocene population is greater than that of the peak 1 population. Moreover, as the peaks become narrower with increasing chain length, the extent of overlap between them decreases, and hence, the observed progression from one asymmetric peak to a predominant peak with shoulder to two distinct peaks.

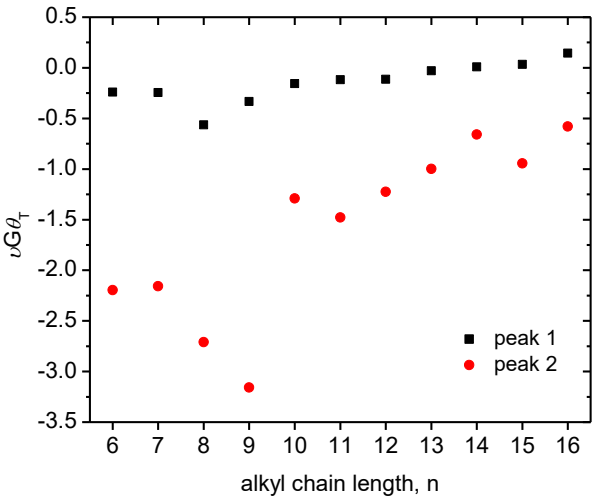

Figure 3.5. Interaction parameter $\nu G\theta_{\mathrm{T}}$ as a function of the alkyl chain length n.

3.3 Redox-Induced Resonance Angle Change

In situ EC-SPR was used to track the redox-induced structural transformations in real time. Figure 3.1 shows the resonance angle change $\Delta\Theta_{min}$ as a function of the applied potential *E*. There is no change in the resonance angle prior to the generation of a Faradaic current, indicating that the measured resonance angle shifts are not due to potential-induced changes in the optical constants of the gold, as the presence of the SAM dielectric suppresses the potential dependence of the SPR response.[17] Furthermore, neither ferrocene nor ferrocenium absorbs at the wavelength (780 nm) used to excite the surface plasmons, and therefore, they do not contribute to the observed resonance angle change.[18] Θ_{min} directly tracks the conversion of the SAM-bound ferrocene to ferrocenium, as previously shown.[19-20] The $\Delta\Theta_{min}$–*E* curves exhibit a sigmoidal form. Θ_{min} increases upon oxidation of the ferrocene to ferrocenium (Figure 1.28A), reaches a limiting value after all of the ferrocene has been oxidized to ferrocenium, and returns to its initial value when the ferrocenium is reduced back to ferrocene. There are no inflections observed in the $\Delta\Theta_{min}$–*E* curves in the potential region (valley) between the two redox peaks. The $\Delta\Theta_{min}$–*E* curves are reproducible over at least five successive oxidation–reduction cycles run between -100 and 650–700 mV (versus Ag/AgCl) at a potential scan rate of 10 mV s^{-1} (Figure 1.28B), suggesting that any SAM structural changes accompanying a ferrocene oxidation/ferrocenium reduction cycle are reversible. Figure 3.1 reveals that at the anodic potential limit, where all the SAM-bound ferrocene has been oxidized, $\Delta\Theta_{min}$ of n_{odd} is larger that of its n_{even} homologue.

We carried out EC-SPR measurements on 136 individual FcC_nSAu SAMs (i.e., 10–19 SAMs per *n*). Figure 3.6 summarizes the resonance angle changes measured at the most oxidizing potential ($\Delta\Theta_{min}^{ox}$) as a function of the alkyl chain length. $\Delta\Theta_{min}^{ox}$ increases from 0.0188° for $n = 6$ to 0.0219° for $n = 9$ and varies between 0.0200° and 0.0219° for $n \geq 9$. A systematic odd-even fluctuation is observed between $n = 9$ and $n = 16$. $\Delta\Theta_{min}^{ox}$ is 0.0011 ± 0.0005° higher for n_{odd} than n_{even}. This difference is small but experimentally significant (see Supporting Information for statistical analysis).

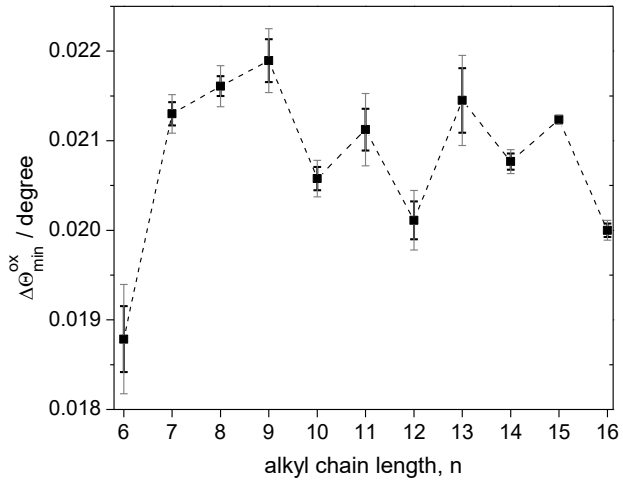

Figure 3.6. Resonance angle change recorded at the most anodic potential $\Delta\Theta_{\mathrm{min}}^{\mathrm{ox}}$ versus the number of methylenes *n* in the alkyl chain of the FcC_nSAu SAMs. Each data point is the mean of N = 10–19 different FcC_nSAu SAMs. Error bars represent the standard deviations (grey) and 95% confidence intervals (black) of the mean $\Delta\Theta_{\mathrm{min}}^{\mathrm{ox}}$ values. The dotted line is a guide to the eye.

3.4 EIS of the FcC_nSAu SAMs

To rationalize the odd-even variation of the resonance angle shift induced by the oxidation of the SAM-bound ferrocene, electrochemical impedance spectroscopy under non-Faradaic conditions was used to probe the ionic insulating and dielectric properties of the FcC_nSAu SAMs. Bode and complex plane plots were used to visualize the raw data and evaluate the quality of the data fits over the entire range of frequencies probed.[21] Representative impedance spectra measured at 0 V (vs. Ag/AgCl) in 0.1 M $NaClO_{4(aq)}$ on FcC_nSAu SAMs of n = 7–16 formed on gold bead electrodes are shown in Figure 3.7 for selected chain lengths. At 0 V, the FcC_nSAu SAMs are in the reduced (neutral) state and there is no electron transfer reaction. There is little variation of the impedance magnitude $|Z|$ with chain length (Figure 3.7A). At frequencies between 1 Hz and 1 kHz (i.e., linear region), the slope of the Bode magnitude plot ($|Z|$ versus log frequency f) is -0.98 for each n, typical of a capacitor-like system.[22] The measured impedance is dominated by the solution resistance at high frequencies, and $|Z|$ becomes independent of frequency at $f \geq 10$ kHz. The value of $|Z|$ of 10^5 Ω cm^2 at 1 Hz for the FcC_nSAu SAMs is the same as that reported for insulating CH_3C_nSAu SAMs.[23]

The corresponding complex plane plots (imaginary part of the impedance Z'' versus real part Z', Figure 3.7B) exhibit nearly vertical lines that are typical of pure capacitor behavior over the frequency domain investigated of 1 Hz to 100 kHz.[22] These results imply that the transport of ions into the SAM is not occurring over the time scale of the measurement, and that under the experimental conditions used, the FcC_nSAu SAMs are ionic insulators.

According to Boubour and Lennox, the impedance phase angle is a more reliable indicator of the defectiveness of a SAM and its ability to act as an ionic insulator.[23] When an AC potential is applied to an electrical circuit consisting of a resistance in series with a capacitance, the phase angle (φ) gives the lag between the sinusoidal voltage and current signals at a given frequency. The phase angle indicates the relative importance of the resistive (φ = 0°) and capacitive (φ = 90°) pathways within the circuit.[22] Boubour and Lennox determined that ω-functionalized alkanethiolate SAMs are well described by the Helmholtz ideal capacitor model, with the gold surface acting as one capacitor plate and the physisorbed

ions at the SAM/electrolyte interface acting as the other plate, when the phase angle at frequencies < ~50 Hz (frequency domain characteristic of ion diffusion) is ≥ 88°.[48] Defect-laden SAMs behave like a capacitor contaminated by a resistive component associated with current leakage due to ion and water penetration at defect sites, resulting in phase angles < ~87°.[24] Phase angles of 88°–89° were obtained at frequencies between 1 and 100 Hz (Figure 3.7C), indicating that the FcC_nSAu SAMs are impermeable to ions in their reduced/neutral state.

The equivalent circuit that best fits the impedance spectra of the FcC_nSAu SAMs consists of a solution resistance (R_s) in series with a constant phase element (CPE) (Figure 3.7A inset). The CNLS fitting parameters are summarized in Table S1. The CPE is a power law-dependent interfacial capacity ($Z_{CPE} = (Q(j\omega)^{\alpha})^{-1}$) that accounts for deviations from ideal capacitive behavior.[21] The magnitude of the CPE parameter is only equivalent to the film capacitance if the CPE exponent (α) is equal to 1. The CPE exponents are very close to 1 (α = 0.98-0.99) for the FcC_nSAu SAMs prepared here so that the CPE magnitude is a good approximation of the SAM capacitance. The values of the monolayer capacitance per unit area (C_{SAM}) thus obtained decrease with chain length, from 2.02 ± 0.14 μF cm^{-2} for n = 7 to 1.26 ± 0.06 μF cm^{-2} for n = 16, as the SAM becomes progressively thicker. The value of 1.48 ± 0.07 μF cm^{-2} for the $FcC_{11}SAu$ SAM falls within the range of capacitance values (1.45 to 1.56 μF cm^{-2}) obtained by Cruañes *et al*. in 1 M $NaClO_{4(aq)}$ at 0 V (vs. Ag/AgCl) for two $FcC_{11}SAu$ SAMs subjected to pressures of 0 to 5 kbar.[25] For a given n, the FcC_nSAu SAM capacitance is higher than that of its more densely packed CH_3C_nSAu SAM analogue.[23]

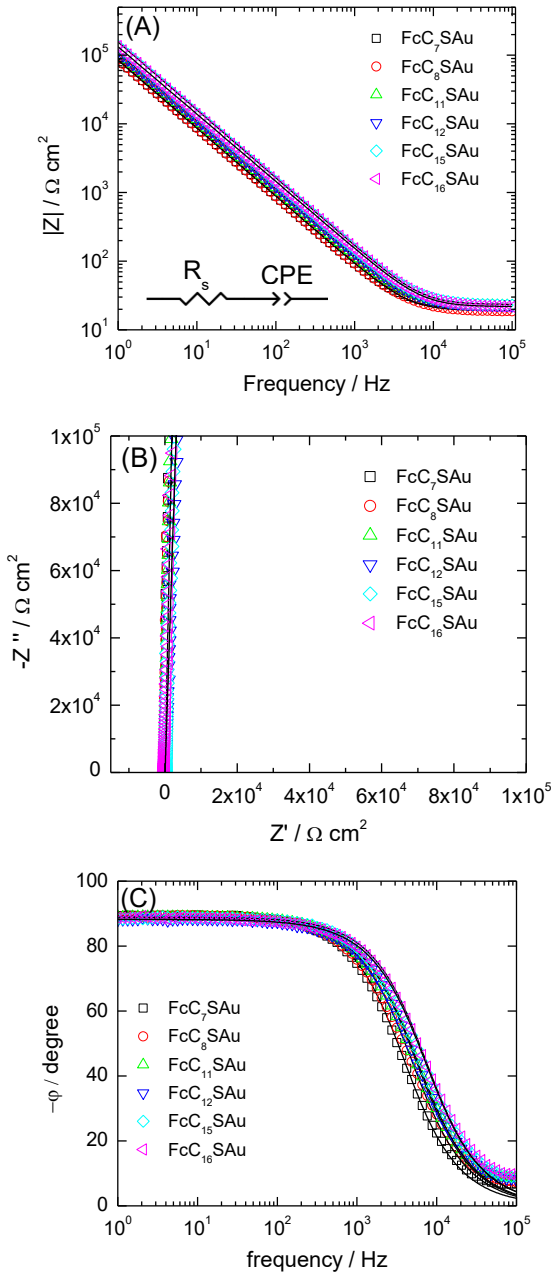

Figure 3.7. Electrochemical impedance spectroscopy (EIS) data for selected chain lengths. (A) Bode plot – impedance magnitude $|Z|$ vs. frequency. (B) Complex plane plot – imaginary part of the impedance Z'' vs. the real part Z'. (C) Bode phase plot – phase angle φ vs. frequency. Impedance spectra were acquired at 0.0 V versus Ag/AgCl in 0.1 M $NaClO_{4(aq)}$ (pH = 5.0). Symbols are the experimental data and solid lines are the result of CNLS fits to the data using the equivalent circuit model shown in inset in (A) which consists of a solution resistance R_s in series with a constant phase element CPE.

The reciprocal of the monolayer capacitance C_{SAM}^{-1} is plotted as a function of n in Figure 3.8A. C_{SAM}^{-1} increases linearly as a function of n, with odd-even alternations observed for $n \geq 10$. $C_{SAM^{even}} \gtrapprox C_{SAM^{odd}}$ (Table S1). The Helmholtz theory models the electrical double layer as a parallel plate capacitor for which the reciprocal of the capacitance per unit area C^{-1} is proportional to the thickness (d) of the dielectric layer that separates the two conducting plates:

$$C^{-1} = d/\epsilon\epsilon_0 \tag{31}$$

where ϵ is the relative dielectric constant or relative dielectric permittivity of the intervening medium and ϵ_0 is the permittivity of free space (8.85419×10^{-12} F m^{-1}).[22] The values of the SAM dielectric constant (ϵ_{SAM}) calculated according to equation 31 from the capacitance values and the computed FcC_nSAu SAM thicknesses given in the supplementary information of ref 7 are shown in Figure 3.8B. ϵ_{SAM} spans 2.86–3.16 and remains nearly constant with chain length. ϵ_{SAM} of n_{even} is higher than n_{odd} for n = 8–16 (see Supporting Information for statistical analysis). The dielectric constants for structurally-related molecules are: FcC_6SH (ϵ = 2.39, Figure S9), ethyl ferrocene (ϵ = 2.56),[26] and butyl ferrocene (ϵ = 2.49),[27] where ϵ is the square of the refractive index n measured by refractometry at 589.3 nm since ferrocene does not absorb at this wavelength[18].

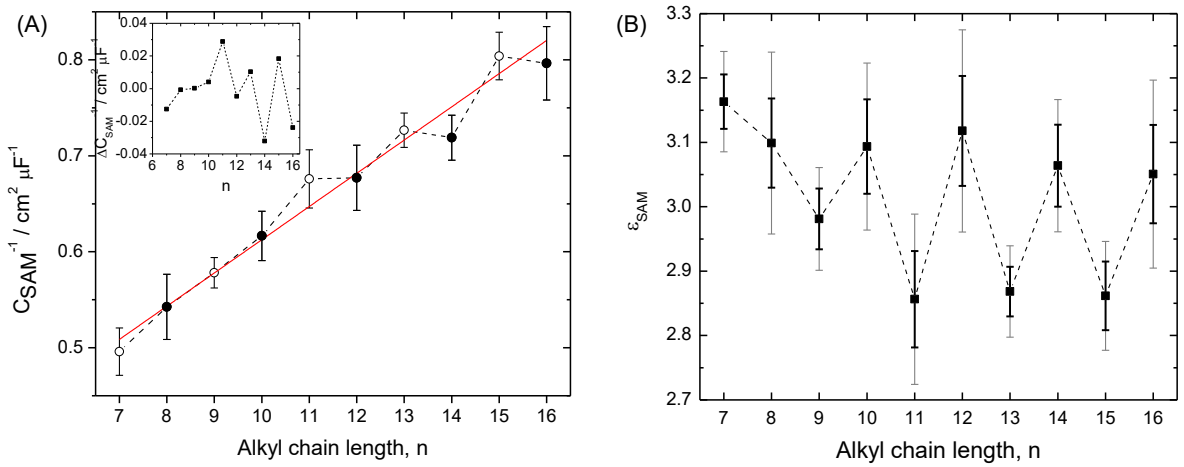

Figure 3.8. (A) Plot of the reciprocal of the FcC$_n$SAu SAM capacitance C_{SAM}^{-1} as a function of n. The solid line represents the linear regression analysis to *all* of the data. Error bars represent the standard deviations of the mean values of N = 10–16 independent measurements per n. Inset shows the difference (ΔC_{SAM}^{-1}) between C_{SAM}^{-1} obtained experimentally and C_{SAM}^{-1} calculated based on the regression line. (B) Dielectric constant ϵ_{SAM} calculated from the SAM capacitance using equation 31 and the computed SAM thicknesses reported in ref 6. The thickness of the n = 16 SAM was extrapolated from the reported values. Error bars represent the standard deviations (grey) and 95% confidence intervals (black) of the mean values. Dashed lines are guides to the eye.

3.5 SAM Thickness Change

The change in the effective SAM thickness caused by the oxidation of the ferrocene to ferrocenium (Δd^{ox}) was determined from the corresponding mean values of $\Delta\Theta_{min}^{ox}$ (Figure 3.9). Reflectivity–Θ curves were generated using the five-layer model given in (Table 1): 1-prism, 2-titanium, 3-gold, 4-reduced or oxidized SAM, and 5-electrolyte solution, where ϵ' and ϵ'' are the real and imaginary components of the wavelength- and temperature-dependent complex dielectric constant. The ϵ_{SAM} values calculated from the SAM capacitances (equation 31) were used for ϵ'. ϵ'' was set to 0 since neither ferrocene nor ferrocenium absorbs at the wavelength used to excite the surface plasmons, as already mentioned. It was assumed that that there is no water (solvent) penetration into the FcC_nSAu SAM upon ferrocene oxidation and ClO_4^- anion association and that the complex dielectric constants of the reduced and oxidized forms are the same.[28-31] The perchlorate ions paired with the SAM-bound ferrocenium termini were considered to be part of the electrolyte solution.[18] A chain length-independent Δd^{ox} of 0.19 ± 0.01 nm was thus obtained (see Discussion).

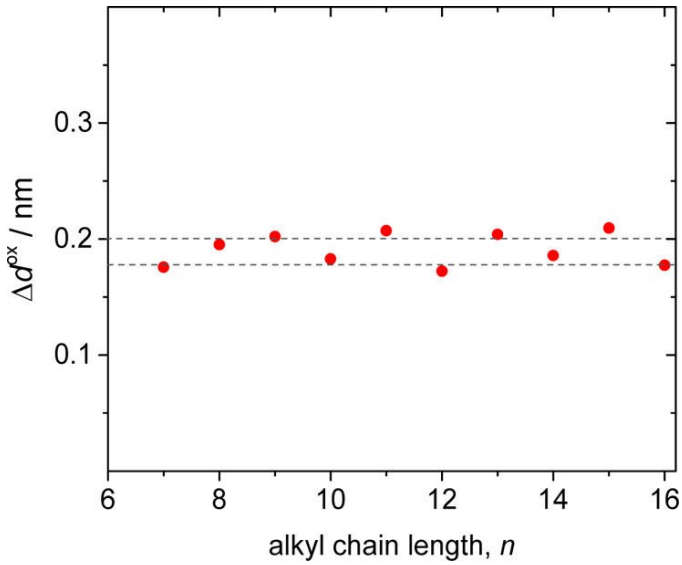

Figure 3.9. Oxidation-induced FcC_nSAu SAM thickness change Δd^{ox} calculated using the mean values of ϵ_{SAM} determined by EIS and $\Delta\Theta_{min}^{ox}$ determined by ESPR. Dashed lines indicate the upper and lower limits of the standard deviation of the average of *all* the data.

Reference

(1) Weiss, E. A.; Kaufman, G. K.; Kriebel, J. K.; Li, Z.; Schalek, R.; Whitesides, G. M. Si/SiO2-Templated Formation of Ultraflat Metal Surfaces on Glass, Polymer, and Solder Supports: Their Use as Substrates for Self-Assembled Monolayers. *Langmuir* **2007,** *23*, 9686-9694.

(2) Love, J. C.; Estroff, L. A.; Kriebel, J. K.; Nuzzo, R. G.; Whitesides, G. M. Self-Assembled Monolayers of Thiolates on Metals as a Form of Nanotechnology. *Chem. Rev.* **2005,** *105*, 1103-1169.

(3) Finklea, H. O. Electrochemistry of Organized Monolayers of Thiols and Related Molecules on Electrodes. In *Electroanalytical Chemistry: A Series of Advances*, Bard, A. J.; Rubinstein, I., Eds.; Marcel Dekker: New York, 1996; Vol. 19, pp 109–335.

(4) Calvente, J. J.; Andreu, R. Intermolecular Interactions in Electroactive Thiol Monolayers Probed by Linear Scan Voltammetry. *Curr. Opin. Electrochem.* **2017,** *1*, 22-26, and references therein.

(5) Collard, D. M.; Fox, M. A. Use of Electroactive Thiols to Study the Formation and Exchange of Alkanethiol Monolayers on Gold. *Langmuir* **1991,** *7*, 1192–1197.

(6) Thompson, D.; Nijhuis, C. A. Even the Odd Numbers Help: Failure Modes of SAM-Based Tunnel Junctions Probed via Odd-Even Effects Revealed in Synchrotrons and Supercomputers. *Acc. Chem. Res.* **2016,** *49*, 2061-2069.

(7) Nerngchamnong, N.; Yuan, L.; Qi, D.-C.; Li, J.; Thompson, D.; Nijhuis, C. A. The Role of van der Waals Forces in the Performance of Molecular Diodes. *Nat. Nanotechnol.* **2013,** *8*, 113-118.

(8) Nerngchamnong, N.; Thompson, D.; Cao, L.; Yuan, L.; Jiang, L.; Roemer, M.; Nijhuis, C. A. Nonideal Electrochemical Behavior of Ferrocenyl–Alkanethiolate SAMs Maps the Microenvironment of the Redox Unit. *J. Phys. Chem. C* **2015,** *119*, 21978-21991.

(9) Yuan, L.; Thompson, D.; Cao, L.; Nerngchangnong, N.; Nijhuis, C. A. One Carbon Matters: The Origin and Reversal of Odd–Even Effects in Molecular Diodes with Self-Assembled Monolayers of Ferrocenyl-Alkanethiolates. *J. Phys. Chem. C* **2015,** *119*, 17910-17919.

(10) Chidsey, C. E. D.; Bertozzi, C. R.; Putvinski, T. M.; Mujsce, A. M. Coadsorption of Ferrocene-Terminated and Unsubstituted Alkanethiols on Gold: Electroactive Self-Assembled Monolayers. *J. Am. Chem. Soc.* **1990,** *112*, 4301–4306.

(11) Lee, L. Y. S.; Sutherland, T. C.; Rucareanu, S.; Lennox, R. B. Ferrocenylalkythiolates as a Probe of Heterogeneity in Binary Self-Assembled Monolayers on Gold. *Langmuir* **2006,** *22*, 4438–4444.

(12) Dionne, E. R.; Toader, V.; Badia, A. Microcantilevers Bend to the Pressure of Clustered Redox Centers. *Langmuir* **2014,** *30*, 742-752.

(13) Brown, A. P.; Anson, F. C. Cyclic and Differential Pulse Voltammetric Behavior of Reactants Confined to the Electrode Surface. *Anal. Chem.* **1977,** *49*, 1589-1595.

(14) Creager, S. E.; Rowe, G. K. Solvent and Double-Layer Effects on Redox Reactions in Self-Assembled Monolayers of Ferrocenyl-Alkanethiolates on Gold. *J. Electroanal. Chem.* **1997,** *420*, 291-299.

(15) Laviron, E. Surface Linear Sweep Voltammetry: Equation of the Peaks for a Reversible Reaction When Interactions Between Adsorbed Molecules are Taken into Account. *J. Electroanal. Chem.* **1974,** *52*, 395-402.

(16) Tian, H.; Dai, Y.; Shao, H.; Yu, H.-Z. Modulated Intermolecular Interactions in Ferrocenylalkanethiolate Self-Assembled Monolayers on Gold. *J. Phys. Chem. C* **2012,** *117*, 1006-1012.

(17) Heaton, R. J.; Peterson, A. W.; Georgiadis, R. M. Electrostatic Surface Plasmon Resonance: Direct Eelectric Field-Induced Hybridization and Denaturation in Monolayer Nucleic Acid Films and Label-Free Discrimination of Base Mismatches. *Proc. Natl. Acad. Sci. U.S.A.* **2001,** *98*, 3701-3704.

(18) Yao, X.; Wang, J.; Zhou, F.; Wang, J.; Tao, N. Quantification of Redox-Induced Thickness Changes of 11-Ferrocenylundecanethiol Self-Assembled Monolayers by Electrochemical Surface Plasmon Resonance. *J. Phys. Chem. B* **2004,** *108*, 7206–7212.

(19) Badia, A.; Chen, C.-I.; Norman, L. L. Calibration of a Fan-Shaped Beam Surface Plasmon Resonance Instrument for Quantitative Adsorbed Thin Film Studies-No Metal Film Thickness or Optical Properties Required. *Sens. Actuators, B* **2013,** *176*, 736-745.

(20) Norman, L. L.; Badia, A. Electrochemical Surface Plasmon Resonance Investigation of Dodecyl Sulfate Adsorption to Electroactive Self-Assembled Monolayers via Ion-Pairing Interactions. *Langmuir* **2007,** *23*, 10198–10208.

(21) Lasia, A. *Electrochemical Impedance Spectroscopy and its Applications*; Springer: New York, USA, 2014.

(22) Bard, A. J.; Faulkner, L. R. *Electrochemical Methods Fundamentals and Applications*; 2nd ed.; J. Wiley & Sons: New York, 2001.

(23) Boubour, E.; Lennox, R. B. Insulating Properties of Self-Assembled Monolayers Monitored by Impedance Spectroscopy. *Langmuir* **2000,** *16*, 4222-4228.

(24) Boubour, E.; Lennox, R. B. Stability of ω-Functionalized Self-Assembled Monolayers as a Function of Applied Potential. *Langmuir* **2000,** *16*, 7464-7470.

(25) Cruañes, M. T.; Drickamer, H. G.; Faulkner, L. R. Characterization of Charge Transfer Processes in Self-Assembled Monolayers by High-Pressure Electrochemical Techniques. *Langmuir* **1995,** *11*, 4089–4097.

(26) www.sigmaaldrich.com/catalog/product/aldrich/484350 (accessed 19/06/2017).

(27) www.sigmaaldrich.com/catalog/product/aldrich/325236 (accessed 19/06/2017).

(28) Ohtsuka, T.; Sato, K.; Uosaki, K. Dynamic Ellipsometry of a Self-Assembled Monolayer of a Ferrocenylalkanethiol During Oxidation-Reduction Cycles. *Langmuir* **1994,** *10*, 3658–3662.

(29) Abrantes, L. M.; Kalaji, M.; Viana, A. S. In Situ Ellipsometric Study of Redox Induced Orientation of a Short Chained Ferrocenylalkylthiol Monolayer Self-Assembled on Gold. *Russ. J. Electrochem.* **2002,** *38*, 39–43.

(30) Viana, A. S.; Kalaji, M.; Abrantes, L. M. Electrochemical Quartz Crystal Microbalance Study of Self-Assembled Monolayers and Multilayers of Ferrocenylthiol Derivatives on Gold. *Langmuir* **2003,** *19*, 9542-9544.

(31) Shimazu, K.; Yagi, I.; Sato, Y.; Uosaki, K. Electrochemical Quartz Crystal Micro-balance Studies of Self-Assembled Monolayers of 11-Ferrocenyl-1-Undecanethiol: Structure-Dependent Ion-Pairing and Solvent Uptake. *J. Electroanal. Chem.* **1994,** *372*, 117–124.

Chapter 4. Discussion

The studies reported herein were initiated to examine the effect of an odd versus even number of methylenes on the redox-induced changes in the FcC_nSAu SAM structure. The apparent redox potential indicated an odd-even effect on the thermodynamics of the interfacial redox reaction.[1-2] By probing the oxidation-induced SAM film thickness change, we sought to establish whether the different orientation/steric constraints of the ferrocene units and strength of the van der Waals interactions in SAM^{even} versus SAM^{odd} affect the ability of the pairing anion to induce molecular reorientations within the SAM. A discussion of the findings and their implications follows and this part of work could be found in the paper shown at the end of the page. [†]

4.1 Surface Microstructure

The surface topography of the thermally-evaporated, gold thin films employed for EC-SPR was characterized in terms of roughness, grain size, and grain coverage. In addition to the latter, bearing volume, a parameter associated with the grain size and boundary widths, has been used in some cases to further characterize the surface defects.[3-4] This characteristic is difficult to quantify for our gold thin films as the grain boundaries are not well defined (Figures 2.1A and S1). The as-deposited gold is rougher on the micrometer length scale (rms roughness of ~1.5 nm over 1–4 μm^2) than the ultrasmooth template-stripped gold (rms roughnesses of 0.4–0.5 over 1–10 μm^2 and grain sizes of 185–250 nm)[1, 3-4] used to demonstrate odd-even effects in the electrical properties of FcC_nSAu SAM-based tunnel junctions,[1, 5] apparent redox potential of FcC_nSAu SAMs,[1-2] and wetting properties of CH_3C_nSAu SAMs.[3] Although the electrochemical signature of our FcC_nSAu SAMs is different from those formed on ultraflat gold films,[2] we observe odd-even alternations of the electrochemical parameters (redox peak potentials, apparent formal potential, and anodic-cathodic peak separation) and redox-induced resonance angle change. While the effects of surface roughness and grain size on odd-even effects in the CH_3C_nSAu SAM wetting

[†]Feng, Y.; Dionne, R. E.; Toader V.; Beaudoin G.; Badia A., Odd–Even Effects in Electroactive Self-Assembled Monolayers Investigated by Electrochemical Surface Plasmon Resonance and Impedance Spectroscopy. *J. Phys. Chem. C.* **2017**, *121*(44), 24626-24640.

properties have been established,[3] the effects of these topography characteristics on the odd-even effect in the electrochemical properties of FcC_nSAu SAMs have not been investigated.

We attribute the observation of odd-even effects on the seemingly rougher surface of the as-deposited gold to the following three aspects. First, the rms roughness within the grains, estimated to be ~0.4 nm, is like that of the template-stripped gold surface. The grains are essentially flat. Second, the mean grain size (~95 nm) is comparable to the molecular domain sizes in SAMs of CH_3C_nS and FcC_nS formed at room temperature on gold (111) single crystals or flame-annealed gold thin films with atomically flat-gold (111) terraces, which typically range from 5 to 50 nm due to kinetic limitations.[6-10] Third, the estimated grain coverage of ~80% is relatively high.

The observation of odd-even effects on both the gold thin film and gold bead electrodes indicates that the supramolecular structure of the FcC_nSAu SAM, rather than the underlying gold surface topography (i.e., asperities and defects), dominates the bulk and interface properties.

4.2 Film Structure Insights via Cyclic Voltammetry

There is a step change in the electrochemical behavior and packing density of the FcC_nSAu SAMs at $n = 9$, as indicated by the CVs and ferrocene surface coverages. The voltammetric signature evolves with chain length (Figure 3.1), from one discernible pair of redox peaks for the shorter $n = 6$ and 7 to peaks with shoulders on their anodic sides for $n = 8$ and 9, and to a dual peak regime for the longer chains ($n \geq 10$). The ferrocene surface coverage Γ_{Fc} increases by 43% from $n = 6$ (3.0×10^{-10} mol cm^{-2}) to $n = 10$ (4.3×10^{-10} mol cm^{-2}), and then varies by 14% from $n = 10$ to $n = 16$ (4.9×10^{-10} mol cm^{-2}) (Figure 3.2D). A similar variation in Γ_{Fc} with n was found on ultraflat gold: a 48% increase from $n = 6$ (3.1×10^{-10} mol cm^{-2}) to $n = 10$ (4.6×10^{-10} mol cm^{-2}), followed by a change of 11% from $n = 10$ to $n = 15$ (5.1×10^{-10} mol cm^{-2}).[2] This variation in the FcC_nS surface concentration with chain length appears to be an inherent characteristic of the system that is not replicated by MD calculations.[5] Moreover, the higher charging currents at potentials positive of the redox peaks for $n = 6$–9 reflect a looser packing structure, consistent with the lower surface coverage densities of these SAMs compared with those of $n \geq 10$. Nijhuis *et al*. report a drop in the yields of non-shorting FcC_nS junctions at $n < 8$ for Au and $n < 9$ for Ag.[5] Furthermore, the work function of FcC_nSAu SAMs is quasi-constant for $n \geq 9$ but increases with decreasing chain length for $n < 9$.[5] In the analogous CH_3C_nSAu or CH_3C_nSAg SAMs, sharp changes in properties, such as wetting and charge transport, with chain length are attributable to a transition in the physical state of the monolayer (deduced from vibrational spectroscopy), from a liquid-like phase with gauche defects for short chains ($n < 9$ for Au) to a solid-like phase of greater conformational chain order for longer chains.[11-16] The step changes in the voltammetric response and surface coverage of the FcC_nSAu SAMs may therefore also signal a transition point from a more disordered state for SAMs of $n = 6$–9 to more conformationally ordered SAMs for $n = 10$–16.

An electrochemical scanning tunneling microscopy (EC-STM) investigation of $FcC_{11}SAu$ SAMs found that the local order within the SAM increases upon oxidation and $Fc^+ClO_4^-$ ion pair formation.[17] The results of surface-enhanced Raman spectroscopy (SERS) and electrochemical quartz microbalance (EQCM) studies indicate that water penetrates

loosely-packed ferrocene-terminated SAMs,[18-19] thereby increasing the hydration of the ferrocenium. Increased hydration of the ferrocenium impedes the formation of $Fc^+ClO_4^-$ ion pairs,[18, 20] possibly resulting in greater electrostatic repulsion between the ferroceniums and larger half-peak widths for the shorter-chain FcC_nSAu SAMs of less than full coverage. Increases in Γ_{Fc}, the interchain van der Waals interactions, and conformational chain order with chain length favor the formation of close-packed $Fc^+ClO_4^-$ ion pairs (SERS data).[2, 18] This could explain the observed decrease in the overall contribution of the repulsive interactions between neighboring ferroceniums and decrease in ΔE_{fwhm} with n. Overall, the variation of the half peak widths and interaction parameters with chain length suggest that the near-constancy of the peak and apparent redox potentials is due to the combined effects of an increase in Γ_{Fc} and decrease in repulsive intermolecular interactions with increasing n.

Schematic illustrations such as those given in Figure 1.18A are idealized representations that do not convey the chain length-dependent effect of gauche bond defects on the overall alkyl chain conformation and terminal group orientation. Defects in the SAMs may obliterate the distinction between SAMs of even- and odd-numbered chains, which probably manifests itself most prominently in a difference in the orientations of their ferrocene termini in the all-trans-extended conformation (as per Figure 1.18). The more disordered the FcC_nSAu SAM, the less significant these conformational-based distinctions are expected to be. An understanding of the evolution of the FcC_nS SAM structural order as a function of the chain length, which has been primarily studied by MD simulations,[1, 5] would thus benefit from the use of vibrational spectroscopy techniques, such as infrared reflection absorption spectroscopy (IRRAS), that are sensitive to the alkyl chain conformation and orientation.[11, 22] To date there is little information on the degree of conformational chain order and dynamics in FcC_nSAu SAMs. One cannot make assumptions (for example the chain tilt angle in FcC_nSAu SAMs as in ref 23) based on the structural data obtained on the more extensively characterized CH_3C_nSAu analogues, given the important difference in their molecular packing densities. The few IRRAS investigations of these ferrocene-terminated SAMs focus on one (n = 11)[24, 26-27] or two (n = 11, 12)[27] alkyl chain lengths. Nevertheless, the reported peak frequencies of the asymmetric methylene stretching mode (ν_a), whose position is a sensitive probe of the average chain conformation and extent of the lateral interactions between polymethylene chains,[28]

indicate that the $FcC_{11}SAu$ SAM (ν_a ranging from 2922 to 2925 cm^{-1})[24-27] is more conformationally disordered than its $CH_3C_{11}SAu$ analogue (ν_a ranging from 2919 to 2920 cm^{-1})[11, 27]. This is to be expected given the mismatch between the cross-sectional areas of the terminal ferrocene (0.34 nm^2) and alkyl chain (0.19 nm^2). A systematic IRRAS characterization would complement the NEXAFS data and aid to rationalize the chain length dependencies and odd-even effects observed in the electrochemical and electronic properties of FcC_nSAu or FcC_nSAg SAM as well as the electrical performance of the SAM-based tunneling junctions.[2-5]

Altogether, the results signify that alkyl chain-chain interactions in the FcC_nSAu SAM, and resulting film structure, are not only a function of the number of methylene units, where the van der Waals chain interactions increase with n,[1] but also of the molecular packing density which varies with n. The FcC_nSAu SAMs are not structurally homologous across the molecular chain lengths investigated herein, and consequently, manifest regimes of different chain length dependencies in their physicochemical properties, as shown by the voltammetry, resonance angle, SAM capacitance, and dielectric constant data presented in the later Results chapter of the thesis.

4.3 Odd-Even Effects in the Electrochemical Parameters

The electrochemical data systematically presents odd-even alternations from $n = 6$ to $n = 16$ (Figure 3.2 A-C). Nijhuis and coworkers attribute the odd-even variation in the apparent formal potential $E^{o\prime}$ to odd-even differences in the SAM packing energy.[1-2] The smaller ferrocene tilt angle in SAM^{even} versus SAM^{odd} reduces the steric hindrance and maximizes the van der Waals interactions between the alkyl chains and lateral interactions among the ferrocene units. MD calculations predict a 1.7 ± 2.5 kJ mol^{-1} lower packing energy for SAM^{even} versus SAM^{odd}.[1-2] The magnitudes of the odd-even difference in the $E^{o\prime}$ values of the two peaks (i.e., ~2.0 kJ mol^{-1} for peak 1 and ~1.2 kJ mol^{-1} for peak 2) are comparable with this computed energy difference. [21] IRRAS studies show that the oxidation of $FcC_{11}SAu$ SAMs leads to a molecular reorientation of the alkyl chains (see next section).[19, 29] Less energy should be required to break the weaker interactions in SAM^{odd} to effect this orientation change compared to SAM^{even}, thereby resulting in a lower oxidation potential. The nonzero ΔE_p can either indicate that the oxidation and reduction of the SAM do not follow the same reverse paths or that the SAM structure changes with the ferrocene oxidation state.[31] In fact, Cruañes *et al*. demonstrated that the oxidation and reduction processes in $FcC_{11}SAu$ SAMs are affected to different degrees by pressure due to a monolayer volume expansion (of the order of 10−20 cm^3 mol^{-1}) that is coupled to the electron-transfer and ion-pairing reactions in the oxidation process.[32] This volume change is necessary to accommodate the sterically-constrained pairing of the ClO_4^- anions with all of the SAM-bound ferroceniums in high coverage SAMs. The larger ΔE_p for SAM^{even} versus SAM^{odd} is therefore consistent with the volume expansion being harder to realize due to stronger chain-chain and lateral ferrocene interactions.

The electrochemical data (Figure 3.2A-C) presents three noteworthy aspects. First, both the lower and higher potential peaks present odd-even effects, albeit to different degrees. Based on the conclusions of MD calculations and NEXAFS measurements, this implies that there are odd-even differences in the SAM packing structures and orientations of the ferrocene termini of both peak populations.[1-2] The lower potential peak 1 interestingly demonstrates the more constant and regular odd-even alternations of the electrochemical parameters (E_p, $E^{o\prime}$, ΔE_p). The odd-even difference in $E^{o\prime}$ is also more pronounced for peak 1 than peak 2. The

observed peak splitting or multiplicity is probably due to different packing structures arising from the polycrystalline nature of the gold surface.[33] An in-depth treatment of the CVs and further structural characterization are needed to determine the origin of the dual peak voltammetry. These are outside of the scope of the present work and will be the focus of a subsequent paper. Second, it is surprising that clear odd-even effects in $E^{o\prime}$ and ΔE_p are observed for SAMs of n = 6–9, as these chain lengths, due to their lower surface coverage densities, are expected to exhibit a substantial percentage of gauche defects (conformational disorder), and therefore, no significant odd-even distinction in the SAM packing structure. These odd-even effects do not seem to be related to differences in the electronic properties of the FcC_nSAu SAMs as no odd-even variations are observed in the work function, ionization potential, and offset energy between the HOMO of the ferrocene and Fermi level of the electrode for n = 6–9.[2, 5] Third, the apparent redox potential of electroactive SAMs typically shows a dependency on the surface coverage (observed experimentally and predicted by theory).[34, 35-40] The positions and $E^{o\prime}$ values of the two peaks however remain remarkably constant as a function of n, even though Γ_{Fc} increases by more than 60% from n = 6 to n = 16. $E^{o\prime}$ of peak 1 is 299 ± 5 mV for SAM^{even} and 278 ± 5 mV for SAM^{odd}. $E^{o\prime}$ of peak 2 is 410 ± 6 mV for SAM^{even} and 397 ± 9 mV for SAM^{odd}. A quasi-constant $E^{o\prime}$ is observed on template-stripped gold for n = 4–15.[2]

The Brown and Anson treatment of the voltammetric behavior of surface-confined redox species suggests that the peak potentials can remain constant if the extent of the non-ideal lateral interactions between the redox units decreases with n when the surface coverage increases with n.[38] This seems to be the case. The formal width at half-maximum (ΔE_{fwhm}) of the redox peak provides a qualitative measure of the extent of the lateral interaction between the surface-tethered redox centers.[40] ΔE_{fwhm} is 90.6 mV for the ideal case where the surface-confined ferrocene/ferrocenium centers do not interact with each other.[40] The ΔE_{fwhm}'s of the anodic peaks obtained by us (Figure S10) and Nijhuis *et al.*[2], which are > 90.6 mV for the shorter chains, decrease with increasing chain length, indicating a decrease in the repulsive interactions between the ferrocenium units. It has been shown by electrochemical quartz microbalance (EQCM) that, due to their lower packing densities, water penetrates short-chain FcC_4COOC_nSAu SAMs, thereby increasing the hydration of the ferrocenium.[41] Water uptake

has also been observed for $FcC_{11}SAu$ SAMs of low coverage.[42] Increased hydration of the ferrocenium impedes the formation of $Fc^{+}ClO_4^{-}$ ion pairs (Surface enhanced Raman spectroscopy (SERS) data),[41] possibly resulting in greater electrostatic repulsion between the ferroceniums and larger half-peak widths for the shorter-chain FcC_nSAu SAMs. Likewise, an increase in the attractive van der Waals interactions and conformational chain order with chain length favors the formation of close-packed $Fc^{+}ClO_4^{-}$ ion pairs (SERS data)[41] and could therefore result in a decrease in the overall contribution of the repulsive interactions between neighboring ferroceniums and decrease in ΔE_{fwhm} with n.[1, 43]

4.4 Chain Length Dependence of the Oxidation-Induced Thickness Change

The resonance angle change measured for the oxidation of the SAM-bound ferrocene to ferrocenium $\Delta\Theta_{\min}^{ox}$ shows two distinct dependencies with chain length (Figure 3.6). $\Delta\Theta_{\min}^{ox}$ increases from n = 6 to n = 9, mirroring the increase in Γ_{Fc} with n observed in this chain length regime. An odd-even fluctuation of $\Delta\Theta_{\min}^{ox}$ is observed for $9 \leq n \leq 16$. $\Delta\Theta_{\min}^{ox}$ of SAM^{odd} is > $\Delta\Theta_{\min}^{ox}$ of SAM^{even}. The difference in $\Delta\Theta_{\min}^{ox}$ between n_{even} and n_{odd} can be due to two effects: (i) differences in the oxidation-induced thickness change Δd^{ox} of FcC_nSAu SAMs due to the different orientations of the ferrocene termini in SAM^{even} versus SAM^{odd} or (ii) differences in the relative dielectric constant ϵ of SAM^{even} versus SAM^{odd} related to the SAM packing.[1, 5] We found that ϵ of SAM^{even} is > ϵ of SAM^{odd} for $8 \leq n \leq 16$. Furthermore, Fresnel modeling using the electrochemically-derived values of ϵ_{SAM} suggests a constant SAM thickness change. Although Figure 3.9 shows an odd-even fluctuation of ~0.03 nm in Δd^{ox} for $n \geq 9$, we cannot say whether this effect is real given the uncertainties in the values of ϵ_{SAM} and $\Delta\Theta_{\min}^{ox}$ used for the calculations. We therefore conclude that the difference in $\Delta\Theta_{\min}^{ox}$ observed between n_{even} and n_{odd} is primarily due to a difference in the dielectric constants of n_{even} and n_{odd} related to the FcC_nS packing.

A difference of 0.19 ± 0.01 nm was calculated from $\Delta\Theta_{\min}^{ox}$ between the thicknesses of the reduced and oxidized FcC_nSAu SAM. This value is comparable to the thickness changes determined for different ferrocene-terminated SAMs by in situ ellipsometry or EC-SPR, which range from 0.09 to 0.3 nm.[23, 44-45, 46] An oxidation-induced increase of 0.44 nm in the apparent height of $FcC_{11}SAu$ islands embedded in an inert CH_3C_9SAu SAM matrix was measured by electrochemical frequency modulation AFM (EFM-AFM).[47] It is important to note that the thicknesses and thickness changes obtained by ellipsometry or SPR depend on the layer model and dielectric constants used to simulate the measured parameters (Θ_{min} in SPR or Ψ and Δ in ellipsometry). We previously calculated thickness changes of 0.42 nm for $FcC_{11}SAu$ and 0.48 nm for $FcC_{12}SAu$ using the dielectric constant determined in ref 45 by in situ single-wavelength ellipsometry.[27] However, for nanometer-thick (< 20 nm) films like the FcC_nSAu SAMs, a single SPR or ellipsometry measurement cannot yield a unique thickness and

dielectric constant.[48] The dielectric constant values determined by EIS for the reduced/neutral form (ϵ_{SAM} = 2.86–3.16), and employed in the calculations in this work, are greater than the one previously used (ϵ_{SAM} = 2.14),[27] resulting in a smaller thickness change. Furthermore, the assumption that the ferrocenium and ClO_4^- anions form interfacial ion pairs, and that the dielectric constants of the reduced and oxidized forms are the same, is probably only valid for SAMs of $n \gtrsim 9$, which form full or close to full coverage monolayers.[49-53] Water penetration into the shorter-chain SAMs during ferrocene oxidation may alter the SAM dielectric constant.[41-42]

There are several possible causes of the observed SAM thickness change and related SAM volume change detected by high pressure voltammetry.[23, 32, 44-46] Two spectroelectrochemical investigations (IRRAS of $FcC_{11}SAu$ SAMs and SERS of a chemically homologous series of FcC_4COOC_nSAu SAMs) conclude, from the observed changes in the CH_2 stretching band intensities, that the oxidation of the SAM-bound ferrocenes and formation of $Fc^+ClO_4^-$ ion pairs induce a molecular reorientation, whereby the alkyl chains adopt a more perpendicular orientation with respect to the electrode surface (Figure 1.18A).[29, 41, 52] A study using subtractively normalized interfacial Fourier transform infrared spectroscopy (SNIFTIRS) of $FcCOC_nSAu$ SAMs however concludes that there is little or no movement of the alkyl chains and that the ferrocene groups rotate/flip to a position normal to the electrode surface.[55] There is also the possibility (coverage dependent) of water molecules being incorporated into the oxidized SAM.[41, 52] The SAM thickness changes calculated herein from the resonance angle shifts and measured by EC-AFM cannot be solely accounted for by a rotation of the ferroceniums, which is estimated to give a maximum variation of 0.0585 nm,[23] and must therefore involve a change in the tilt, and possibly the conformation of the alkyl chains (vide infra). MD simulations indicate that the alkyl chain tilt angle (with respect to the surface normal) in FcC_nSAu SAMs decreases with chain length, from ~31° for n = 6 to ~17° for n = 15.[5, 56] Using the computed chain tilt angles and effective thickness changes determined by EC-SPR (Figure 3.9), a reasonable concordance is obtained between the oxidized SAM thickness and thickness expected for FcC_nS chains oriented perpendicular to the surface (Figure S11). SERS of FcC_4COOC_nSAu SAMs and MD simulations of FcC_nSAu SAMs point to the oxidized SAM being more disordered than its reduced form.[41, 57] However,

electrochemical scanning tunneling microscopy images of the reduced and oxidized states of $FcC_{11}SAu$ SAMs formed on Au(111) show an increase in the local order within the SAM upon oxidation.[43] Consistent with this finding, EQCM measurements on $FcC_{11}SAu$ SAMs show that for a close-packed SAM, the oxidized monolayer and associated ClO_4^- anions behave as a rigid layer.[51] Moreover, the formation of interfacial $Fc^+ClO_4^-$ pairs was found to inhibit the mediated oxidation of a solution redox species through the ferrocene-terminated SAM.[49] This electron transfer inhibition was explained in terms of the formation of a rigid two-dimensional $Fc^+ClO_4^-$ network which restricts the movement of the electron-accepting ferrocenium terminus. The latter results suggest that the association of the ClO_4^- anion to the SAM-bound ferrocenium has an ordering effect on the SAM so that we do not believe that the redox-induced thickness change is due to disordering of the SAM. The discordance between the results of the different experimental studies may arise from the structure of the ferrocene thiol precursor or roughness of the surface used in the SERS investigation. The polar ester group can perturb the chain-chain interactions and promote the ingress of water in the FcC_4COOC_nSAu SAMs. We thus conclude that untilting of the alkyl chains, which may also include a change in orientation of the ferrocenium termini,[42] is the most probable process (Figure 1.18A).

4.5 Dielectric Properties of the FcC$_n$SAu SAMs

The impedance spectra (Figure 3.7) indicate that FcC$_n$SAu SAMs of n = 7 – 16 chain lengths behave as nearly ideal capacitors in their reduced state (0 V vs. Ag/AgCl) in 0.1 M $NaClO_{4(aq)}$ over the frequency range of 1 Hz to 100 kHz. The progressive linear increase of the reciprocal of the SAM capacitance C_{SAM}^{-1} with increasing chain length (Figure 3.8A) is in line with expectations of progressive increases in the hydrophobic SAM dielectric thickness d and decrease in the double-layer capacitance C^{-1} (equation 31). Despite lower FcC$_n$S surface coverages, SAMs of $7 \leq n < 10$ present phase angles of 89º at low frequency (Table S1) under the experimental conditions used and C_{SAM}^{-1} does not deviate from the linear trend with n. An odd-even effect in the SAM capacitance is however only evident between n = 10 and n = 16 (Figure 3.8A inset), regime where the ferrocene surface coverage and voltammetric signature suggest the SAMs to be more structurally homologous.

The parallel plate capacitor approximation (equation 31) was used to calculate the SAM dielectric constant ϵ_{SAM} from the SAM capacitance. ϵ_{SAM} depends on the value of the SAM thickness used. Computed values were used for the SAM thickness (as per other studies)[11, 30] since there is a relative uncertainty of ~20-30% (absolute uncertainty of ±0.4 nm) in the thicknesses determined by angle-resolved XPS.[2] Instead of determining an average value over a range of chain lengths from the slope of the C_{SAM}^{-1} versus d (or n) plot,[12-13, 21, 30] we calculate a ϵ_{SAM} value for each chain length (Figure 3.8B) to reveal the structure-related variation of ϵ_{SAM}. ϵ_{SAM} remains nearly constant with chain length. Recent theoretical calculations (ab initio or density functional theory) of surface-tethered monolayer films of saturated n-alkyl chains predict a linear increase in ϵ_{SAM} with the surface coverage density and, for a fixed molecular density (i.e., 3.0 molecules nm^{-2}), no dependence in ϵ_{SAM} with chain length.[41, 43, 49] Even though the FcC$_n$S density increases from 2.0 molecules nm^{-2} for n = 7 to 3.0 molecules nm^{-2} for n = 16, we do not observe an overall increase in the measured ϵ_{SAM}, as predicted.[41]

Nevertheless, there is a statistically significant odd-even variation of ϵ_{SAM}. Such an effect was not considered by the aforementioned theoretical studies. [41, 43, 49] We find values of ϵ_{SAM} of 3.08 ± 0.03 for n_{even} and 2.86 ± 0.01 for n_{odd} for n = 10–16. It is important to note that

there is no systematic alternation between n_{even} and n_{odd} in either the computed or experimentally-determined FcC_nSAu SAM thicknesses.[1-2] Nijhuis *et al*. also found an odd-even difference in the resistance, capacitance, and dielectric constant of $CH_3(CH_2)_nS$ SAMs, where n = 5–17, sandwiched between GaOx/EGaIn and Ag electrodes.[30] Using a parallel plate capacitor model, they calculated a ϵ_{SAM} value of 3.5 ± 0.2 for junctions with n_{odd} and 3.1 ± 0.1 for junctions with n_{even} (reversal of odd-even effect on silver)[1, 5]. We thus believe that the odd-even effect in ϵ_{SAM} originates from differences in the intrinsic SAM structure. More importantly, the odd-even differences in the dielectric properties of the FcC_nSAu SAMs demonstrated here are perhaps the most compelling evidence to date of odd-even differences in the interactions and packing of the alkyl chains in these SAMs predicted by MD calculations.[1, 5] It would be of interest to eventually use two-color (or two-wavelength) SPR to simultaneously and unambiguously measure the FcC_nSAu SAM thickness and dielectric constant as a function of n.[48, 52]

Reference

(1) Nerngchamnong, N.; Yuan, L.; Qi, D.-C.; Li, J.; Thompson, D.; Nijhuis, C. A. The Role of van der Waals Forces in the Performance of Molecular Diodes. *Nat. Nanotechnol.* **2013,** *8*, 113-118.

(2) Nerngchamnong, N.; Thompson, D.; Cao, L.; Yuan, L.; Jiang, L.; Roemer, M.; Nijhuis, C. A. Nonideal Electrochemical Behavior of Ferrocenyl–Alkanethiolate SAMs Maps the Microenvironment of the Redox Unit. *J. Phys. Chem. C* **2015,** *119*, 21978-21991.

(3) Wang, Z.; Chen, J.; Gathiaka, S. M.; Oyola-Reynoso, S.; Thuo, M. Effect of Substrate Morphology on the Odd–Even Effect in Hydrophobicity of Self-Assembled Monolayers. *Langmuir* **2016,** *32*, 10358-10367.

(4) Yuan, L.; Jiang, L.; Zhang, B.; Nijhuis, C. A. Dependency of the Tunneling Decay Coefficient in Molecular Tunneling Junctions on the Topography of the Bottom Electrodes. *Angew. Chemie Int. Ed.* **2014,** *53*, 3377-3381.

(5) Yuan, L.; Thompson, D.; Cao, L.; Nerngchangnong, N.; Nijhuis, C. A. One Carbon Matters: The Origin and Reversal of Odd–Even Effects in Molecular Diodes with Self-Assembled Monolayers of Ferrocenyl-Alkanethiolates. *J. Phys. Chem. C* **2015,** *119*, 17910-17919.

(6) Fenter, P.; Eisenberger, P.; Liang, K. S. Chain-length Dependence of the Structures and Phases of $CH_3(CH_2)_{n-1}SH$ Self-Assembled on Au(111). *Phys. Rev. Lett.* **1993,** *70*, 2447-2450.

(7) Poirier, G. E. Characterization of Organosulfur Molecular Monolayers on Au(111) using Scanning Tunneling Microscopy. *Chem. Rev.* **1997,** *97*, 1117–1127.

(8) O'Dwyer, C.; Gay, G.; Viaris de Lesegno, B.; Weiner, J. The Nature of Alkanethiol Self-Assembled Monolayer Adsorption on Sputtered Gold Substrates. *Langmuir* **2004,** *20*, 8172-8182.

(9) Müller-Meskamp, L.; Karthäuser, S.; Waser, R.; Homberger, M.; Wang, Y.; Englert, U.; Simon, U. Structural Ordering of w-Ferrocenylalkanethiol Monolayers on Au(111) Studied by Scanning Tunneling Microscopy. *Surf. Sci.* **2009,** *603*, 716-722.

(10) Nerngchamnong, N.; Wu, H.; Sotthewes, K.; Yuan, L.; Cao, L.; Roemer, M.; Lu, J.; Loh, K. P.; Troadec, C.; Zandvliet, H. J. W.; Nijhuis, C. A. Supramolecular Structure

of Self-Assembled Monolayers of Ferrocenyl Terminated n-Alkanethiolates on Gold Surfaces. *Langmuir* **2014,** *30*, 13447-13455.

(11) Porter, M. D.; Bright, T. B.; Allara, D. L.; Chidsey, C. E. D. Spontaneously Organized Molecular Assemblies. 4. Structural Characterization of n-Alkyl Thiol Monolayers on Gold by Optical Ellipsometry, Infrared Spectroscopy, and Electrochemistry. *J. Am. Chem. Soc.* **1987,** *109*, 3559-3568.

(12) Jiang, L.; Sangeeth, C. S. S.; Yuan, L.; Thompson, D.; Nijhuis, C. A. One-Nanometer Thin Monolayers Remove the Deleterious Effect of Substrate Defects in Molecular Tunnel Junctions. *Nano Letters* **2015,** *15*, 6643-6649.

(13) Chen, J.; Chang, B.; Oyola-Reynoso, S.; Wang, Z.; Thuo, M. Quantifying Gauche Defects and Phase Evolution in Self-Assembled Monolayers through Sessile Drops. *ACS Omega* **2017,** *2*, 2072-2084.

(14) Laibinis, P. E.; Whitesides, G. M.; Allara, D. L.; Tao, Y. T.; Parikh, A. N.; Nuzzo, R. G. Comparison of the Structures and Wetting Properties of Self-Assembled Monolayers of n-Alkanethiols on the Coinage Metal Surfaces, Copper, Silver, and Gold. *J. Am. Chem. Soc.* **1991,** *113*, 7152-7167.

(15) Biebuyck, H. A.; Bain, C. D.; Whitesides, G. M. Comparison of Organic Monolayers on Polycrystalline Gold Spontaneously Assembled from Solutions Containing Dialkyl Disulfides or Alkanethiols. *Langmuir* **1994,** *10*, 1825-1831.

(16) Chen, J.; Liu, J.; Tevis, I. D.; Andino, R. S.; Miller, C. M.; Ziegler, L. D.; Chen, X.; Thuo, M. M. Spectroscopic Evidence for the Origin of Odd-Even Effects In Self-Assembled Monolayers and Effects of Substrate Roughness. *Phys. Chem. Chem. Phys.* **2017,** *19*, 6989-6995.

(17) Rudnev, A. V.; Yoshida, K.; Wandlowski, T. Electrochemical Characterization of Self-Assembled Ferrocene-Terminated Alkanethiol Monolayers on Low-Index Gold Single Crystal Electrodes. *Electrochim. Acta* **2013,** *87*, 770-778.

(18) Kazakevičienė, B.; Valincius, G.; Niaura, G.; Talaikytė, Z.; Kažemėkaitė, M.; Razumas, V.; Plaušinaitis, D.; Teišerskienė, A.; Lisauskas, V. Mediated Oxidation of Ascorbic Acid on a Homologous Series of Ferrocene-Terminated Self-Assembled Monolayers. *Langmuir* **2007,** *23*, 4965–4971.

(19) Ye, S.; Haba, T.; Sato, Y.; Shimuza, K.; Uosaki, K. Coverage Dependent Behavior of Redox Reaction Induced Structure Change and Mass Transport at an 11-Ferrocenyl-1-Undecanethiol Self-Assembled Monolayer on a Gold Electrode Studied by an In Situ IRRAS-EQCM Combined System. *Phys. Chem. Chem. Phys.* **1999,** *1*, 3653–3659.

(20) Valincius, G.; Niaura, G.; Kazakevičienė, B.; Talaikytė, Z.; Kažemėkaitė, M.; Butkus, E.; Razumas, V. Anion Effect on Mediated Electron Transfer Through Ferrocene-Terminated Self-Assembled Monolayers. *Langmuir* **2004,** *20*, 6631–6638.

(21) Rampi, M. A.; Schueller, O. J. A.; Whitesides, G. M. Alkanethiol Self-Assembled Monolayers as the Dielectric of Capacitors with Nanoscale Thickness. *Appl. Phys. Lett.* **1998,** *14*, 1781-1783.

(22) Nuzzo, R. G.; Dubois, L. H.; Allara, D. L. Fundamental Studies of Microscopic Wetting on Organic Surfaces. 1. Formation and Structural Characterization of a Self-Consistent Series of Polyfunctional Organic Monolayers. *J. Am. Chem. Soc.* **1990,** *112*, 558-569.

(23) Yao, X.; Wang, J.; Zhou, F.; Wang, J.; Tao, N. Quantification of Redox-Induced Thickness Changes of 11-Ferrocenylundecanethiol Self-Assembled Monolayers by Electrochemical Surface Plasmon Resonance. *J. Phys. Chem. B* **2004,** *108*, 7206–7212.

(24) Uosaki, K.; Sato, Y.; Kita, H. Electrochemical Characteristics of a Gold Electrode Modified with a Self-Assembled Monolayer of Ferrocenylalkanethiols. *Langmuir* **1991,** *7*, 1510–1514.

(25) Popenoe, D. D.; Deinhammer, R. S.; Porter, M. D. Infrared Spectroelectrochemical Characterization of Ferrocene-Terminated Alkanethiolate Monolayers at Gold. *Langmuir* **1992,** *8*, 2521–2530.

(26) Tian, H.; Dai, Y.; Shao, H.; Yu, H.-Z. Modulated Intermolecular Interactions in Ferrocenylalkanethiolate Self-Assembled Monolayers on Gold. *J. Phys. Chem. C* **2012,** *117*, 1006-1012.

(27) Norman, L. L.; Badia, A. Microcantilevers Modified with Ferrocene-Terminated Self-Assembled Monolayers: Effect of Molecular Structure and Electrolyte Anion on the Redox-Induced Surface Stress. *J. Phys. Chem. C* **2011,** *115*, 1985-1995.

(28) Snyder, R. G.; Maroncelli, M.; Strauss, H. L.; Hallmark, V. M. Temperature and Phase Behavior of Infrared Intensities: The Poly(Methylene) Chain. *J. Phys. Chem.* **1986,** *90*, 5623-5630.

(29) Ye, S.; Sato, Y.; Uosaki, K. Redox-Induced Orientation Change of a Self-Assembled Monolayer of 11-Ferrocenyl-1-undecanethiol on a Gold Electrode Studied by *in Situ* FT-IRRAS. *Langmuir* **1997,** *13*, 3157–3161.

(30) Jiang, L.; Sangeeth, C. S. S.; Nijhuis, C. A. The Origin of the Odd–Even Effect in the Tunneling Rates across EGaIn Junctions with Self-Assembled Monolayers (SAMs) of n-Alkanethiolates. *J. Am. Chem. Soc.* **2015,** *137*, 10659-10667.

(31) Finklea, H. O. Electrochemistry of Organized Monolayers of Thiols and Related Molecules on Electrodes. In *Electroanalytical Chemistry: A Series of Advances*, Bard, A. J.; Rubinstein, I., Eds.; Marcel Dekker: New York, 1996; Vol. 19, 109–335.

(32) Cruañes, M. T.; Drickamer, H. G.; Faulkner, L. R. Characterization of Charge Transfer Processes in Self-Assembled Monolayers by High-Pressure Electrochemical Techniques. *Langmuir* **1995,** *11*, 4089–4097.

(33) Zhong, C.-J.; Zak, J.; Porter, M. D. Voltammetric Reductive Desorption Characteristics of Alkanethiolate Monolayers at Single Crystal Au(111) and (110) Electrode Surfaces. *J. Electroanal. Chem.* **1997,** *421*, 9-13.

(34) Chidsey, C. E. D.; Bertozzi, C. R.; Putvinski, T. M.; Mujsce, A. M. Coadsorption of Ferrocene-Terminated and Unsubstituted Alkanethiols on Gold: Electroactive Self-Assembled Monolayers. *J. Am. Chem. Soc.* **1990,** *112*, 4301–4306.

(35) Dionne, E. R.; Toader, V.; Badia, A. Microcantilevers Bend to the Pressure of Clustered Redox Centers. *Langmuir* **2014,** *30*, 742-752.

(36) Lee, L. Y. S.; Sutherland, T. C.; Rucareanu, S.; Lennox, R. B. Ferrocenylalkythiolates as a Probe of Heterogeneity in Binary Self-Assembled Monolayers on Gold. *Langmuir* **2006,** *22*, 4438–4444.

(37) Brown, A. P.; Anson, F. C. Cyclic and Differential Pulse Voltammetric Behavior of Reactants Confined to the Electrode Surface. *Anal. Chem.* **1977,** *49*, 1589-1595.

(38) Brown, A. P.; Anson, F. C. Cyclic and Differential Pulse Voltammetric Behavior of Reactants Confined to the Electrode Surface. *Anal. Chem.* **1977,** *49*, 1589-1595.

(39) Creager, S. E.; Rowe, G. K. Solvent and Double-Layer Effects on Redox Reactions in Self-Assembled Monolayers of Ferrocenyl-Alkanethiolates on Gold. *J. Electroanal. Chem.* **1997,** *420*, 291-299.

(40) Laviron, E. Surface Linear Sweep Voltammetry: Equation of the Peaks for a Reversible Reaction When Interactions Between Adsorbed Molecules are Taken into Account. *J. Electroanal. Chem.* **1974,** *52*, 395-402.

(41) Gala, F.; Zollo, G. Dielectric Properties of Self-Assembled Monolayer Coatings on a (111) Silicon Surface. *J. Phys. Chem. C* **2015,** *119*, 7264-7274.

(42) Shimazu, K.; Yagi, I.; Sato, Y.; Uosaki, K. Electrochemical Quartz Crystal Microbalance Studies of Self-Assembled Monolayers of 11-Ferrocenyl-1-Undecanethiol: Structure-Dependent Ion-Pairing and Solvent Uptake. *J. Electroanal. Chem.* **1994,** *372*, 117–124.

(43) Van Dyck, C.; Marks, T. J.; Ratner, M. A. Chain Length Dependence of the Dielectric Constant and Polarizability in Conjugated Organic Thin Films. *ACS Nano* **2017,** *11*, 5970-5981.

(44) Viana, A. S.; Jones, A. H.; Abrantes, L. M.; Kalaji, M. Redox Induced Orientational Changes in a Series of Short Chain Ferrocenyl Alkyl Thiols Self-Assembled on Gold(III) Electrodes. *J. Electroanal. Chem.* **2001,** *500*, 290–298.

(45) Ohtsuka, T.; Sato, K.; Uosaki, K. Dynamic Ellipsometry of a Self-Assembled Monolayer of a Ferrocenylalkanethiol During Oxidation-Reduction Cycles. *Langmuir* **1994,** *10*, 3658–3662.

(46) Abrantes, L. M.; Kalaji, M.; Viana, A. S. In Situ Ellipsometric Study of Redox Induced Orientation of a Short Chained Ferrocenylalkylthiol Monolayer Self-Assembled on Gold. *Russ. J. Electrochem.* **2002,** *38*, 39–43.

(47) Umeda, K.-i.; Fukui, K.-i. Observation of Redox-State-Dependent Reversible Local Structural Change of Ferrocenyl-Terminated Molecular Island by Electrochemical Frequency Modulation AFM. *Langmuir* **2010,** *26*, 9104-9110.

(48) Peterlinz, K. A.; Georgiadis, R. In Situ Kinetics of Self-Assembly by Surface Plasmon Resonance Spectroscopy. *Langmuir* **1996,** *12*, 4731-4740.

(49) Heitzer, H. M.; Marks, T. J.; Ratner, M. A. Maximizing the Dielectric Response of Molecular Thin Films via Quantum Chemical Design. *ACS Nano* **2014,** *8*, 12587-12600.

(50) Viana, A. S.; Kalaji, M.; Abrantes, L. M. Electrochemical Quartz Crystal Microbalance Study of Self-Assembled Monolayers and Multilayers of Ferrocenylthiol Derivatives on Gold. *Langmuir* **2003,** *19*, 9542-9544.

(51) Goujon, F.; Bonal, C.; Limoges, B.; Malfreyt, P. Molecular Dynamics Simulations of Ferrocene-Terminated Self-Assembled Monolayers. *J. Phys. Chem. B* **2010,** *114*, 6447-6454.

(52) Liang, H.; Miranto, H.; Granqvist, N.; Sadowski, J. W.; Viitala, T.; Wang, B.; Yliperttula, M. Surface Plasmon Resonance Instrument as a Refractometer for Liquids and Ultrathin Films. *Sens. Actuators, B* **2010,** *149*, 212-220.

(53) Kawaguchi, T.; Tada, K.; Shimazu, K. Redox and Mass Transport Characteristics of Domain-Free Mixed Ferrocenyloctanethiol/Alkanethiol Monolayers on Gold. *J. Electroanal. Chem.* **2003,** *543*, 41-49.

(54) Jung, L. S.; Campbell, C. T.; Chinowsky, T. M.; Mar, M. N.; Yee, S. S. Quantitative Interpretation of the Response of Surface Plasmon Resonance Sensors to Adsorbed Films. *Langmuir* **1998,** *14*, 5636-5648.

(55) Viana, A. S.; Jones, A. H.; Abrantes, L. M.; Kalaji, M. Redox Induced Orientational Changes in a Series of Short Chain Ferrocenyl Alkyl Thiols Self-Assembled on Gold(111) Electrodes. *J. Electroanal. Chem.* **2001,** *500*, 290-298.

(56) Wang, S.; Wei, M.-Z.; Hu, G.-C.; Wang, C.-K.; Zhang, G.-P. Mechanisms of the Odd-Even Effect and its Reversal in Rectifying Performance of Ferrocenyl-n-Alkanethiolate Molecular Diodes. *Org. Electron.* **2017,** *49*, 76-84.

(57) Thompson, D.; Nijhuis, C. A. Even the Odd Numbers Help: Failure Modes of SAM-Based Tunnel Junctions Probed via Odd-Even Effects Revealed in Synchrotrons and Supercomputers. *Acc. Chem. Res.* **2016,** *49*, 2061-2069.

Chapter 5. Summary and Conclusions

Our findings indicate that the FcC_nSAu SAMs are not structurally homologous in terms of their molecular packing density and structural order across the chain lengths n = 6–16 investigated. The cyclic voltammograms and electrochemically-determined ferrocene surface coverages suggest a change in the SAM structure between n = 9 and 10. Structural differences between SAMs of n = 6–9 and those of n = 10–16 are reflected in the oxidation-induced resonance angle shift, double-layer capacitance, and SAM dielectric constant which exhibit odd-even variations beginning at n = 9 or 10. This behavior is consistent with expectations that the alkyl chains in the more loosely-packed SAMs of n < 10 are more conformationally disordered and that gauche defects blur the distinction between SAM^{odd} and SAM^{even} related to differences in the molecular packing and orientation of the ferrocene termini in the trans-extended conformation.

Despite indications of two distinct regimes, the apparent redox potential shows odd-even alternations across the entire range of chain lengths n = 6–16. This suggests that the odd-even effect in the SAM redox potential may not only reflect ferrocene-tilt-angle related differences in the lateral interactions among the ferrocene units and SAM packing energy, as postulated by Nijhuis and coworkers.[1-2] The different chain length dependencies observed for the SAM redox potential, double-layer capacitance, and dielectric constant highlight the need for more advanced electrochemical characterization and studies of the evolution of the FcC_nSAu SAM structure and conformational order with chain length in both the reduced and oxidized forms.

The resonance angle shift measured for the oxidation of the SAM-bound ferrocene to ferrocenium exhibits an odd-even effect, with SAM^{odd} giving a larger shift (~0.001°) than SAM^{even} . This odd-even difference originates from a difference of ~0.2 in the dielectric constants of SAM^{odd} and SAM^{even}, which is attributable to intrinsic differences in the SAM packing structure. The ability of SPR to resolve such small differences in the resonance angle demonstrates its superb sensitivity to changes in the dielectric constant at a metal surface.

A chain length-independent SAM thickness change of 0.19 nm was estimated from the mean resonance angle shifts and SAM dielectric constant values, demonstrating that SAM^{even} and SAM^{odd} undergo the same ferrocene-oxidation-induced molecular reorientations.

Reference

1. Nerngchamnong, N.; Yuan, L.; Qi, D.-C.; Li, J.; Thompson, D.; Nijhuis, C. A. The Role of van der Waals Forces in the Performance of Molecular Diodes. *Nat. Nanotechnol.* **2013,** *8*, 113-118.
2. Nerngchamnong, N.; Thompson, D.; Cao, L.; Yuan, L.; Jiang, L.; Roemer, M.; Nijhuis, C. A. Nonideal Electrochemical Behavior of Ferrocenyl–Alkanethiolate SAMs Maps the Microenvironment of the Redox Unit. *J. Phys. Chem. C* **2015,** *119*, 21978-21991.

Supporting Information

Syntheses of ω-Ferrocenylalkanethiols ($Fc(CH_2)_nSH$, referred to as FcC_nSH)

Materials: Ferrocene (98%), $AlCl_3$ (99+%), titanium tetrachloride ($TiCl_4$, 1M in dichloromethane), triethylsilane (99%), thiourea (99%), 6-bromohexanoyl chloride (97%), 11-bromoundecanoic acid (99%), cyclododecanone (≥99%), 16-hexadecanolide (97%) were purchased from Sigma Aldrich and used as received. 9-bromononan-1ol (98%) and pentadecanolide (98%) were obtained from Alfa Aesar. 13-bromotridecanoic acid was purchased from Arch Bioscience Company and used without further purification. 7-bromoheptanoic acid (97%) was purchased from Acros Organics. 9-bromononanoic acid was obtained by oxidation of 9-bromononan-1-ol.[1] 10-bromodecanoic acid was obtained by $KMnO_4$ oxidation of 11-bromo-1-undecene.[2] 12-bromododecanoic acid was synthesized according to literature procedures.[3-5] 14-bromotetradecanoic acid was previously synthesized by bromination of 14-hydroxytetradecanoic acid obtained following the procedure of Sato and al.[6] 15-bromopentadecanoic acid and 16-bromohexadecanoic acid were obtained in high yields by hydrolysis of 16-hexadecanolide and pentadecanolide, respectively, followed by bromination of the corresponding intermediates, n-hydroxyalkanoic acids. 8-Mercaptooctyl ferrocene, previously synthesized in house[7], was purified prior to the analytical measurements.

Dried solvents were obtained from an MBraun Solvent Purification System. ^1H and ^{13}C NMR spectra were recorded on a Varian Mercury 300, Varian Mercury 400 and/or Bruker AVIIIHD 500 (depending of the availability of the instruments) using chloroform-d or methanol-d_4 as a solvent. High resolution electrospray ionization (ESI) mass spectra were recorded on an Exactive Plus Orbitrap-API instrument (ThermoFisher Scientific). Melting points were recorded on a TA Instruments DSC Q2000 differential scanning calorimetry instrument (heating rate of 10 °C/min).

The ω-ferrocenylalkanethiols **(5)** ($Fc(CH_2)_nSH$, n = 6, 7, 9–16) were obtained following the successive reactions shown in S1.

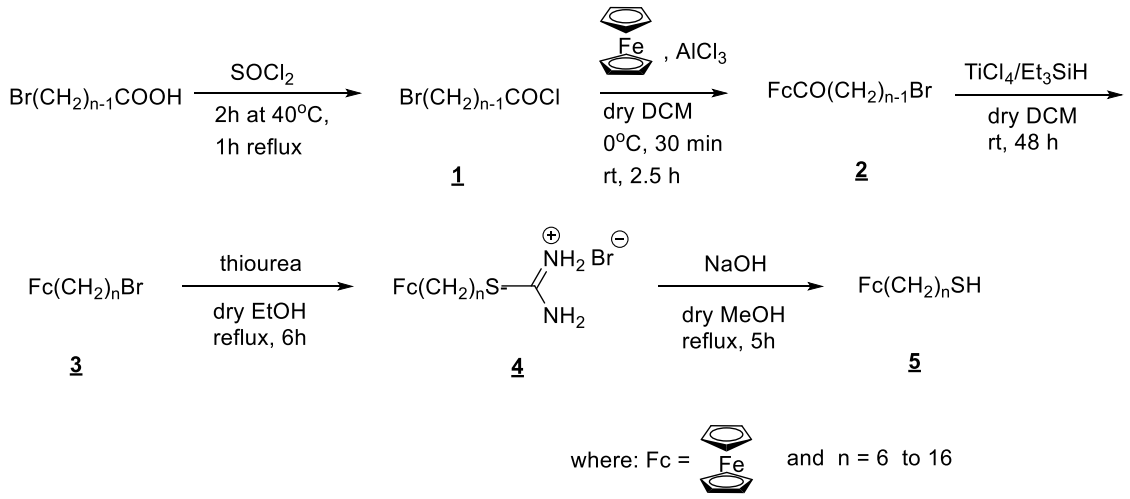

S1. Synthesis of the *ω*-ferrocenylalkanethiols

Synthesis of ω - bromoalkanoyl chloride (Br(CH₂)$_{n-1}$COCl) (**1**)

ω-Bromoalkanoic acid ($Br(CH_2)_{n-1}COOH$, n=7,9-16) (1 eq.) was reacted, under an inert atmosphere, with $SOCl_2$ (7 eq.) at 40 ºC for 2 hours, followed by 1 hour at reflux. The excess of thionyl chloride was removed by distillation at atmospheric pressure and the resulted acyl chloride was used for the next step without further purification.

Br(CH₂)₆COCl ^{1}H NMR (400 MHz, $CDCl_3$): δ 3.40 (t, 2H, J=6.8 Hz, Br-C*H*$_2$-CH$_2$~), 2.90 (t, 2H, J=7.6Hz, ~CH$_2$-C*H*$_2$COCl), 1.86 (p, 2H, J=7.2 Hz, Br-CH$_2$-C*H*$_2$~), 1.73 (p, 2H, J=7.6 Hz, ~C*H*$_2$-CH$_2$COCl), 1.53-1.35 (m, 4H, Br-CH$_2$-CH$_2$-C*H*$_2$~).

^{13}C-NMR (125 MHz, $CDCl_3$):δ173.70, 77.31, 77.05, 76.80, 46.93, 33.58, 32.35, 27.61, 27.56, 24.86.

$Br(CH_2)_8COCl$ ^{1}H NMR (400 MHz, $CDCl_3$): δ 3.41 (t, 2H, J=6.8Hz, Br-C*H*$_2$-CH_2~), 2.89 (t, 2H, J=7.2Hz, ~CH_2-C*H*$_2$COCl), 1.86 (p, 2H, J=6.8 Hz, Br-CH_2-C*H*$_2$~), 1.72 (p, 2H, J=7.2Hz, ~C*H*$_2$-CH_2COCl), 1.60-1.34 (m, 8H, Br-CH_2-CH_2-C*H*$_2$~).

$Br(CH_2)_9COCl$ ^{1}H NMR (300 MHz, $CDCl_3$): δ 3.41 (t, 2H, J=6.9 Hz, Br-C*H*$_2$-CH_2~), 2.89 (t, 2H, J=6.9 Hz, ~CH_2-C*H*$_2$COCl), 1.86 (p, 2H, J= 7.2 Hz, Br-CH_2-C*H*$_2$~), 1.71 (p, 2H, J=7.2 Hz, ~C*H*$_2$-CH_2COCl), 1.50-1.31 (m, 10H, Br-CH_2-CH_2-C*H*$_2$~).

$Br(CH_2)_{10}COCl$ ^{1}H NMR (400 MHz, $CDCl_3$): δ 3.40 (t, 2H, J=6.8 Hz, Br-C*H*$_2$-CH_2~), 2.88 (t, 2H, J=7.6 Hz, ~CH_2-C*H*$_2$COCl), 1.85 (p, 2H, J=6.4 Hz, Br-CH_2-C*H*$_2$~), 1.70 (p, 2H, J=6.8 Hz, ~C*H*$_2$-CH_2COCl), 1.50-1.29 (m, 12H, Br-CH_2-CH_2-C*H*$_2$~).

$Br(CH_2)_{11}COCl$ ^{1}HNMR (400 MHz, $CDCl_3$): δ 3.41 (t, 2H, J=6.8 Hz, Br-C*H*$_2$-CH_2~), 2.88 (t, 2H, J=6.8 Hz, ~CH_2-C*H*$_2$COCl), 1.85 (p, 2H, J=6.8 Hz, Br-CH_2-C*H*$_2$~), 1.71 (p, 2H, J=7.4 Hz, ~C*H*$_2$-CH_2COCl), 1.50-1.28 (m, 14H, Br-CH_2-CH_2-C*H*$_2$~).

$Br(CH_2)_{12}COCl$ ^{1}H NMR (400 MHz, $CDCl_3$): δ 3.42 (t, 2H, J=6.4 Hz, Br-C*H*$_2$-CH_2~), 2.89 (t, 2H, J=6.8 Hz, ~CH_2-C*H*$_2$COCl), 1.86 (p, 2H, J=6.8 Hz, Br-CH_2-C*H*$_2$~), 1.71 (p, 2H, J=7.2 Hz, ~C*H*$_2$-CH_2COCl), 1.45-1.28 (m, 16H, Br-CH_2-CH_2-C*H*$_2$~).

$Br(CH_2)_{13}COCl$ ^{1}H NMR (400 MHz, $CDCl_3$): δ 3.41 (t, 2H, J=6.8 Hz, Br-C*H*$_2$-CH_2~), 2.89 (t, 2H, J=6.8 Hz, ~CH_2-C*H*$_2$COCl), 1.86 (p, 2H, J=7.2 Hz, Br-CH_2-C*H*$_2$~), 1.71 (p, 2H, J=7.2 Hz, ~C*H*$_2$-CH_2COCl), 1.45-1.27 (m, 18H, Br-CH_2-CH_2-C*H*$_2$~).

$Br(CH_2)_{14}COCl$ ^{1}H NMR (500 MHz, $CDCl_3$): δ 3.41 (t, 2H, J = 8.5 Hz, Br-C*H*$_2$-CH_2~), 2.88 (t, 2H, J = 9.0 Hz, ~CH_2-C*H*$_2$COCl), 1.85 (p, 2H, J = 9.5 Hz, Br-CH_2-C*H*$_2$~), 1.70 (p, 2H, J = 9.5 Hz, ~C*H*$_2$-CH_2COCl), 1.47-1.20 (m, 20H, Br-CH_2-CH_2-C*H*$_2$~).

$Br(CH_2)_{15}COCl$ ^{1}H NMR (300 MHz, $CDCl_3$): δ 3.41 (t, 2H, J=7.2 Hz, Br-C*H*$_2$-CH_2~), 2.88 (t, 2H, J=7.2 Hz, ~CH_2-C*H*$_2$COCl), 1.85 (p, 2H, J=6.9 Hz, Br-CH_2-C*H*$_2$~), 1.71 (p, 2H, J=7.2 Hz, ~C*H*$_2$-CH_2COCl), 1.45-1.26 (m, 22H, Br-CH_2-CH_2-C*H*$_2$~).

Synthesis of ω - bromoalkanoylferrocene ($FcCO(CH_2)_{n-1}Br$) (**2**)[5]

Ferrocene (1 eq.) in dry dichloromethane (final concentration of 0.6 M) was cooled on an ice bath. $AlCl_3$ (1 eq.) was added in one portion (solution turned color from yellow to brown), followed by the drop-wise addition of *ω*-bromoalkanoyl chloride ($Br(CH_2)_{n-1}COCl$, n=6,7,9-16) (1 eq.) (solution turned color to dark violet). After the total addition of the acylchloride, the reaction mixture was stirred at 0 ºC for 30 min. when the ice bath was removed and the stirring was continued at room temperature for 2.5 h. The reaction was quenched by careful addition of water; the organic phase was separated, and the aqueous layer was extracted twice with dichloromethane. The combined halogenated layers were dried over $MgSO_4$ and the solvent was removed under reduced pressure. The crude product was purified by flash column chromatography (SiO_2, hexanes:ethyl acetate, 4:1 (v:v) unless otherwise specified).

$FcCO(CH_2)_5Br$ (78.4%, R_f = 0.53)

^{1}H NMR (400 MHz, $CDCl_3$): δ 4.78 (t, 2H, J = 2.0 Hz, H_{Fc} *ortho* to C(O)CH_2 ~), 4.50 (t, 2H, *J* = 2 Hz, H_{Fc} *meta* to C(O)CH_2), 4.20 (s, 5H, H_{Fc}), 3.45 (t, 2H, *J* = 6.8 Hz, ~ CH_2-C*H*$_2$-Br), 2.73 (t, 2H, *J* = 6.8 Hz, C(O)C*H*$_2$~), 1.93 (p, 2H, *J* = 7.2 Hz, ~ C*H*$_2$-CH_2-Br), 1.76 (p, 2H, *J* = 7.6 Hz, C(O)CH_2C*H*$_2$~), 1.54 (p, 2H, *J* = 7.6 Hz, ~ CH_2-C*H*$_2$-CH_2~).

^{13}CNMR (75 MHz, $CDCl_3$): δ 204.16, 79.03, 72.18, 69.75, 69.29, 39.38, 33.75, 32.68, 28.07, 23.58.

$FcCO(CH_2)_6Br$ (72.6%, $R_f = 0.42$)

^{1}H NMR (400 MHz, $CDCl_3$): δ 4.79 (t, 2H, J = 2.0 Hz, H_{Fc} *ortho* to C(O)CH_2 ~), 4.50 (t, 2H, J = 2 Hz, H_{Fc} *meta* to C(O)CH_2), 4.20 (s, 5H, H_{Fc}), 3.43 (t, 2H, J = 6.8 Hz, ~CH_2-CH_2-Br), 2.71 (t, 2H, J = 7.2 Hz, C(O)CH_2~), 1.90 (p, 2H, J = 7.2 Hz, ~CH_2-CH_2-Br), 1.73 (p, 2H, J = 7.2 Hz, C(O)CH_2CH_2~), 1.57-1.39 (m, 4H, J = 7.6 Hz, ~CH_2-(CH_2)$_2$-CH_2~).

^{13}C-NMR (75 MHz, $CDCl_3$): δ 204.34, 79.14, 72.14, 69.75, 69.32, 39.49, 33.93, 32.61, 28.61, 28.04, 24.28.

$FcCO(CH_2)_8Br$ (74.7%, Hex:EtOAc, 9:1 (v:v), $R_f = 0.25$)

^{1}H NMR (400 MHz, $CDCl_3$): δ 4.78 (t, 2H, J = 2.4 Hz, H_{Fc} *ortho* to C(O)CH_2 ~), 4.50 (t, 2H, J = 2 Hz, H_{Fc} *meta* to C(O)CH_2), 4.20 (s, 5H, H_{Fc}), 3.42 (t, 2H, J = 6.8 Hz, ~CH_2-CH_2-Br), 2.70 (t, 2H, J = 6.8 Hz, C(O)CH_2~), 1.87 (p, 2H, J = 7.2 Hz, ~CH_2-CH_2-Br), 1.71 (m, 2H, J = 6.8 Hz, C(O)CH_2CH_2~), 1.50-1.29 (m, 8H, ~CH_2-(CH_2)$_4$-CH_2~).

^{13}C NMR (125 MHz, $CDCl_3$): δ 204.57, 79.20, 72.10, 69.74, 69.33, 39.71, 34.03, 32.80, 29.44, 28.65, 28.14, 24.55.

$FcCO(CH_2)_9Br$ (54.9%, $R_f = 0.61$)

^{1}H NMR (300 MHz, $CDCl_3$): δ 4.78 (t, 2H, J = 2.0 Hz, H_{Fc} *ortho* to C(O)CH_2~), 4.49 (t, 2H, J = 2 Hz, H_{Fc} *meta* to C(O)CH_2), 4.20 (s, 5H, H_{Fc}), 3.41 (t, 2H, J = 6.8 Hz, ~CH_2-CH_2-Br), 2.70 (t, 2H, J = 7.2 Hz, C(O)CH_2~), 1.86 (p, 2H, J = 7.2 Hz, ~CH_2-CH_2-Br), 1.71 (p, 2H, J = 6.8 Hz, C(O)CH_2CH_2~), 1.48-1.27 (m, 10H, ~CH_2-(CH_2)$_5$-CH_2~).

^{13}C-NMR (75 MHz, $CDCl_3$): δ204.77, 79.12, 72.12, 69.72, 69.33, 39.71, 34.06, 32.87, 29.47, 29.38, 29.28, 28.70, 28.13, 24.58.

$FcCO(CH_2)_{10}Br$ (70.8%, $R_f = 0.58$)

^1H NMR (300 MHz, $CDCl_3$): δ 4.79 (t, 2H, J = 1.6 Hz, H_{Fc} *ortho* to $C(O)CH_2$~), 4.49 (t, 2H, J = 2 Hz, H_{Fc} *meta* to $C(O)CH_2$), 4.20 (s, 5H, H_{Fc}), 3.41 (t, 2H, J = 6.4 Hz, ~CH_2-CH_2-Br), 2.70 (t, 2H, J = 7.2 Hz, C(O)CH_2~), 1.86 (p, 2H, J = 7.2 Hz, ~CH_2-CH_2-Br), 1.71 (p, 2H, J = 6.8 Hz, C(O)CH_2CH_2~), 1.55-1.25 (m, 12H, ~CH_2-(CH_2)$_6$-CH_2~).

^{13}C NMR (75 MHz, $CDCl_3$): δ 204.84, 79.47, 72.31, 69.93, 69.58, 39.99, 34.28, 33.07, 29.99, 29.77, 29.71, 29.63, 28.98, 28.40, 24.86.

$FcCO(CH_2)_{11}Br$ (54.9%, R_f =0.48)

^1H NMR (300 MHz, $CDCl_3$): δ 4.78 (t, 2H, J = 1.8 Hz, H_{Fc} *ortho* to $C(O)CH_2$~), 4.49 (t, 2H, J = 2.1 Hz, H_{Fc} *meta* to $C(O)CH_2$), 4.20 (s, 5H, H_{Fc}), 3.41 (t, 2H, J = 7.2 Hz, ~CH_2-CH_2-Br), 2.70 (t, 2H, J = 7.2 Hz, C(O)CH_2~), 1.86 (p, 2H, J = 6.9 Hz, ~CH_2-CH_2-Br), 1.71 (p, 2H, J = 7.2 Hz, C(O)CH_2CH_2~), 1.45-1.25 (m, 14H, ~ CH_2-(CH_2)$_7$-CH_2~).

^{13}C NMR (75 MHz, $CDCl_3$): δ 204.97, 79.40, 72.30, 69.94, 69.55, 39.97, 34.29, 33.04, 29.75, 29.70, 29.67, 29.62, 28.96, 28.37, 24.84.

$FcCO(CH_2)_{12}Br$ (45.1%, $R_f = 0.64$)

^1H NMR (500 MHz, $CDCl_3$): δ 4.80 (t, 2H, J = 2.0 Hz, H_{Fc} *ortho* to $C(O)CH_2$~), 4.50 (t, 2H, J = 2.0 Hz, H_{Fc} *meta* to $C(O)CH_2$), 4.21 (s, 5H, H_{Fc}), 3.42 (t, 2H, J = 7.0 Hz, ~CH_2-CH_2-Br), 2.71 (t, 2H, J = 7.5 Hz, C(O)CH_2~), 1.87 (p, 2H, J = 7.5 Hz, ~CH_2-CH_2-Br), 1.72 (p, 2H, J = 7.5 Hz, C(O)CH_2CH_2~), 1.48-1.27 (m, 16H, ~CH_2-(CH_2)$_8$-CH_2~).

^{13}C NMR (125 MHz, $CDCl_3$): δ 204.70, 79.23, 72.08, 69.73, 69.34, 39.78, 34.08, 32.85, 29.57, 29.53, 29.51, 29.43, 28.77, 28.19, 24.66.

$FcCO(CH_2)_{13}Br$ (60.7%, $R_f = 0.69$)

^1H NMR (400 MHz, $CDCl_3$): δ 4.78 (t, 2H, J = 2.0 Hz, H_{Fc} *ortho* to $C(O)CH_2$~), 4.49 (t, 2H, J = 2.0 Hz, H_{Fc} *meta* to $C(O)CH_2$), 4.20 (s, 5H, H_{Fc}), 3.41 (t, 2H, J = 6.8 Hz, ~CH_2-CH_2-Br),

2.70 (t, 2H, J = 7.2 Hz, C(O)CH_2~), 1.86 (p, 2H, J = 6.8 Hz, ~CH_2-CH_2-Br), 1.71 (p, 2H, J = 7.2 Hz, C(O)CH_2CH_2~), 1.46-1.25 (m, 18H, ~CH_2-(CH_2)$_9$-CH_2~).

^{13}C-NMR (125 MHz, $CDCl_3$): δ 204.68, 79.23, 72.08, 69.73, 69.34, 39.78, 34.09, 32.85, 29.58, 29.53, 29.51, 29.43, 28.77, 28.19, 24.66.

$FcCO(CH_2)_{14}Br$ (58.9%, Hex:EtOAc, 9:1 (v:v), R_f = 0.37)

^{1}H NMR (400 MHz, $CDCl_3$): δ 4.79 (t, 2H, J = 1.6 Hz, H_{Fc} *ortho* to C(O)CH_2 ~), 4.49 (t, 2H, J = 2.0 Hz, H_{Fc} *meta* to C(O)CH_2), 4.20 (s, 5H, H_{Fc}), 3.41 (t, 2H, J = 6.8 Hz, ~CH_2-CH_2-Br), 2.70 (t, 2H, J = 7.6 Hz, C(O)CH_2~), 1.86 (p, 2H, J = 7.2 Hz, ~CH_2-CH_2-Br), 1.71 (p, 2H, J = 7.2 Hz, C(O)CH_2CH_2~), 1.49-1.25 (m, 20H, ~CH_2-(CH_2)$_{10}$-CH_2~).

^{13}C NMR (125 MHz, $CDCl_3$): δ 204.55, 79.21,72.08, 69.73, 69.34, 39.79, 34.09, 32.86, 29.64, 29.61, 29.59, 29.54, 29.45, 28.78, 28.19, 24.67.

$FcCO(CH_2)_{15}Br$ (58.7%, Hex:EtOAc, 9:1 (v:v), R_f = 0.44)

^{1}H NMR (300 MHz, $CDCl_3$): δ 4.78 (t, 2H, J = 1.8 Hz, H_{Fc} *ortho* to C(O)CH_2~), 4.49 (t, 2H, J = 1.8 Hz, H_{Fc} *meta* to C(O)CH_2), 4.20 (s, 5H, H_{Fc}), 3.41 (t, 2H, J = 6.9 Hz, ~CH_2-CH_2-Br), 2.70 (t, 2H, J = 7.2 Hz, C(O)CH_2~), 1.86 (p, 2H, J = 7.2 Hz, ~CH_2-CH_2-Br), 1.71 (p, 2H, J = 6.9 Hz, C(O)CH_2CH_2~), 1.49-1.24 (m, 22H, ~ CH_2-(CH_2)$_{11}$-CH_2~).

^{13}C NMR (125 MHz, $CDCl_3$): δ 204.74, 79.24, 72.09, 69.74, 69.35, 39.81, 34.11, 32.86, 29.65, 29.62, 29.59, 29.55, 29.45, 28.79, 28.20, 24.67.

Synthesis of ω-bromoalkylferrocene ($Fc(CH_2)_nBr$) (**3**)[8]

ω-Bromoalkanoylferrocene ($FcCO(CH_2)_{n-1}Br$, n = 6, 7, 9-16) (1 eq.) was dissolved in dry dichloromethane ([Fc] ≈ 0.15 M) under an inert atmosphere. $TiCl_4$ (1 eq.) was added drop wise, followed by the drop wise addition of Et_3SiH (4 eq.). The deep blue reaction mixture was stirred at room temperature for 48 h, and then quenched by the addition of 5% (w/v)

Na_2CO_3. The formed grey precipitate was separated by filtration and the filtrate (orange-red) was transferred into a separatory funnel. The organic phase (bottom layer) was separated, and the aqueous one was extracted several times with dichloromethane (until the organic phase was colorless). The combined organic layers were dried over $MgSO_4$ and concentrated by rotary evaporation. The residue was purified by flash chromatography over silica gel using various mixtures of ethyl acetate: hexanes.

Fc(CH₂)₆Br (41.3%, Hex:EtOAc, 24:1 (v:v), $R_f = 0.71$)

^{1}H NMR (400 MHz, $CDCl_3$): δ 4.11 (s, 5H, H_{Fc}), 4.04 (m, 4H, H_{Fc} *ortho* to ~CH_2-CH_2 and H_{Fc} *meta* to ~CH_2-CH_2~) (unresolved signal), 3.42 (t, 2H, J = 7.2 Hz, ~CH_2-CH_2-Br), 2.33 (t, 2H, J = 8.0 Hz, F_c-CH_2~), 1.87 (p, 2H, J = 7.2 Hz, ~CH_2-CH_2-Br), 1.54-1.30 (m, 6H, F_c-CH_2-(CH_2)$_3$~).

Fc(CH₂)₇Br (63.9%, Hex:EtOAc, 24:1 (v:v), $R_f = 0.66$)

^{1}H NMR (400 MHz, $CDCl_3$): δ 4.12 (s, 5H, H_{Fc}), 4.09 (d, 2H, J = 1.6 Hz, H_{Fc} *ortho* to ~CH_2-CH_2~), 4.07 (d, 2H, J = 2 Hz, H_{Fc} *meta* to ~CH_2-CH_2~), 3.42 (t, 2H, J = 6.8 Hz, ~CH_2-CH_2-Br), 2.32 (t, 2H, J = 7.6 Hz, F_c-CH_2~), 1.86 (p, 2H, J = 7.2Hz, ~CH_2-CH_2-Br), 1.55-1.28 (m, 8H, F_c-CH_2 (CH_2)$_4$~).

^{13}C NMR (125 MHz, $CDCl_3$): δ 89.40, 68.48, 68.07, 67.04, 34.03, 32.82, 31.04, 29.57, 29.41, 28.66, 28.14.

Fc(CH₂)₉Br (53.2%, Hex:EtOAc, 24:1 (v:v), $R_f = 0.80$)

^{1}H NMR (400 MHz, $CDCl_3$): δ 4.11 (s, 5H, H_{Fc}), 4.06 (d, 2H, J = 1.2 Hz, H_{Fc} *ortho* to ~CH_2-CH_2~), 4.04 (d, 2H, J = 1.6 Hz, H_{Fc} *meta* to ~CH_2-CH_2~), 3.42 (t, 2H, J = 7.2 Hz, ~CH_2-CH_2-Br), 2.32 (t, 2H, J = 8.0 Hz, F_c-CH_2~), 1.86 (p, 2H, J = 8.0 Hz, ~CH_2-CH_2-Br), 1.5-1.2 (m, 12H, F_c-CH_2 (CH_2)$_6$~).

^{13}C NMR (125 MHz, $CDCl_3$): δ 89.53, 68.47, 68.07, 67.01, 34.06, 32.84, 31.12, 29.60, 29.41, 28.77, 28.18.

$Fc(CH_2)_{10}Br$ (36.0%, Hex:EtOAc, 24:1 (v:v), $R_f = 0.70$)

^1H NMR (300 MHz, $CDCl_3$): δ 4.11 (s, 5H, H_{Fc}), 4.08-4.06 (m, 4H, H_{Fc} *ortho* and *meta* to ~CH_2-CH_2~), 3.42 (t, 2H, *J* = 6.4 Hz, ~CH_2-C*H*$_2$-Br), 2.30 (t, 2H, *J* = 7.6 Hz, F_c-C*H*$_2$~), 1.86 (p, 2H, *J* = 7.6 Hz, ~C*H*$_2$-CH_2-Br), 1.55-1.23 (m, 14H, F_c-CH_2 (C*H*$_2$)$_7$ ~).

^{13}C NMR (125 MHz, $CDCl_3$): δ 89.75, 68.62, 68.19, 67.12, 34.08, 32.85, 31.11, 29.64, 29.59, 29.51, 29.49, 29.44, 28.78, 28.19.

$Fc(CH_2)_{11}Br$ (49.5%, Hex:EtOAc, 24:1 (v:v), $R_f = 0.79$)

^1H NMR (300 MHz, $CDCl_3$): δ 4.09 (s, 5H, H_{Fc}), 4.06 (s, 2H, H_{Fc} *ortho* to ~CH_2-CH_2 ~), 4.05-4.02 (m, 4H, H_{Fc} *ortho* and *meta* to ~CH_2-CH_2 ~) (unresolved), 3.42 (t, 2H, *J* = 6.4 Hz ~CH_2-C*H*$_2$-Br), 2.32 (t, 2H, *J* = 7.6 Hz, F_c-C*H*$_2$~), 1.86 (p, 2H, *J* = 6.8 Hz, ~C*H*$_2$-CH_2-Br), 1.54-1.25 (m, 16H, F_c-CH_2(C*H*$_2$)$_8$~).

^{13}C NMR ($CDCl_3$, 125 MHz): δ 90.02, 68.92, 68.39, 67.32, 34.30, 32.98, 31.21, 29.88, 29.81, 29.77, 29.64, 29.01, 28.42.

$Fc(CH_2)_{12}Br$ (44.0%, Hex:EtOAc, 24:1 (v:v), $R_f = 0.68$)

^1H NMR ($CDCl_3$, 400 MHz): δ 4.11 (s, 5H, H_{Fc}), 4.07 (s, 2H, H_{Fc} *ortho* to ~CH_2-CH_2~), 4.05 (s, 2H, H_{Fc} *meta* to ~CH_2-CH_2 ~), 3.42 (t, 2H, *J* = 6.4 Hz, ~CH_2-C*H*$_2$-Br), 2.30 (t, 2H, *J* = 6.4 Hz, F_c-C*H*$_2$~), 1.86 (p, 2H, *J* = 7.6 Hz, ~C*H*$_2$-CH_2-Br), 1.86 (m, 2H, F_c-CH_2-C*H*$_2$~), 1.5-1.2 (m, 18H, F_c-CH_2(C*H*$_2$)$_9$~).

^{13}C NMR ($CDCl_3$, 75 MHz): δ 90.12, 68.92, 68.47, 67.40, 34.32, 33.04, 31.31, 29.86, 29.81, 29.78, 29.74, 29.64, 28.97, 28.38.

$Fc(CH_2)_{13}Br$ (73.4%, Hex:EtOAc, 24:1 (v:v), $R_f = 0.77$)

^{1}H NMR (500 MHz, $CDCl_3$): δ 4.16 (s, 5H, H_{Fc}), 4.15- 4.02 (m, 4H, H_{Fc} *ortho* and *meta* to ~CH_2-CH_2~) (unresolved), 3.44 (t, 2H, *J* = 7.0 Hz, ~CH_2-C*H*$_2$-Br), 2.30 (t, 2H, *J* = 7.0 Hz, F_c-C*H*$_2$~), 1.88 (p, 2H, *J* = 6.5 Hz, ~C*H*$_2$-CH_2-Br), 1.55-1.24(m, 20H, F_c-CH_2(C*H*$_2$)$_{10}$~).

^{13}C NMR (125 MHz, $CDCl_3$): δ 90.27, 69.11, 68.60, 67.53, 34.09, 32.86, 31.60, 31.08, 29.68, 29.65, 29.63, 29.59, 29.55, 29.45, 28.79, 28.20.

Fc(CH$_2$)$_{14}$Br (63.1%, Hex:EtOAc, 9:1 (v:v), R_f = 0.91)

^{1}H NMR (400 MHz, $CDCl_3$): δ 4.09 (s, 5H, H_{Fc}), 4.05 (d, 2H, *J* = 2.0 Hz, H_{Fc} *ortho* to ~CH_2-CH_2~), 4.04 (d, 2H, *J* = 1.6 Hz, H_{Fc} *meta* to ~CH_2-CH_2~), 3.41 (t, 2H, *J* = 6.8 Hz, ~CH_2-C*H*$_2$-Br), 2.31 (t, 2H, *J* = 7.2 Hz, F_c-C*H*$_2$~), 1.86 (p, 2H, *J* = 7.6 Hz, ~C*H*$_2$-CH_2-Br), 1.56-1.22 (m, 22H, F_c-CH_2(C*H*$_2$)$_{11}$~).

^{13}C NMR (125 MHz, $CDCl_3$): δ 89.71, 68.54, 68.16, 67.07, 34.10, 32.82, 31.13, 29.69, 29.67, 29.66, 29.64, 29.59, 29.56, 29.46, 28.79, 28.20.

Fc(CH$_2$)$_{15}$Br (49.1%, Hex:EtOAc, 24:1 (v:v), R_f = 0.75)

^{1}H NMR (400 MHz, $CDCl_3$): δ 4.14 (s, 5H, H_{Fc}), 4.11-4.02 (m, 4H, H_{Fc} *ortho* and *meta* to ~CH_2-CH_2~) (unresolved), 3.41 (t, 2H, *J* = 6.8 Hz, ~CH_2-C*H*$_2$-Br), 2.28 (t, 2H, *J* = 7.6 Hz, F_c-C*H*$_2$~), 1.86 (p, 2H, *J* = 7.2 Hz, ~C*H*$_2$-CH_2-Br), 1.52-1.22 (m, 24H, F_c-CH_2(C*H*$_2$)$_{12}$~).

^{13}C NMR (125 MHz, $CDCl_3$): δ 89.89, 68.65, 68.22, 67.14, 34.08, 32.86, 31.12, 29.68, 29.66, 29.63, 29.59, 29.56, 29.46, 28.79, 28.20.

Fc(CH$_2$)$_{16}$Br (43.7%, Hex:EtOAc, 24:1 (v:v), R_f = 0.78)

^{1}H NMR (500 MHz, $CDCl_3$): δ 4.12 (s, 5H, H_{Fc}), 4.10- 4.04 (m, 4H, H_{Fc} *ortho* and *meta* to ~CH_2-CH_2~) (unresolved), 3.42 (t, 2H, *J* = 7.0 Hz, ~CH_2-C*H*$_2$-Br), 2.31 (t, 2H, *J* = 7.5 Hz, F_c-C*H*$_2$~), 1.86 (p, 2H, *J* = 7.0 Hz, ~C*H*$_2$-CH_2-Br), 1.56-1.21 (m, 26H, F_c-CH_2(C*H*$_2$)$_{13}$~).

^{13}C NMR (125 MHz, $CDCl_3$): δ 89.79, 68.58, 68.16, 67.08, 34.10, 32.86, 31.13, 29.69, 29.67, 29.66, 29.64, 29.59, 29.56, 29.46, 28.79, 28.20.

Synthesis of ω-ferrocenylalkylisothiuronium bromide (Fc(CH$_2$)$_m$SC(=NH$_2$)NH$_2$Br) (**4**)

ω-Bromoalkylferrocene (Fc(CH$_2$)$_n$Br, n=6,7,9-16) (0.17 M, 1 eq.) and thiourea (0.4 M, 2.3 eq.) were dissolved in ethanol. The reaction mixture was degassed and then heated at reflux for 6 h. The solvent was removed under reduced pressure and the crude material was purified by column chromatography over silica gel, first eluted with dichloromethane (in order to remove the unreacted starting material) followed, usually, by a 4:1 (v:v) mixture of dichloromethane:methanol.

Fc(CH$_2$)$_6$SC(=NH$_2$)NH$_2$Br (100.0%, CH_2Cl_2: MeOH, 17:3 (v:v), R_f = 0.70)

^{1}H NMR (300 MHz, CD_3OD): δ 4.06 (s, 5H, H_{Fc}), 4.04 (d, 2H, *J* = 1.6 Hz, H_{Fc} *ortho* to ~CH$_2$-CH$_2$~), 4.01 (d, 2H, *J* = 1.6 Hz, H_{Fc} *meta* to ~CH$_2$-CH$_2$~), 3.13 (t, 2H, *J* = 6.8 Hz, ~CH$_2$-C*H*$_2$-S-C(=NH$_2$)NH$_2$Br), 2.34 (t, 2H, *J* = 7.2 Hz, F$_c$-C*H*$_2$~), 1.70 (p, 2H, *J* = 8.0 Hz, ~C*H*$_2$-CH$_2$-S-C(=NH$_2$)NH$_2$Br), 1.56-1.32 (m, 6H, F$_c$-CH$_2$(C*H*$_2$)$_3$).

^{13}C NMR (75 MHz, CD_3OD): δ 171.46, 90.21, 69.38, 69.06, 68.05, 32.09, 31.85, 30.48, 29.88, 29.60, 29.28.

Fc(CH$_2$)$_7$SC(=NH$_2$)NH$_2$Br (100%, CH_2Cl_2: MeOH, 4:1 (v:v), R_f = 0.67)

^{1}H NMR (400 MHz, $CDCl_3$): δ 4.05 (s, 5H, H_{Fc}), 4.04 (d, 2H, *J* = 1.6 Hz, H_{Fc} *ortho* to ~CH$_2$-CH$_2$ ~), 4.01 (d, 2H, *J* = 1.6 Hz, H_{Fc} *meta* to ~CH$_2$-CH$_2$~), 3.13 (t, 2H, *J* = 7.6 Hz, ~CH$_2$-C*H*$_2$-S-C(=NH$_2$)NH$_2$Br), 2.34 (t, 2H, *J* = 7.2 Hz, F$_c$-C*H*$_2$~), 1.70 (p, 2H, *J* = 7.6 Hz, ~C*H*$_2$-CH$_2$-S-C(=NH$_2$)NH$_2$Br), 1.54-1.30 (m, 8H, F$_c$-CH$_2$(C*H*$_2$)$_4$).

^{13}C NMR (125 MHz, $CDCl_3$): δ 171.72, 88.97, 68.01, 67.68, 66.65, 30.82, 30.51, 29.21, 28.97, 28.56, 28.24, 28.02.

$Fc(CH_2)_9SC(=NH_2)NH_2Br$ (97.8%, CH_2Cl_2: MeOH, 4:1 (v:v), $R_f = 0.70$)

^1H NMR (500 MHz, $CDCl_3$, 10% CD_3OD) : δ 4.02 (s, 5H, H_{Fc}), 3.98 (d, 2H, J = 1.5 Hz, H_{Fc} *ortho* to ~CH_2-CH_2~), 3.97 (d, 2H, J = 2 Hz, H_{Fc} *meta* to ~CH_2-CH_2~), 3.03 (t, 2H, J = 8.0 Hz, ~CH_2-C*H*$_2$-S-C(=NH_2)NH_2Br), 2.25 (t, 2H, J = 8 Hz, F_c-C*H*$_2$~), 1.64 (p, 2H, J = 7.5 Hz, ~C*H*$_2$-CH_2-Br), 1.47-1.32 (m, 4H, F_c-CH_2-C*H*$_2$~ and~C*H*$_2$-CH_2-S-C(=NH_2)NH_2Br), 1.29 (s(broad), 8H, ~CH_2-(C*H*$_2$)$_4$-CH_2~).

^{13}C NMR (125 MHz, $CDCl_3$): δ 171.38, 89.33, 68.30, 67.90, 66.86, 66.84, 30.98, 30.96, 30.93, 29.42, 29.41, 29.33, 29.26, 29.20, 29.12, 28.85, 28.83, 28.34, 28.07.

$Fc(CH_2)_{10}SC(=NH_2)NH_2Br$ (91.5%, CH_2Cl_2: MeOH, 4:1 (v:v), $R_f = 0.62$)

^1H NMR (300 MHz, CD_3OD): δ 4.06 (s, 5H, H_{Fc}), 4.02 (d, 2H, J = 1.5 Hz, H_{Fc} *ortho* to ~CH_2-CH_2~), 4.01 (d, 2H, J = 1.8 Hz, H_{Fc} *meta* to ~CH_2-CH_2~), 3.13 (t, 2H, J = 7.2 Hz, ~CH_2-C*H*$_2$-S-C(=NH_2)NH_2Br), 2.32 (t, 2H, J = 7.5 Hz, F_c-C*H*$_2$~), 1.70 (p, 2H, J = 7.5 Hz, ~C*H*$_2$-CH_2-S-C(=NH_2)NH_2Br), 1.55-1.23 (m, 14H, F_c-CH_2(C*H*$_2$)$_{12}$~).

$Fc(CH_2)_{11}SC(=NH_2)NH_2Br$ (71.9%, CH_2Cl_2: MeOH, 4:1 (v:v), $R_f = 0.59$)

^1H NMR (300 MHz, $CDCl_3$): δ 4.08 (s, 5H, H_{Fc}), 4.05 (d, 2H, J = 1.6 Hz, H_{Fc} *ortho* to ~CH_2-CH_2~), 4.03 (d, 2H, J = 1.6 Hz, H_{Fc} *meta* to ~CH_2-CH_2~), 3.19 (t, 2H, J = 7.6 Hz, ~CH_2-C*H*$_2$-S-C(=NH_2)NH_2Br), 2.30 (t, 2H, J = 7.6 Hz, F_c-C*H*$_2$~), 1.71 (p, 2H, J = 7.2 Hz, ~C*H*$_2$-CH_2-S-C(=NH_2)NH_2Br), 1.47-1.32 (m, 4H, F_c-CH_2-C*H*$_2$~ and ~C*H*$_2$-CH_2-S-C(=NH_2)NH_2Br), 1.27 (s(broad), 12H, ~CH_2-(C*H*$_2$)$_6$-CH_2~).

$Fc(CH_2)_{12}SC(=NH_2)NH_2Br$ (92.8%, CH_2Cl_2: MeOH, 4:1 (v:v), $R_f = 0.56$)

^1H NMR (400 MHz, CD_3OD): δ 4.06 (s, 5H, H_{Fc}), 4.03 (d, 2H, J = 1.2 Hz,H_{Fc} *ortho* to ~CH_2-CH_2~), 4.01 (d, 2H, J = 1.2 Hz, H_{Fc}*meta* to ~CH_2-CH_2~), 3.13 (t, 2H, J = 7.6 Hz, ~CH_2-C*H*$_2$-S-C(=NH_2)NH_2Br), 2.32 (t, 2H, J = 7.6 Hz, F_c-C*H*$_2$~), 1.70 (p, 2H, J = 7.6 Hz, ~C*H*$_2$-CH_2-S-C(=NH_2)NH_2Br), 1.56-1.28 (m, 18H, F_c-CH_2(C*H*$_2$)$_9$ ~).

^{13}C NMR (75 MHz, CD_3OD): δ 171.40, 90.48, 69.37, 69.04, 68.00, 32.30, 31.89, 30.68, 30.62, 30.52, 30.09, 29.64, 29.45.

$Fc(CH_2)_{15}SC(=NH_2)NH_2Br$ (95.8%, CH_2Cl_2: MeOH, 4:1 (v:v), R_f = 0.73)

^{1}H NMR (500 MHz, $CDCl_3$, 20% CD_3OD): δ 4.12 (s, 5H, H_{Fc}), 4.10-4.02 (s(broad) 4H, H_{Fc} *ortho* and *meta* to ~CH_2-CH_2~) (unresolved), 3.03 (t, 2H, *J* = 7.5 Hz, ~CH_2-C*H*$_2$-S-C(=NH_2)NH_2Br), 2.20 (t, 2H, *J* = 7.0 Hz, F_c-C*H*$_2$~), 1.65 (p, 2H, *J* = 7.5 Hz, ~C*H*$_2$-CH_2-S-C(=NH_2)NH_2Br), 1.47-1.18 (m, 24H, F_c-CH_2(C*H*$_2$)$_{12}$ ~).

^{13}C NMR (125 MHz, $CDCl_3$, 20% CD_3OD) : δ 171.34, 88.40, 69.04, 68.44, 67.47, 30.95, 30.85, 29.60, 29.58, 29.56, 29.54, 29.47, 29.42, 29.32, 28.93, 28.41, 28.16.

$Fc(CH_2)_{16}SC(=NH_2)NH_2Br$ (100%, CH_2Cl_2: MeOH, 4:1 (v:v), R_f = 0.61)

^{1}H NMR (400 MHz, CD_3OD): δ 4.06 (s, 5H, H_{Fc}), 4.03(d, 2H, *J* = 2.0 Hz, H_{Fc} *ortho* to ~CH_2-CH_2~), 4.01 (d, 2H, *J* = 1.6 Hz, H_{Fc} *meta* to ~CH_2-CH_2~), 3.12 (t, 2H, *J* = 7.2 Hz, ~CH_2-C*H*$_2$-S-C(=NH_2)NH_2Br), 2.32 (t, 2H, *J* = 7.2 Hz, F_c-C*H*$_2$~), 1.70 (p, 2H, *J* = 7.6 Hz, ~C*H*$_2$-CH_2-S-C(=NH_2)NH_2Br), 1.55-1.25 (m, 26H, F_c-CH_2(C*H*$_2$)$_{13}$ ~).

Synthesis of ω-ferrocenylalkanethiols ($Fc(CH_2)_nSH$) (**5**)

The solution of *ω*-ferrocenylalkylisothiuronium bromide ($Fc(CH_2)_nSC(=NH_2)NH_2Br$, *n* = 6, 7, 9-16) (1 eq.), 0.16 M in dry methanol, was thoroughly degassed and then NaOH (2.2 eq.) was added as a solid. The reaction mixture was heated at reflux for 5 h, under a positive pressure of inert gas. After cooling at room temperature, the reaction mixture was diluted with water, acidified, followed by extraction with dichloromethane. The organic phase was dried over $CaCl_2$, filtrated and concentrated by rotary evaporation. The crude product was purified by flash chromatography over silica gel eluted with a mixture of hexanes:dichloromethane to give the desired product.

$Fc(CH_2)_6SH$ (42.6%, Hex:CH_2Cl_2, 9:1 (v:v), $R_f = 0.26$)

^1H NMR (300 MHz, $CDCl_3$): δ 4.09 (s, 5H, H_{Fc}), 4.05 (s(broad), 4H, H_{Fc} *ortho* to ~CH_2-CH_2~ and H_{Fc} *meta* to ~CH_2-CH_2~) (unresolved), 2.53 (q, 2H, J = 7.5 Hz, ~CH_2-C*H*$_2$-SH), 2.32 (t, 2H, J = 7.5 Hz, F_c-C*H*$_2$~), 1.67-1.30 (m, 9H, ~CH_2-(C*H*$_2$)$_4$-CH_2 and -S*H*).

^{13}C NMR (75 MHz, $CDCl_3$): δ (ppm) 89.42, 68.64, 68.23, 67.21, 34.18, 31.20, 29.71, 29.21, 28.44, 24.83.

ESI-HRMS *m/z* 302.0687 (calcd. average mass for $C_{16}H_{22}SFe$: 302.0792)

Mp: 17.9 ºC

$Fc(CH_2)_7SH$ (61.4%, Hex:CH_2Cl_2, 9:1 (v:v), $R_f = 0.50$)

^1H NMR (500 MHz, $CDCl_3$): δ 4.10 (s, 5H, H_{Fc}), 4.06 (d, 2H, J = 1.5 Hz, H_{Fc} *ortho* to ~CH_2-CH_2~), 4.04 (d, 2H, J = 1.5 Hz, H_{Fc} *meta* to ~CH_2-CH_2~), 2.53 (q, 2H, J = 7.5 Hz, ~CH_2-C*H*$_2$-SH), 2.32 (t, 2H, J = 8.0 Hz, F_c-C*H*$_2$~), 1.62 (p, 2H, J = 7.5 Hz, ~ C*H*$_2$-CH_2-SH), 1.50-1.26 (m, 9H, ~ CH_2-(C*H*$_2$)$_4$-CH_2 and -S*H*).

^{13}C NMR (125 MHz, $CDCl_3$): δ 89.43, 68.45, 68.05, 67.01, 34.03, 31.08, 29.58, 29.50, 28.97, 28.35, 24.66.

ESI-HRMS *m/z* 316.0930 (calcd. average mass for $C_{17}H_{24}SFe$: 316.0948)

Mp: 8.6 ºC

$Fc(CH_2)_8SH$ (Hex:CH_2Cl_2, 24:1 (v:v), $R_f = 0.22$)

^1H NMR (500 MHz, $CDCl_3$): δ 4.09 (s, 5H, H_{Fc}), 4.05 (d, 2H, J = 2.0 Hz, H_{Fc} *ortho* to ~CH_2-CH_2~), 4.03 (d, 2H, J = 1.5 Hz, H_{Fc} *meta* to ~CH_2-CH_2~), 2.53 (q, 2H, J = 7.0 Hz, ~ CH_2-C*H*$_2$-SH), 2.32 (t, 2H, J = 8.0 Hz, F_c-C*H*$_2$~), 1.62 (p, 2H, J = 7.0 Hz, ~C*H*$_2$-CH_2-SH), 1.50 (p, 2H, J = 7.0 Hz, F_c-CH_2-C*H*$_2$~), 1.43-1.26 (m, 8H, ~CH_2-(C*H*$_2$)$_4$-CH_2), 1.34 (t, 1H, J = 7.5 Hz, -S*H*).

^{13}C NMR (125 MHz, $CDCl_3$): δ 89.50, 68.44, 68.05, 66.98, 34.04, 31.11, 29.59, 29.57, 29.40, 29.05, 28.38, 24.67.

ESI-HRMS *m/z* 330.1089 (calcd. average mass for $C_{18}H_{26}SFe$: 330.1105)

Mp: 35.5 ºC

Fc(CH₂)₉SH (59.6 %, Hex:CH_2Cl_2, 9:1 (v:v), R_f = 0.52)

^{1}H NMR (400 MHz, $CDCl_3$): δ 4.10 (s, 5H, H_{Fc}), 4.06 (d, 2H, *J* = 1.2 Hz, H_{Fc} *ortho* to ~CH_2-CH_2~), 4.04 (d, 2H, J= 1.6 Hz, H_{Fc} *meta* to ~CH_2-CH_2~), 2.53 (q, 2H, *J* = 7.6 Hz, ~CH_2-C*H*$_2$-SH), 2.32 (t, 2H, *J* = 7.6 Hz, F_c-C*H*$_2$~), 1.61 (p, 2H, *J* = 7.6 Hz, ~C*H*$_2$-CH_2-SH), 1.50-1.26 (m, 12H, ~CH_2-(C*H*$_2$)$_6$-CH_2~), 1.34 (t, 1H, *J* = 7.6 Hz, -S*H*).

^{13}C NMR (125 MHz, $CDCl_3$): δ 89.99, 68.82, 68.39, 67.38, 34.05, 31.09, 29.62, 29.59, 29.49, 29.47, 29.08, 28.38, 24.67.

ESI-HRMS *m/z* 344.1256 (calcd. average mass for $C_{19}H_{28}SFe$: 344.1262)

Mp: 19.3 ºC

Fc(CH₂)₁₀SH (49.8%, Hex:CH_2Cl_2, 24:1 (v:v), R_f = 0.70)

^{1}H NMR (400 MHz, $CDCl_3$): δ 4.14 (s, 5H, H_{Fc}), 4.11- 4.09 (m, 4H, H_{Fc} *ortho* to ~CH_2-CH_2~ and H_{Fc} *meta* to ~CH_2-CH_2~) (unresolved), 2.53 (q, 2H, *J* = 7.6 Hz, ~CH_2-C*H*$_2$-SH), 2.28 (t, 2H, *J* = 7.6 Hz, F_c-C*H*$_2$~), 1.61 (p, 2H, *J* = 6.8 Hz, ~C*H*$_2$-CH_2-SH), 1.50-1.21 (m, 14H, ~CH_2-(C*H*$_2$)$_7$-CH_2~), 1.34 (t, 1H, *J* = 7.6 Hz, -S*H*).

^{13}C NMR (125 MHz, $CDCl_3$): δ 89.67, 68.55, 68.14, 67.06, 34.06, 31.12, 29.65, 29.59, 29.55, 29.51, 29.08, 28.39, 24.68.

ESI-HRMS *m/z* 358.1410 (calcd. average mass for $C_{20}H_{28}SFe$: 358.1419)

Mp: 43.7 ºC

Fc(CH₂)₁₁SH (66.2%, Hex:CH_2Cl_2, 9:1 (v:v), R_f = 0.59)

^{1}H NMR (300 MHz, $CDCl_3$): δ 4.10 (s, 5H, H_{Fc}), 4.06 (s, 2H, H_{Fc} *ortho* to ~CH_2-CH_2~) (unresolved), 4.04(d, 2H, *J* = 1.2 Hz, H_{Fc} *meta* to ~CH_2-CH_2~), 2.53 (q, 2H, *J* = 7.6 Hz, ~CH_2-C*H*$_2$-SH), 2.31 (t, 2H, *J* = 7.6 Hz, F_c-C*H*$_2$~), 1.61 (p, 2H, *J* = 7.6 Hz, ~C*H*$_2$-CH_2-SH), 1.50-1.25 (m, 16H, ~CH_2-(C*H*$_2$)$_8$-CH_2~), 1.34 (t, 1H, *J* = 8.0 Hz, -S*H*).

^{13}C NMR (75 MHz, $CDCl_3$): δ 89.80, 68.65, 68.26, 67.18, 34.30, 31.25, 29.88, 29.81, 29.80, 29.75, 29.74, 29.30, 28.61, 24.89.

ESI-HRMS *m/z* 372.1569 (calcd average mass for $C_{21}H_{30}SFe$: 372.1576)

Mp: 36.4 ºC

Fc(CH$_2$)$_{12}$SH (32.8%, Hex:CH_2Cl_2, 9:1 (v:v), R_f = 0.53)

^{1}H NMR (400 MHz, $CDCl_3$): δ 4.09 (s, 5H, H_{Fc}), 4.05 (d, 2H, *J* = 1.6 Hz, H_{Fc} *ortho* to ~CH_2-CH_2 ~), 4.03 (d, 2H, *J* = 1.6 Hz, H_{Fc} *meta* to ~CH_2-CH_2~), 2.53 (q, 2H, *J* = 6.8 Hz, ~CH_2-C*H*$_2$-SH), 2.31 (t, 2H, *J* = 7.2 Hz, F_c-C*H*$_2$~), 1.61 (p, 2H, *J* = 7.6 Hz, ~C*H*$_2$-CH_2-SH), 1.55-1.26 (m, 18H, ~ CH_2-(C*H*$_2$)$_9$-CH_2~), 1.34 (t, 1H, *J* = 8.0 Hz, -S*H*).

^{13}C NMR (75 MHz, $CDCl_3$): δ 90.75,69.43, 68.90, 67.83, 34.24, 31.23, 29.81, 29.77, 29.70, 29.26, 28.57, 24.86.

ESI-HRMS *m/z* 386.1726 (calcd. average mass for $C_{22}H_{32}SFe$: 386.1733)

Mp: 52.9 ºC

Fc(CH$_2$)$_{13}$SH (55.78%, Hex:CH_2Cl_2, 19:1 (v:v), R_f = 0.57)

^{1}H NMR (400 MHz, $CDCl_3$): δ 4.12 (s, 5H, H_{Fc}), 4.10 (s (broad), 2H, H_{Fc} *ortho* to ~CH_2-CH_2~) (unresolved), 4.07 (s(broad), 2H, H_{Fc}*meta* to ~CH_2-CH_2~)(unresolved), 2.53 (q, 2H, *J* = 7.2 Hz, ~CH_2-C*H*$_2$-SH), 2.30 (t, 2H, *J* = 7.2 Hz, F_c-C*H*$_2$~), 1.62 (p, 2H, *J* = 7.6 Hz, ~C*H*$_2$-CH_2-SH), 1.55-1.20 (m, 20H, ~ CH_2-(C*H*$_2$)$_{10}$-CH_2~), 1.34 (t, 1H, *J* = 8.0 Hz, -S*H*).

^{13}C NMR (125 MHz, $CDCl_3$): δ 89.78, 68.65, 68.22, 67.15, 34.08, 31.12, 29.69, 29.67, 29.65, 29.60, 29.56, 29.54, 29.10, 28.41, 24.68.

ESI-HRMS *m/z* 400.1884 (calcd. average mass for $C_{23}H_{34}SFe$: 400.1890)

Mp: 46.8 ºC

Fc(CH₂)₁₄SH (84.3%, Hex:CH_2Cl_2, 9:1 (v:v))

^{1}H NMR (300 MHz, $CDCl_3$): δ 4.09 (s, 5H, H_{Fc}), 4.05 (d, 2H, *J* = 1.6 Hz, H_{Fc} *ortho* to ~CH_2-CH_2~), 4.04 (d, 2H, *J* = 2.0 Hz, H_{Fc} *meta* to ~CH_2-CH_2~), 2.53 (q, 2H, *J* = 7.2 Hz, ~CH_2-C*H*$_2$-SH), 2.31 (t, 2H, *J* = 7.6 Hz, F_c-C*H*$_2$~), 1.61 (p, 2H, *J* = 7.6 Hz, ~C*H*$_2$-CH_2-SH), 1.54-1.22 (m, 22H, ~CH_2-(C*H*$_2$)$_{11}$-CH_2~), 1.34 (t, 1H, *J* = 7.6 Hz, -S*H*).

^{13}CNMR (100 MHz, $CDCl_3$): δ 89.61, 68.64, 68.23, 67.16, 34.27, 31.34, 29.88, 29.85, 29.82, 29.78, 29.76, 29.74, 29.30, 28.59, 24.89.

ESI-HRMS *m/z* 414.2035 (calcd. average mass for $C_{24}H_{36}SFe$: 414.2047)

Mp: 57.5 ºC

Fc(CH₂)₁₅SH (55.78%, Hex:CH_2Cl_2, 9:1 (v:v), R_f = 0.61)

^{1}H NMR (400 MHz, $CDCl_3$): δ 4.10 (s, 5H, H_{Fc}),4.07 (s (broad), 2H, H_{Fc} *ortho* to ~CH_2-CH_2 ~) (unresolved), 4.05 (s(broad), 2H, H_{Fc} *meta* to ~CH_2-CH_2 ~) (unresolved), 2.53 (q, 2H, *J* = 7.6 Hz, ~CH_2-C*H*$_2$-SH), 2.31 (t, 2H, *J* = 8.0 Hz, F_c-C*H*$_2$~), 1.61 (p, 2H, *J* = 7.2 Hz, ~C*H*$_2$-CH_2-SH), 1.54-1.22 (m, 24H, ~ CH_2-(C*H*$_2$)$_{12}$-CH_2~), 1.34 (t, 1H, *J* = 7.6 Hz, -S*H*).

^{13}C NMR (125 MHz, $CDCl_3$): δ 90.42, 69.13, 68.61, 67.55, 34.07, 31.08, 29.69, 29.66, 29.61, 29.59, 29.57, 29.54, 29.10, 28.40, 24.68.

ESI-HRMS *m/z* 428.2208 (calcd. average mass for $C_{25}H_{38}SFe$: 428.2204)

Mp: 52.5 ºC

Fc(CH₂)₁₆SH (45.24%, Hex:CH_2Cl_2, 9:1 (v:v), R_f = 0.62)

^{1}H NMR (300 MHz, $CDCl_3$) : δ 4.09 (s, 5H, H_{Fc}), 4.05 (d, 2H, *J* = 1.6 Hz, H_{Fc} *ortho* to ~CH_2-CH_2~), 4.04 (d, 2H, *J* = 1.6 Hz, H_{Fc} *meta* to ~CH_2-CH_2~), 2.52 (q, 2H, *J* = 7.6 Hz, ~CH_2-C*H*$_2$-

SH), 2.31 (t, 2H, J = 7.6 Hz, F_c-CH_2~), 1.61 (p, 2H, J = 7.6 Hz, ~CH_2-CH_2-SH), 1.54-1.22 (m, 26H, ~ CH_2-(CH_2)$_{13}$-CH_2~), 1.35 (t, 1H, J = 7.6 Hz, -SH).

^{13}C NMR (125 MHz, $CDCl_3$): δ 89.73, 68.58, 68.16, 67.08, 34.08, 31.13, 29.70, 29.66, 29.61, 29.59, 29.57, 29.54, 29.10, 28.40, 24.69.

ESI-HRMS *m/z* 442.2354 (calcd. average mass for $C_{26}H_{40}SFe$: 442.2361)

Mp: 64.4 ºC

Example of a ^{1}H NMR spectrum of FcC$_n$SH. Compound is FcC$_{11}$SH.

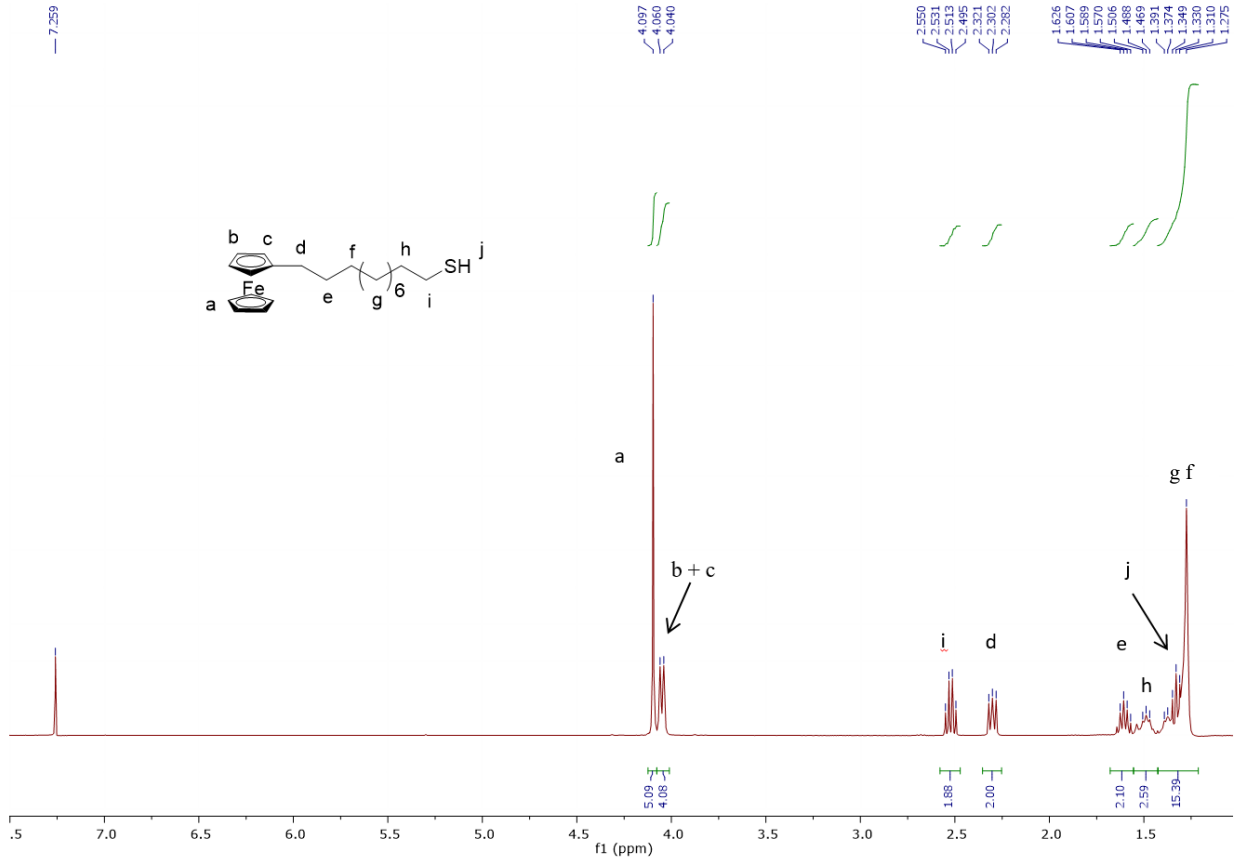

Example of a DSC thermogram. Compound is $FcC_{15}SH$.

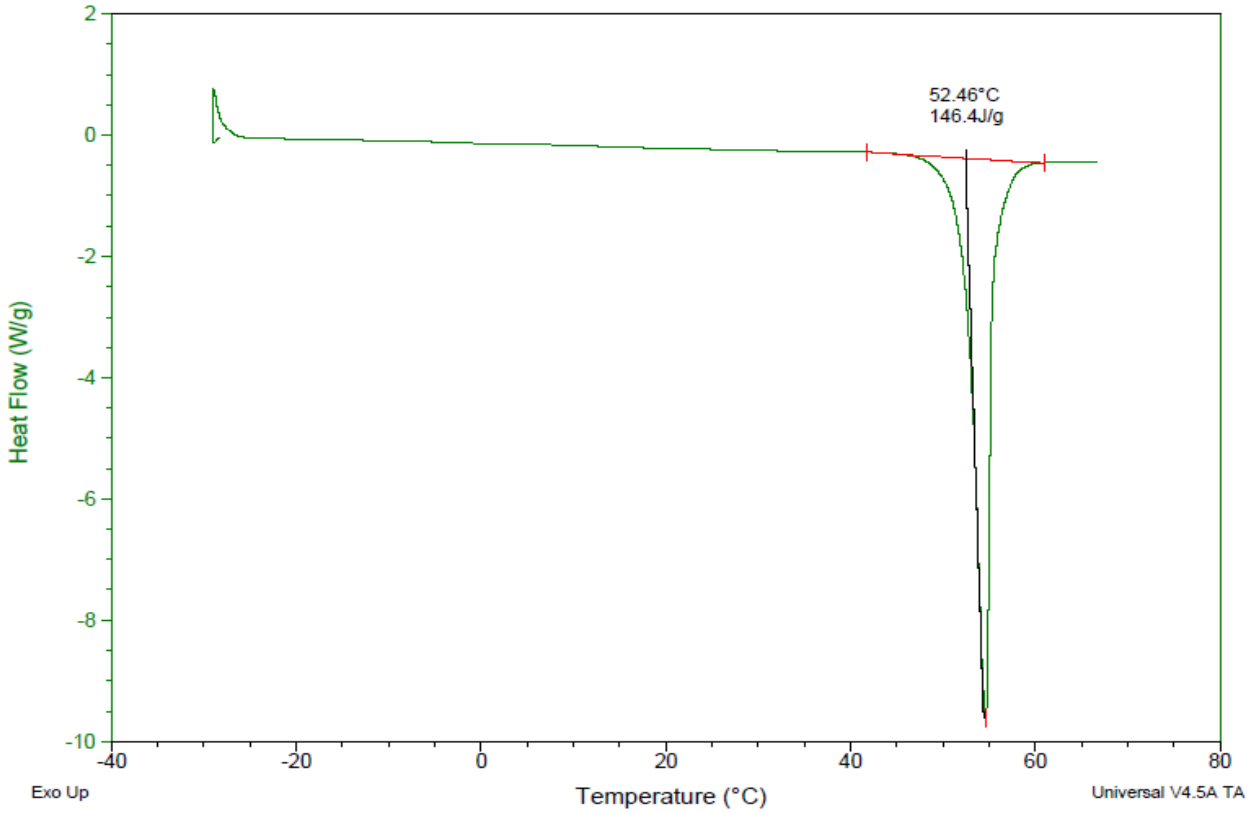

Table S1. CNLS fitting parameters and phase angles at 1 Hz ($\varphi_{1\ Hz}$) obtained by electrochemical impedance spectroscopy (EIS) at a working electrode potential of 0 V vs. Ag/AgCl in 0.1 M $NaClO_{4(aq)}$ on FcC_nSAu functionalized gold bead electrodes.

FcC_nSAu	R_s / Ω cm^2	CPE / μF cm^{-2}	α	$\varphi_{1\ Hz}$ / º
7	24 ± 1	2.020 ± 0.138	0.991 ± 0.003	89 ± 1
8	24 ± 5	1.851 ± 0.116	0.989 ± 0.005	89 ± 0
9	20 ± 2	1.731 ± 0.046	0.986 ± 0.004	89 ± 1
10	22 ± 2	1.624 ± 0.068	0.993 ± 0.018	89 ± 0
11	21 ± 2	1.482 ± 0.069	0.985 ± 0.006	89 ± 0
12	24 ± 2	1.480 ± 0.075	0.988 ± 0.006	89 ± 1
13	22 ± 3	1.377 ± 0.034	0.980 ± 0.006	88 ± 0
14	23 ± 4	1.392 ± 0.047	0.984 ± 0.005	88 ± 1
15	20 ± 3	1.245 ± 0.044	0.983 ± 0.004	89 ± 1
16	21 ± 2	1.258 ± 0.060	0.985 ± 0.013	89 ± 1

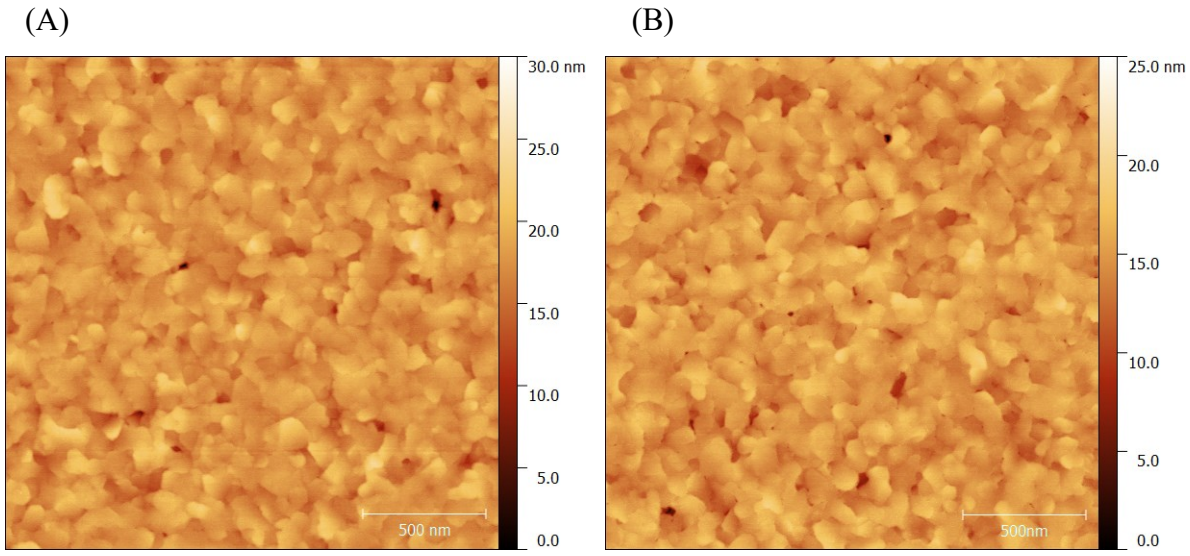

Figure S1. AFM height images (2 μm × 2 μm) of thermally evaporated Au on B270 glass. Substrates are from two different evaporation lots. Root mean square (rms) roughness: (A) 1.5 nm and (B) 1.4 nm.

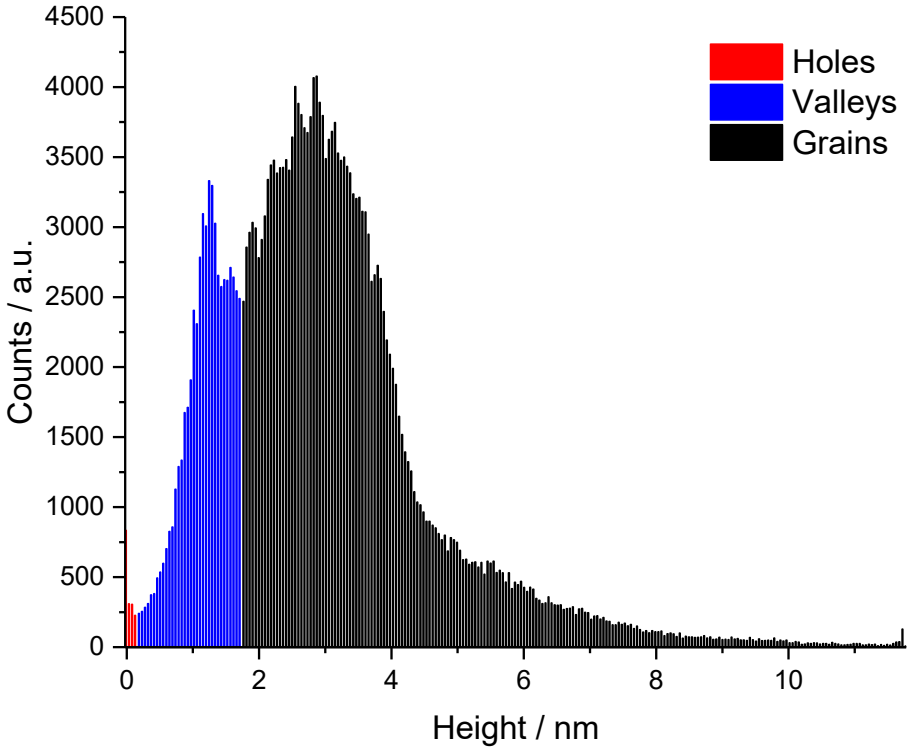

Figure S2. Height distributions of the surface features for the as-deposited gold thin films.

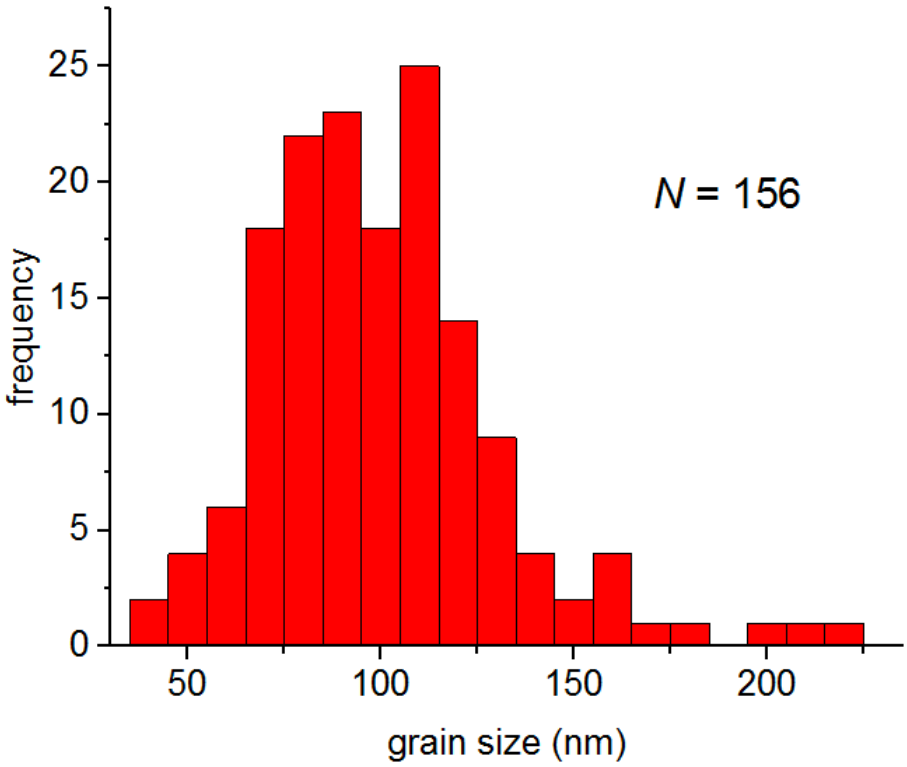

Figure S3. Histogram of the grain sizes for the as-deposited gold thin films.

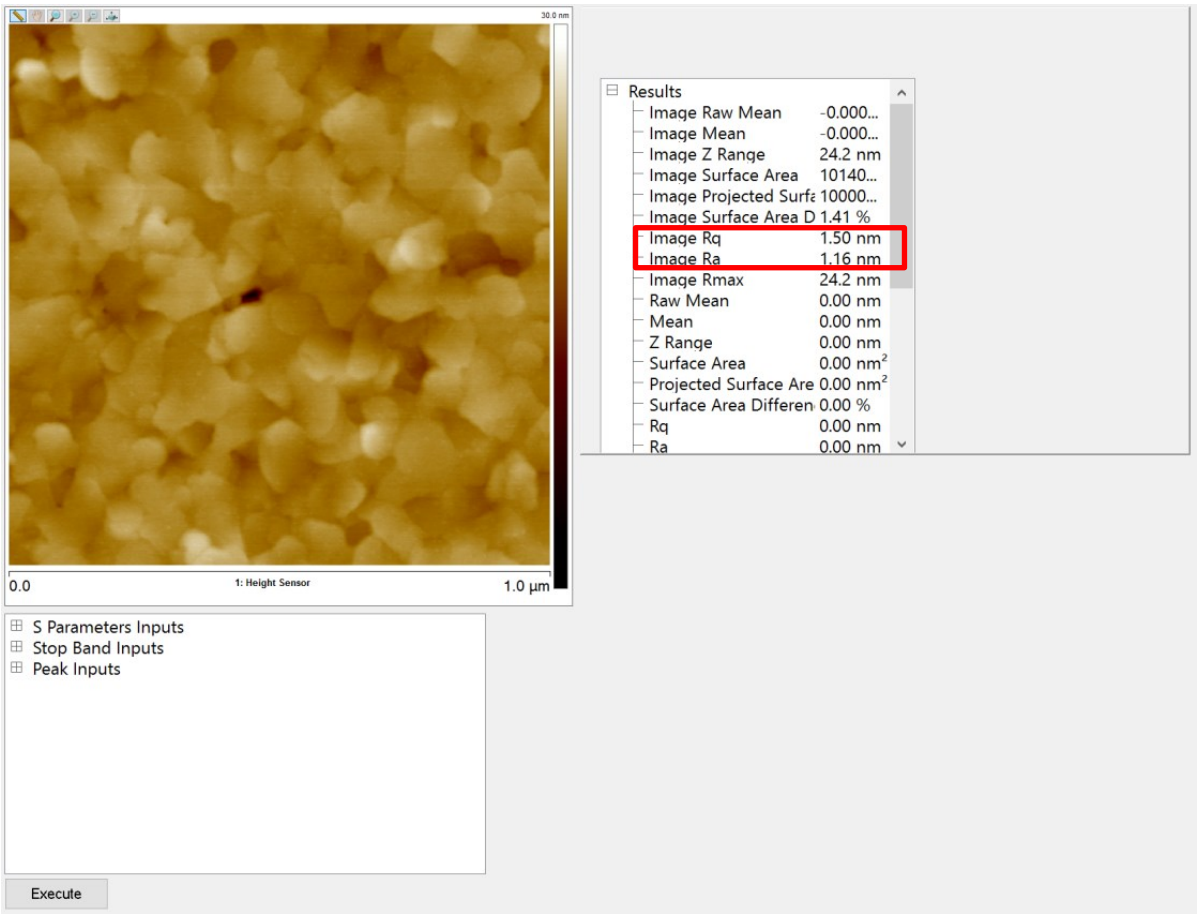
30.0 nm
0.0
1: Height Sensor
1.0 µm
Results
Image Raw Mean -0.000...
Image Mean -0.000...
Image Z Range 24.2 nm
Image Surface Area 10140...
Image Projected Surfa 10000...
Image Surface Area D 1.41 %
Image Rq 1.50 nm
Image Ra 1.16 nm
Image Rmax 24.2 nm
Raw Mean 0.00 nm
Mean 0.00 nm
Z Range 0.00 nm
Surface Area 0.00 nm²
Projected Surface Are 0.00 nm²
Surface Area Differen 0.00 %
Rq 0.00 nm
Ra 0.00 nm
S Parameters Inputs
Stop Band Inputs
Peak Inputs
Execute

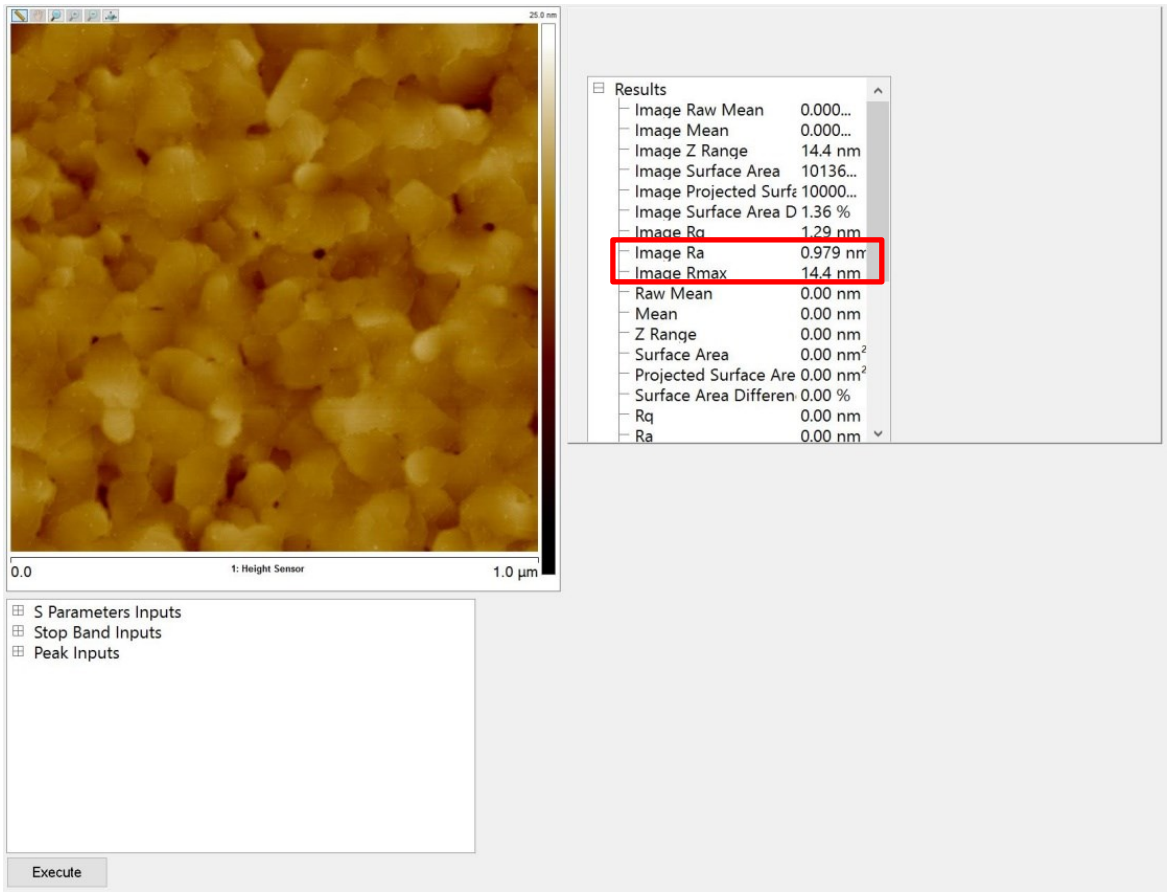

Figure S4. Examples of roughness analyses on films taken from two different evaporation lots. Values are indicated in red. Rq is the rms roughness and Ra is the average roughness.

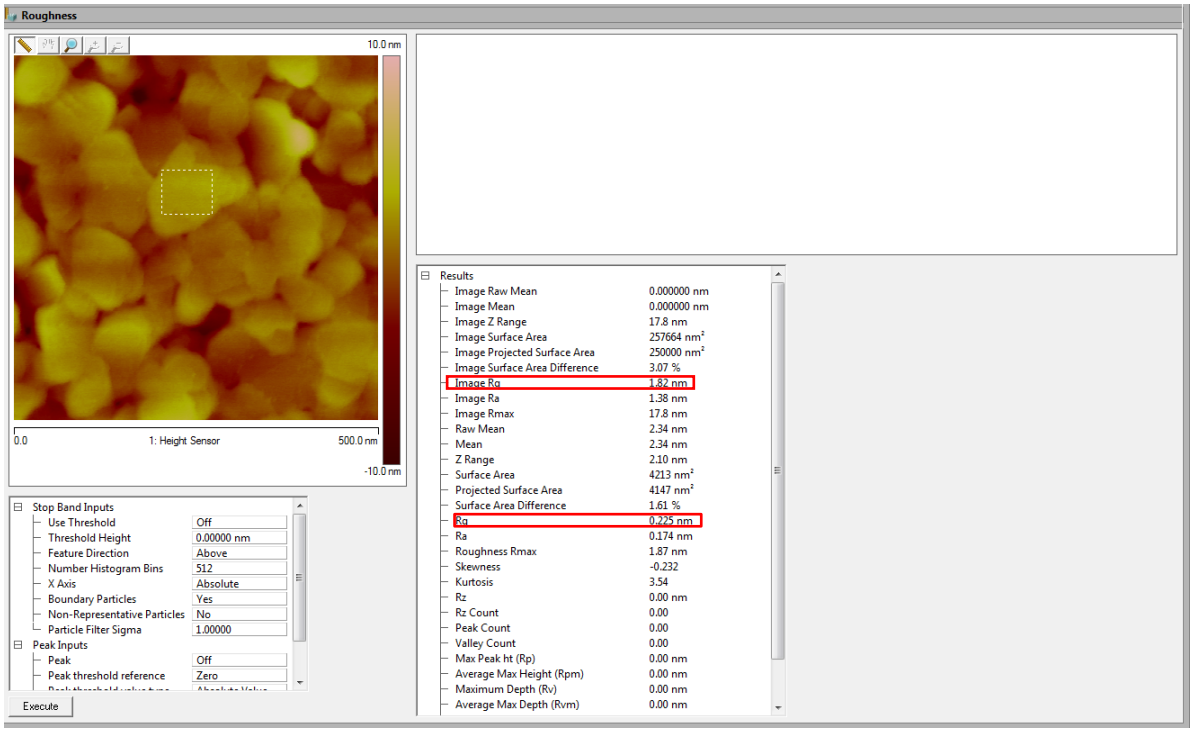

Figure S5. Example of roughness analysis results. The rms roughness of the 0.5 μm × 0.5 μm area is 1.82 nm. The rms roughness within the grain indicated by the white box is 0.225 nm.

(A)

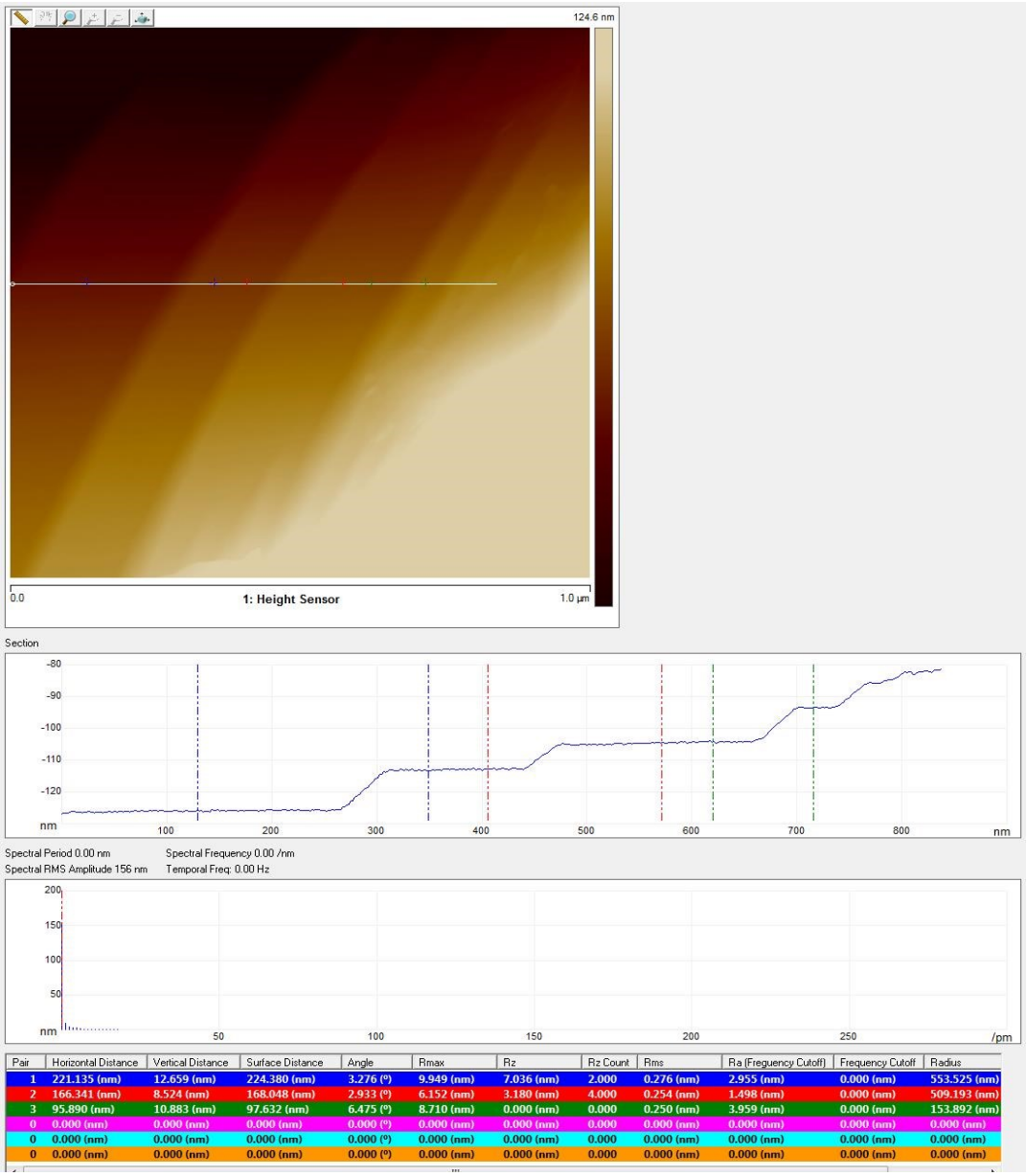

Pair	Horizontal Distance	Vertical Distance	Surface Distance	Angle	Rmax	Rz	Rz Count	Rms	Ra (Frequency Cutoff)	Frequency Cutoff	Radius
1	221.135 (nm)	12.659 (nm)	224.380 (nm)	3.276 (º)	9.949 (nm)	7.036 (nm)	2.000	0.276 (nm)	2.955 (nm)	0.000 (nm)	553.525 (nm)
2	166.341 (nm)	8.524 (nm)	168.048 (nm)	2.933 (º)	6.152 (nm)	3.180 (nm)	4.000	0.254 (nm)	1.498 (nm)	0.000 (nm)	509.193 (nm)
3	95.890 (nm)	10.883 (nm)	97.632 (nm)	6.475 (º)	8.710 (nm)	0.000 (nm)	0.000	0.250 (nm)	3.959 (nm)	0.000 (nm)	153.892 (nm)
0	0.000 (nm)	0.000 (nm)	0.000 (nm)	0.000 (º)	0.000 (nm)	0.000 (nm)	0.000	0.000 (nm)	0.000 (nm)	0.000 (nm)	0.000 (nm)
0	0.000 (nm)	0.000 (nm)	0.000 (nm)	0.000 (º)	0.000 (nm)	0.000 (nm)	0.000	0.000 (nm)	0.000 (nm)	0.000 (nm)	0.000 (nm)
0	0.000 (nm)	0.000 (nm)	0.000 (nm)	0.000 (º)	0.000 (nm)	0.000 (nm)	0.000	0.000 (nm)	0.000 (nm)	0.000 (nm)	0.000 (nm)

(B)

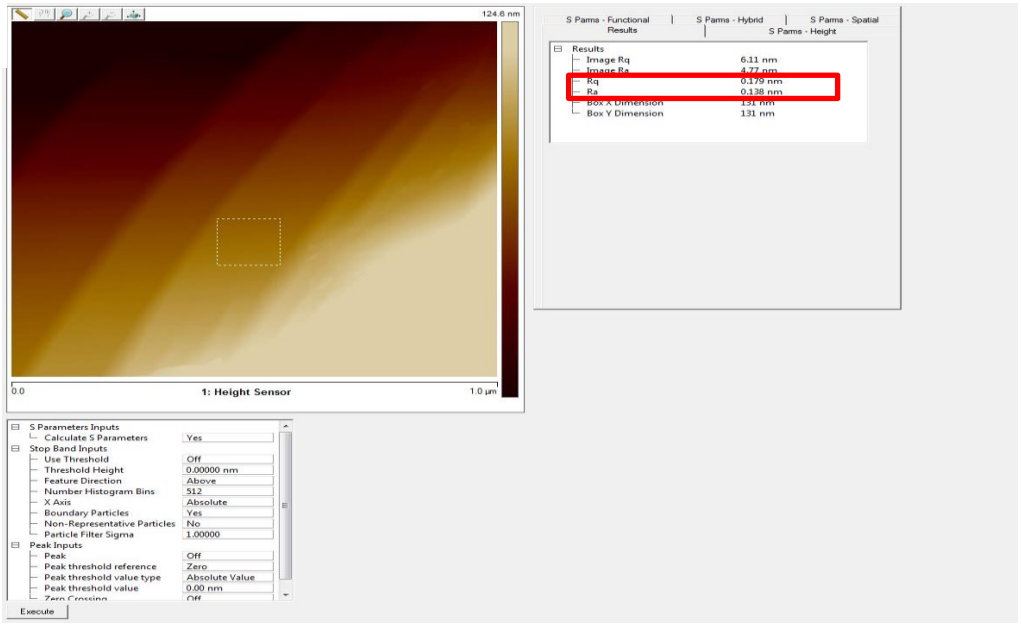

Figure S6. (A) Section analysis of an AFM image acquired on the surface of an annealed gold bead. (B) Roughness analysis on the surface of a flat terrace.

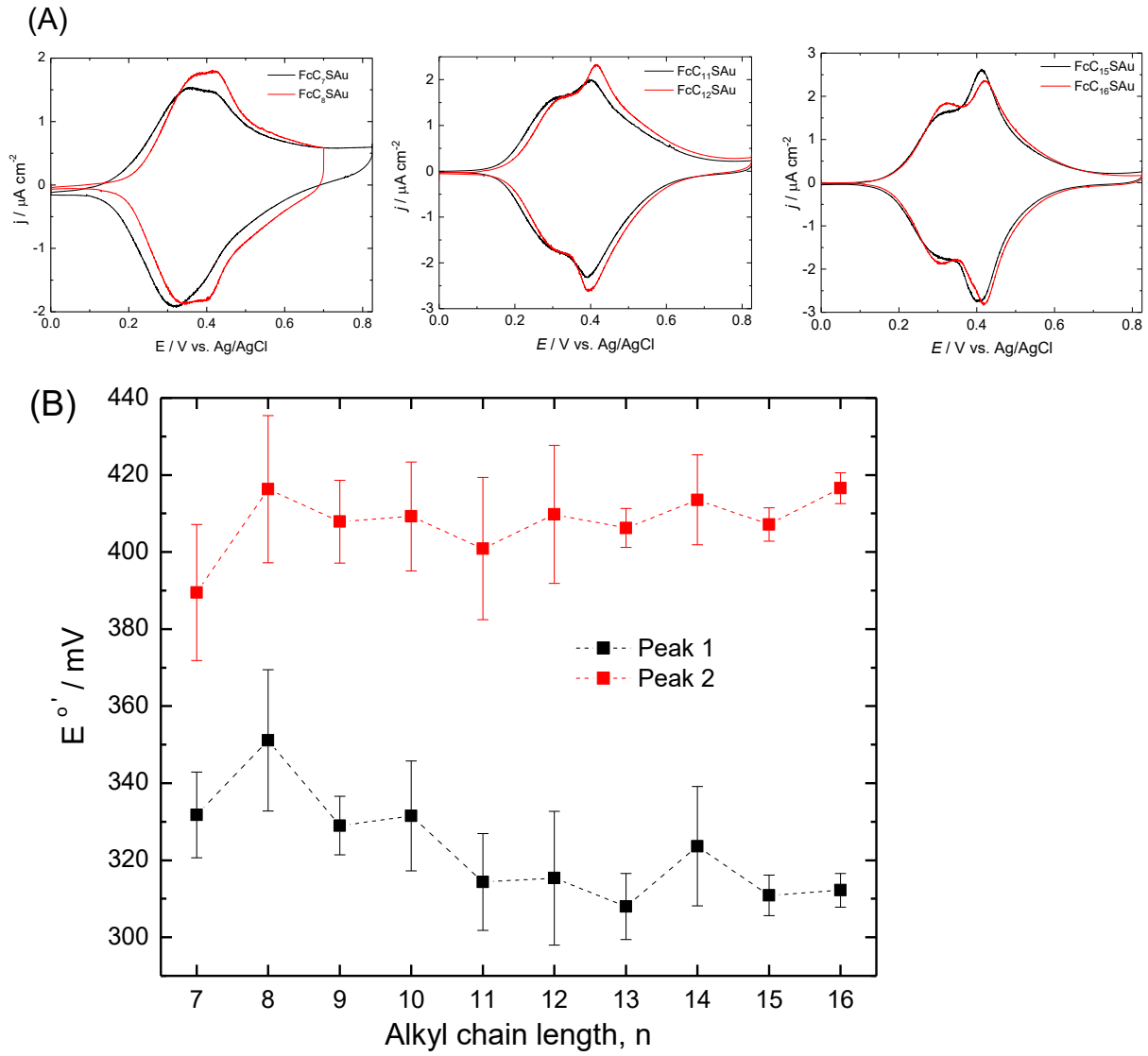

Figure S7. Cyclic voltammetry of FcC_nSAu SAMs formed on annealed gold beads. (A) Voltammograms for selected odd-even pairs. Electrolyte is 0.1 M $NaClO_{4(aq)}$. Scan rate is 10 mV s^{-1}. (B) Apparent redox potential $E^{o'}$ as a function of the number of methylenes n.

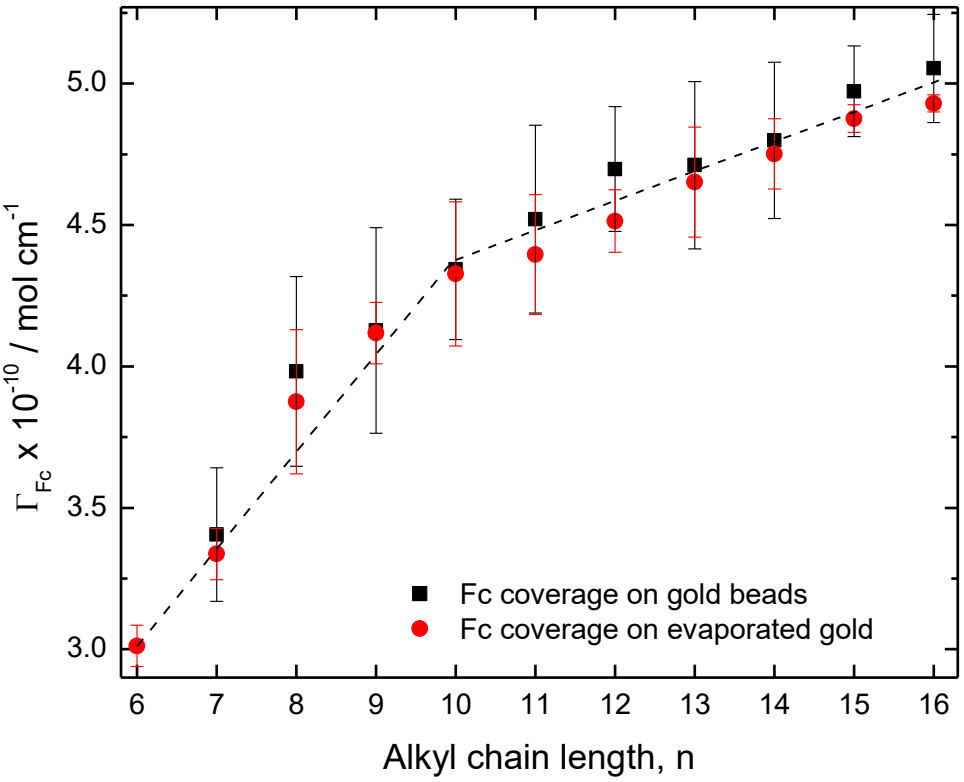

Figure S8. Comparison of the ferrocene surface coverages Γ_{Fc} of FcC_nSAu SAMs formed on thermally-evaporated gold thin films and annealed gold bead electrodes. The dashed line is a guide for the eye.

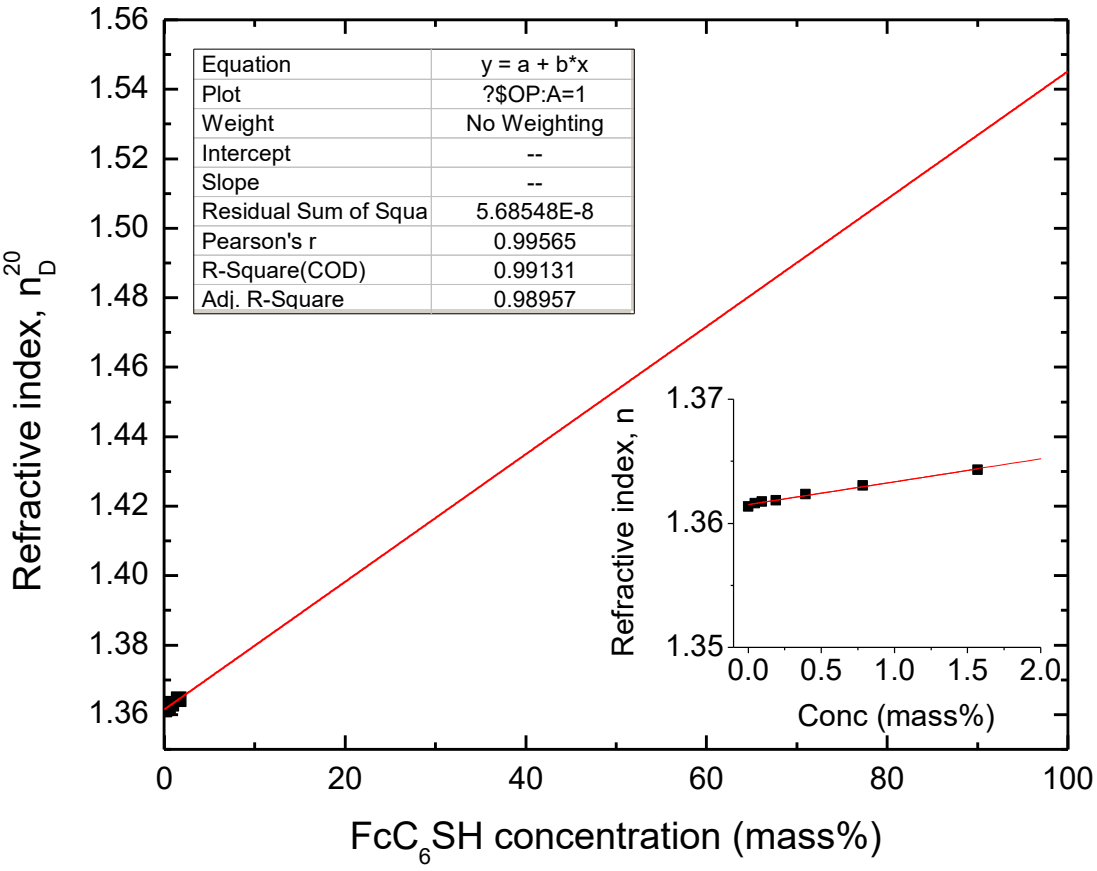

Figure S9. Refractive index values n_D^{20} measured for different mass percentages of FcC_6SH in anhydrous absolute ethanol. Limited solubility of FcC_6SH in ethanol. Linear regression gives: n = 0.00184*Conc% + 1.36152; r = 0.99565. Extrapolation of the data to 100% gives a bulk refractive index of 1.546 for the FcC_6SH, corresponding to a dielectric constant of 2.389.

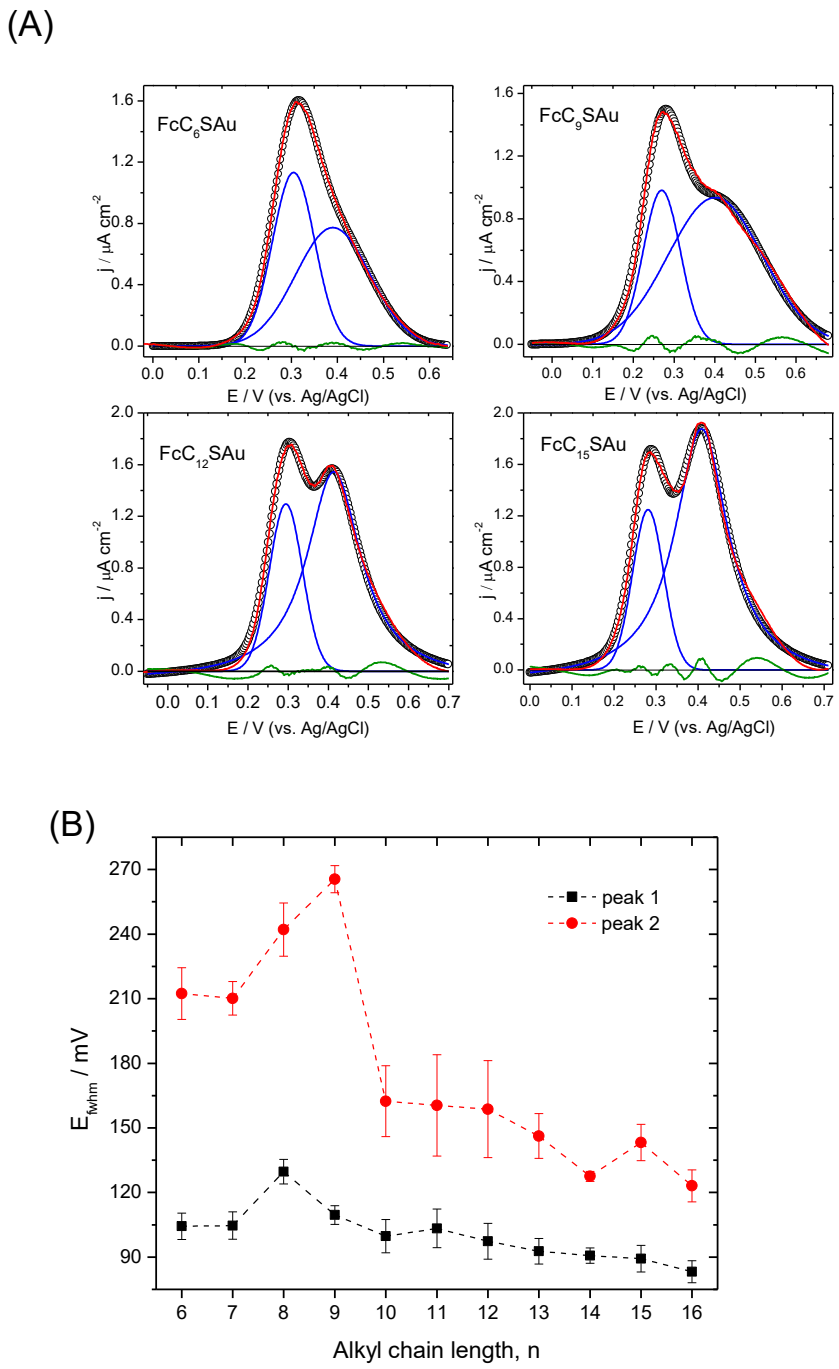

Figure S10. (A) Examples of the anodic peak deconvolutions.[9] Blue curves are the individual Gaussian and Lorentzian peaks and red curves are the cumulative fits. The green curves are the fitting residuals. The anodic peaks were baseline corrected before mathematical deconvolution. Functions used for the peak deconvolutions: FcC_6SAu Gaussian-Gaussian, FcC_9SAu Gaussian-Gaussian, $FcC_{12}SAu$ Gaussian-Lorentzian, and $FcC_{15}SAu$ Gaussian-

Lorentzian. (B) Full width at half maximum E_{fwhm} values obtained from the peak deconvolution.

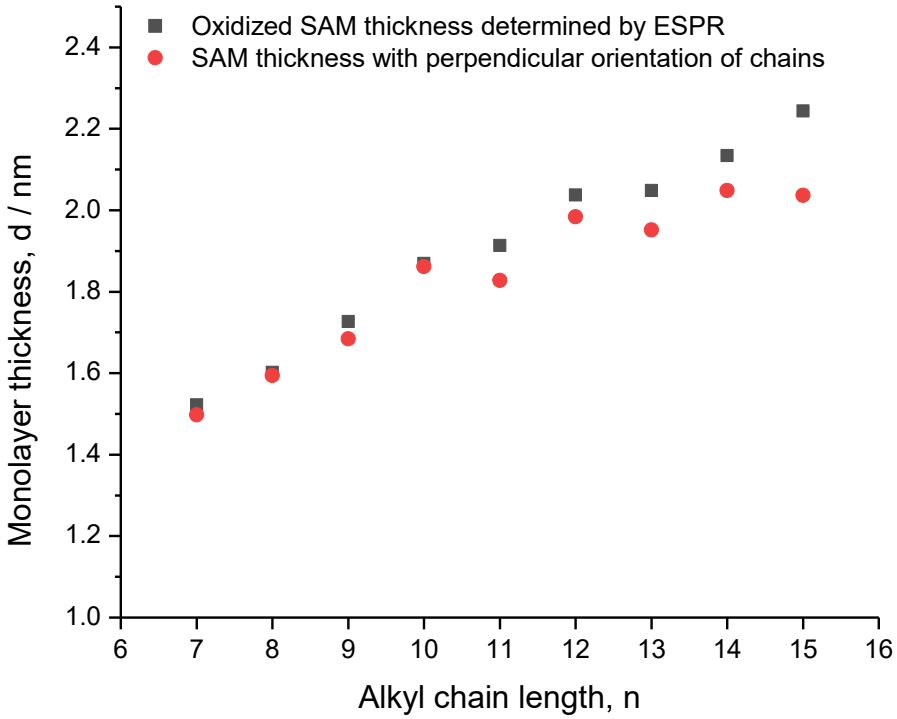

Figure S11. Comparison of FcC_nSAu SAM thicknesses obtained by ESPR and by assuming a perpendicular orientation of the alkyl chains in the oxidized state. The thicknesses of the SAMs with alkyl chains in the perpendicular orientation were calculated using trigonometry from the computed thicknesses of the reduced SAM[10] and computed alkyl chain tilt angles[11].

Statistical Analysis Results

1. Resonance angle change values, $\Delta\Theta_{\min}^{ox}$. The bold value at the bottom of each column represents the mean.

FcC$_n$SAu										
n = 6	n =7	n = 8	n = 9	n =10	n = 11	n = 12	n = 13	n = 14	n = 15	n = 16
0.01863	0.021063	0.021762	0.021876	0.020643	0.020611	0.019864	0.020936	0.02081	0.021177	0.020023
0.018206	0.021024	0.021458	0.02167	0.020468	0.02073	0.020112	0.020768	0.020693	0.021156	0.020137
0.018431	0.021297	0.02141	0.022096	0.020571	0.020644	0.020067	0.021854	0.020905	0.021281	0.019896
0.019378	0.021499	0.02161	0.022398	0.020471	0.020544	0.020196	0.020976	0.020475	0.021307	0.019949
0.018433	0.021158	0.021589	0.021987	0.02063	0.02141	0.019995	0.021803	0.020775	0.021222	0.019935
0.018487	0.021251	0.02174	0.022395	0.02072	0.021677	0.01981	0.022164	0.020732	0.021205	0.019862
0.018379	0.021135	0.021743	0.022048	0.02057	0.021437	0.019726	0.021733	0.020916	0.021248	0.020073
0.018482	0.02089	0.021696	0.021359	0.02072	0.021498	0.020167	0.021963	0.020904	0.021263	0.019951
0.018314	0.021507	0.02174	0.021489	0.02023	0.02159	0.020585	0.021162	0.020867	0.021199	0.019885
0.018291	0.021369	0.021264	0.022044	0.020242	0.020858	0.020345	0.021136	0.020694	0.021302	0.020122
0.019705	0.021487	0.02109	0.021483	0.020714	0.021134	0.020777		0.020671		0.020171
0.019645	0.021484	0.021911		0.020949	0.021265	0.019698				
0.01983	0.021479	0.021701			0.020855					
		0.021954			0.021479					
		0.021442								
		0.021649								
		0.021346								
		0.021568								
		0.021911								
0.018785	**0.021280**	**0.021610**	**0.021895**	**0.020577**	**0.021124**	**0.020112**	**0.021450**	**0.020767**	**0.021236**	**0.020000**

Two-sample *t*-test results on the above data, assuming unequal variance at 95% confidence level.[12]

i. If t Stat > t Critical, we conclude that the two means are not the same. The difference is significant.
ii. For any value of P ≤ 0.05, we would reject the null hypothesis and conclude that the means are not the same.[12]

FcC $_8$ SAu-FcC $_9$ SAu	Variable 1	Variable 2
Mean	0.021895039	0.02160959
Variance	1.27057E-07	5.2499E-08
Observations	11	19
Hypothesized Mean Difference	0	
df	15	
t Stat	2.385890136	
P(T<=t) one-tail	0.015329129	
t Critical one-tail	1.753050356	
P(T<=t) two-tail	0.030658257	
t Critical two-tail	2.131449546	

FcC $_9$ SAu-FcC $_{10}$ SAu	Variable 1	Variable 2
Mean	0.021895039	0.020577354
Variance	1.27057E-07	4.19659E-08
Observations	11	12
Hypothesized Mean Difference	0	
df	16	
t Stat	10.74173148	
P(T<=t) one-tail	5.03008E-09	
t Critical one-tail	1.745883676	
P(T<=t) two-tail	1.00602E-08	
t Critical two-tail	2.119905299	

FcC $_{10}$ SAu-FcC $_{11}$ SAu	Variable 1	Variable 2
Mean	0.021123776	0.02057735
Variance	1.62781E-07	4.1966E-08
Observations	14	12
Hypothesized Mean Difference	0	
df	20	
t Stat	4.443133806	
P(T<=t) one-tail	0.000124889	
t Critical one-tail	1.724718243	
P(T<=t) two-tail	0.000249778	
t Critical two-tail	2.085963447	

FcC $_{11}$ SAu-FcC $_{12}$ SAu	Variable 1	Variable 2
Mean	0.021123776	0.020111877
Variance	1.62781E-07	1.10736E-07
Observations	14	12
Hypothesized Mean Difference	0	
df	24	
t Stat	7.006971972	
P(T<=t) one-tail	1.5155E-07	
t Critical one-tail	1.71088208	
P(T<=t) two-tail	3.03101E-07	
t Critical two-tail	2.063898562	

FcC $_{12}$ SAu-FcC $_{13}$ SAu	Variable 1	Variable 2
Mean	0.021449547	0.02011188
Variance	2.53002E-07	1.1074E-07
Observations	10	12
Hypothesized Mean Difference	0	
df	15	
t Stat	7.198840597	
P(T<=t) one-tail	1.53965E-06	
t Critical one-tail	1.753050356	
P(T<=t) two-tail	3.0793E-06	
t Critical two-tail	2.131449546	

FcC $_{13}$ SAu-FcC $_{14}$ SAu	Variable 1	Variable 2
Mean	0.021449547	0.020767427
Variance	2.53002E-07	1.78563E-08
Observations	10	11
Hypothesized Mean Difference	0	
df	10	
t Stat	4.157148957	
P(T<=t) one-tail	0.0009788	
t Critical one-tail	1.812461123	
P(T<=t) two-tail	0.0019576	
t Critical two-tail	2.228138852	

FcC $_{14}$ SAu-FcC $_{15}$ SAu	Variable 1	Variable 2
Mean	0.021236091	0.02076743
Variance	2.75808E-09	1.7856E-08
Observations	10	11
Hypothesized Mean Difference	0	
df	13	
t Stat	10.7544153	
P(T<=t) one-tail	3.84438E-08	
t Critical one-tail	1.770933396	
P(T<=t) two-tail	7.68877E-08	
t Critical two-tail	2.160368656	

FcC $_{15}$ SAu-FcC $_{16}$ SAu	Variable 1	Variable 2
Mean	0.021236091	0.020000354
Variance	2.75808E-09	1.2118E-08
Observations	10	11
Hypothesized Mean Difference	0	
df	15	
t Stat	33.29582528	
P(T<=t) one-tail	8.89747E-16	
t Critical one-tail	1.753050356	
P(T<=t) two-tail	1.77949E-15	
t Critical two-tail	2.131449546	

2. Dielectric constants of FcC_nSAu SAMs on gold beads determined by EIS. The bold value at the bottom of each column represents the mean.

	FcC_nSAu									
	n =7	*n* =8	*n* =9	*n* =10	*n* =11	*n* =12	*n* = 13	*n* =14	*n* =15	*n* =16
	3.08	3.13	2.95	3.15	3.00	3.28	2.79	3.08	2.79	3.04
	3.20	3.05	2.90	2.89	2.78	3.10	2.83	2.96	2.83	3.26
	3.12	2.99	3.01	3.18	2.79	3.28	2.84	2.99	2.95	3.01
	3.34	2.83	3.05	3.19	2.84	3.10	2.99	2.96	2.67	3.24
	3.20	3.07	2.80	3.33	3.09	2.91	2.76	2.99	2.87	2.89
	3.23	3.00	3.01	3.23	3.08	3.10	2.88	3.28	2.84	3.02
	3.21	3.20	3.01	3.13	2.81	2.95	2.94	3.18	2.77	3.20
	3.18	3.13	2.97	2.96	2.76	3.07	2.96	3.10	2.72	3.22
	3.16	3.34	3.01	2.99	2.71	2.94	2.91	3.03	2.89	3.15
	3.17	3.24	2.96	3.06	2.90	2.94	2.89	3.06	2.85	2.80
	3.11	3.27	3.11	3.01	2.80	3.28	2.88		3.02	3.05
	3.08	3.26		2.98	2.72	3.29	2.82		2.99	3.01
	3.05	3.10				3.20	2.78		2.95	2.97
		3.03							2.92	
		3.07								
		2.87								
Mean	**3.16**	**3.10**	**2.98**	**3.09**	**2.86**	**3.12**	**2.87**	**3.06**	**2.86**	**3.05**

Two-sample *t*-test results on the above data, assuming unequal variance at 95% confidence level.[12]

i. If t Stat > t Critical, we can conclude that the two means are not the same. The difference is significant.
ii. For any value of P ≤ 0.05, we would reject the null hypothesis and conclude that the means are not the same.[12]

FcC $_7$ SAu-FcC $_8$ SAu	*Variable 1*	*Variable 2*
Mean	3.1633183	3.0990305
Variance	0.0060719	0.0199452
Observations	13	16
Hypothesized Mean Difference	0	
df	24	
t Stat	1.5529878	
P(T<=t) one-tail	0.0667573	
t Critical one-tail	1.7108821	
P(T<=t) two-tail	0.1335147	
t Critical two-tail	2.0638985	

FcC $_8$ SAu-FcC $_9$ SAu	*Variable 1*	*Variable 2*
Mean	3.0990305	2.9811815
Variance	0.0199452	0.0063901
Observations	16	11
Hypothesized Mean Difference	0	
df	24	
t Stat	2.7567531	
P(T<=t) one-tail	0.0054877	
t Critical one-tail	1.7108821	
P(T<=t) two-tail	0.0109754	
t Critical two-tail	2.0638985	

FcC $_9$ SAu-FcC $_{10}$ SAu	*Variable 1*	*Variable 2*
Mean	2.9811815	3.0935463
Variance	0.0063901	0.0168446
Observations	11	12
Hypothesized Mean Difference	0	
df	19	
t Stat	2.5222597	
P(T<=t) one-tail	0.0103712	
t Critical one-tail	1.7291328	
P(T<=t) two-tail	0.0207424	
t Critical two-tail	2.093024	

FcC $_{10}$ SAu-FcC $_{11}$ SAu	*Variable 1*	*Variable 2*
Mean	3.0935463	2.8564244
Variance	0.0168446	0.0174869
Observations	12	12
Hypothesized Mean Difference	0	
df	22	
t Stat	4.4331849	
P(T<=t) one-tail	0.0001047	
t Critical one-tail	1.7171443	
P(T<=t) two-tail	0.0002094	
t Critical two-tail	2.0738731	

$FcC_{11}SAu$-$FcC_{12}SAu$	*Variable 1*	*Variable 2*
Mean	2.8564244	3.1178369
Variance	0.0174869	0.02471
Observations	12	13
Hypothesized Mean Difference	0	
df	23	
t Stat	4.511131	
P(T<=t) one-tail	7.872E-05	
t Critical one-tail	1.7138715	
P(T<=t) two-tail	0.0001574	
t Critical two-tail	2.0686576	

$FcC_{12}SAu$-$FcC_{13}SAu$	*Variable 1*	*Variable 2*
Mean	3.1178369	2.8683351
Variance	0.02471	0.0050268
Observations	13	13
Hypothesized Mean Difference	0	
df	17	
t Stat	5.2167288	
P(T<=t) one-tail	3.49E-05	
t Critical one-tail	1.7396067	
P(T<=t) two-tail	6.981E-05	
t Critical two-tail	2.1098156	

$FcC_{13}SAu$-$FcC_{14}SAu$	*Variable 1*	*Variable 2*
Mean	2.8683351	3.0638621
Variance	0.0050268	0.0105288
Observations	13	10
Hypothesized Mean Difference	0	
df	15	
t Stat	5.1533738	
P(T<=t) one-tail	5.891E-05	
t Critical one-tail	1.7530503	
P(T<=t) two-tail	0.0001178	
t Critical two-tail	2.1314495	

$FcC_{14}SAu$-$FcC_{15}SAu$	*Variable 1*	*Variable 2*
Mean	3.0638621	2.8616724
Variance	0.0105288	0.0103756
Observations	10	14
Hypothesized Mean Difference	0	
df	19	
t Stat	4.7736283	
P(T<=t) one-tail	6.604E-05	
t Critical one-tail	1.7291328	
P(T<=t) two-tail	0.0001321	
t Critical two-tail	2.093024	

$FcC_{15}SAu$-$FcC_{16}SAu$	*Variable 1*	*Variable 2*
Mean	2.8616724	3.0514286
Variance	0.0103756	0.0212593
Observations	14	14
Hypothesized Mean Difference	0	
df	23	
t Stat	3.9918724	
P(T<=t) one-tail	0.000287	
t Critical one-tail	1.7138715	
P(T<=t) two-tail	0.000574	
t Critical two-tail	2.0686576	

References

(1) Amara, N.; Mashiach, R.; Amar, D.; Krief, P.; Spieser, S. A. H.; Bottomley, M. J.; Aharoni, A.; Meijler, M. M., Covalent Inhibition of Bacterial Quorum Sensing. *J. Am. Chem. Soc.* **2009,** *131* (30), 10610-10619.

(2) Bartra, M.; Vilarrasa, J., Cyclization of 9-substituted decanoic acid derivatives to 9-decanolide and 9-decanolactam. *J. Org. Chem.* **1991,** *56* (17), 5132-5138.

(3) Adejare, A.; Shen, J.; Ogunbadeniyi, A. M., Halogens halt aromatic group migration in Baeyer–Villiger oxidation. *J. Fluorine Chem.* **2000,** *105* (1), 107-109.

(4) Huisgen, R.; Ott, H., Die konfiguration der carbonestergruppe und die sondereigenschaften der lactone. *Tetrahedron* **1959,** *6* (3), 253-267.

(5) Bidd, I.; Kelly, D. J.; Ottley, P. M.; Paynter, O. I.; Simmonds, D. J.; Whiting, M. C., Convenient syntheses of bifunctional C12-acyclic compounds from cyclododecanone. *J. Chem. Soc., Perkin Trans. 1* **1983**, 1369-1372.

(6) Fujisawa, T.; Mori, T.; Kawara, T.; Sato, T., One-Step Synthesis of ω-Hydroxycarboxylic Acids by the Reaction of ω-Metaloxylated Grignard Reagents with β-Propiolactones. *Chem. Lett.* **1984,** *11*, 569-570.

(7) Creager, S. E.; Rowe, G. K., Competitive self-assembly and electrochemistry of some ferrocenyl-n-alkanethiol derivatives on gold. *J. Electroanal. Chem.* **1994,** *370* (1), 203-211.

(8) Tazaki, M.; Okada, K.; Yakata, K.; Nakano, K.; Sakai, M.; Yonemitsu, T., Facile, Convenient Synthesis of Highly Pure ω-Ferrocenylalkanethiols as Probes for Self-Assembled Monolayer (SAM) on Gold Surface. *Phosphorus, Sulfur Silicon Relat. Elem.* **2000,** *167* (1), 239-249.

(9) Lee, L. Y. S.; Sutherland, T. C.; Rucareanu, S.; Lennox, R. B., Ferrocenylalkylthiolates as a Probe of Heterogeneity in Binary Self-Assembled Monolayers on Gold. *Langmuir* **2006,** *22* (9), 4438-4444.

(10) Nerngchamnong, N.; Yuan, L.; Qi, D.-C.; Li, J.; Thompson, D.; Nijhuis, C. A., The Role of van der Waals Forces in the Performance of Molecular Diodes. *Nat. Nanotechnol.* **2013,** *8* (2), 113-118.

(11) Yuan, L.; Thompson, D.; Cao, L.; Nerngchangnong, N.; Nijhuis, C. A., One Carbon Matters: The Origin and Reversal of Odd–Even Effects in Molecular Diodes with Self-Assembled Monolayers of Ferrocenyl-Alkanethiolates. *J. Phys. Chem. C* **2015,** *119* (31), 17910-17919.

(12) Harris, D. C., *Quantitative Chemical Analysis*. 6th ed.; W. H. Freeman and Co: 2003.